

# **LIQUID METAL PUMPS FOR ENABLING HEAT TRANSFER AT EXTREME TEMPERATURES**

A Thesis  
Presented to  
The Academic Faculty

by

Caleb Amos Amy

In Partial Fulfillment  
of the Requirements for the Degree  
Master of Science Mechanical Engineering from the  
George W. Woodruff School of Mechanical Engineering

Georgia Institute of Technology  
December 2017

**© CALEB AMY 2017**

**LIQUID METAL PUMPS FOR ENABLING HEAT TRANSFER AT  
EXTREME TEMPERATURES**

Approved by:

Dr. Asegun Henry, Advisor  
School of Mechanical Engineering  
Georgia Institute of Technology

Dr. Shannon Yee  
School of Mechanical Engineering  
*Georgia Institute of Technology*

Dr. Samuel Graham  
School of Mechanical Engineering  
*Georgia Institute of Technology*

Dr. Devesh Ranjan  
School of Mechanical Engineering  
*Georgia Institute of Technology*

Date Approved: July 24<sup>th</sup>, 2017

## ACKNOWLEDGEMENTS

I thank my parents for their encouragement and teachings throughout my life, in addition to their support. I also want to thank my fiancé, Taylor Dudley, for her support, encouragement, and flexibility over the last decade.

I thank my advisor, Dr. Asegun Henry, for his mentorship, teaching, feedback, and editing. Dr. Diane England shared expertise on material compatibility, bonding, and sealing, in addition to advice from Dr. Ken Sandhage. Also, Dr. Shannon Yee provided helpful feedback throughout the process, which helped me focus on important issues upfront.

I also want to thank my fellow graduate students—Malavika Bagepalli, Daniel Budenstein, Freddy DeAngelis, and Greg Wilk—for their advice and time. Colin Kelsall, Akhil Chavan, and Haiqi Wen also contributed significantly as undergraduates.

Finally, I would like to thank the ARPA-E agency for the financial support of project DE-AR0000339, through which this work was made possible.

# TABLE OF CONTENTS

<b>ACKNOWLEDGEMENTS</b>	<b>iii</b>
<b>LIST OF TABLES</b>	<b>vi</b>
<b>LIST OF FIGURES</b>	<b>vii</b>
<b>LIST OF SYMBOLS AND ABBREVIATIONS</b>	<b>xii</b>
<b>SUMMARY</b>	<b>xv</b>
<b>Chapter 1. Introduction</b>	<b>1</b>
1.1 Challenges and State-of-the-Art	2
1.2 Solution Approach	4
1.3 Applications	6
<b>Chapter 2. Material Selection</b>	<b>10</b>
2.1 Temperature	11
2.2 Gas Environment	11
2.3 Heat Transfer Fluid	12
2.4 Potential Containment Materials	18
<b>Chapter 3. Design and Modeling of The Pump System</b>	<b>23</b>
3.1 Pump Type	23
3.2 Primary Pump Material	27
3.2.1 Medium Temperature Pumps	28
3.2.2 Shapal Hi-M Soft™	32
3.2.3 Tungsten	34
3.3 Pump Sealing	36
3.4 Pump Mounting	38
3.4.1 Thermal modelling using COMSOL Multiphysics	41
3.5 Pump Actuation	43
3.5.1 Potential Alignment Solutions	48
<b>Chapter 4. Experimental Setup</b>	<b>54</b>
4.1 Circulation Loop	55
4.2 Static Seals	59
4.3 Flow Meter	64
4.4 Thermal Management Equipment	80
4.4.1 Heating Equipment	80
4.4.2 Cooling Equipment	87
4.4.3 Insulation	89
4.4.4 Temperature Measurement and Control	91
4.5 Nitrogen Chamber	93
<b>Chapter 5. Experimental Results and Discussion</b>	<b>99</b>

<b>5.1</b>	<b>Medium Temperature Pumps</b>	<b>99</b>
<b>5.2</b>	<b>Shapal Hi-M Soft™</b>	<b>103</b>
5.2.1	Initial Unsuccessful Tests	103
5.2.2	Primary Successful Tests	117
<b>5.3</b>	<b>Tungsten</b>	<b>125</b>
<b>5.4</b>	<b>Discussion and Future Work</b>	<b>126</b>
5.4.1	Wear Resistance	126
5.4.2	Shaft Actuation	135
5.4.3	Compatible fluids	138
<b>Chapter 6. Conclusion</b>		<b>141</b>
<b>Appendix A: Commerical Thermal Energy Grid Storage (TEGS) Attempts</b>		<b>143</b>
<b>Appendix B: Properties and Mesh Convergence of Thermal Models</b>		<b>153</b>
<b>Appendix C: Pump Speed and Perfomance Recommendations</b>		<b>155</b>
<b>Appendix D: SiC formation on C: Thickness limitations</b>		<b>157</b>
<b>REFERENCES</b>		<b>158</b>

## LIST OF TABLES

Table 1: Compatibility of representative candidate fluids and some unprotected containment materials up to 1350°C. Adapted from [10, 50] and various sources in the open literature, including recent results for Sn at 1350°C from [44]. ✓ indicates good compatibility (corrosion rate below 1 mil/year (25.4 μm/year)); — limited (between 1 and 10 mils/year); × poor (larger than 10 mils/year). *SiC can have good stability with Sn if ~0.5% Si is added. ....	15
Table 2: Properties and cost of selected liquid metals at 600°C.....	16
Table 3: Theoretical performance of visual flow meter.....	75
Table 4: Wear amount and rates for gears after 72 hours (~1,000,000 rev.). While most wear occurred at the gear teeth, the wear most detrimental to performance occurred at the radial gear tips—because this allowed fluid to leak around the teeth. This surface only contacts the pump body as the shaft wears; thus, minimizing the shaft/bearing wear rate is key.....	125

## LIST OF FIGURES

Figure 1A: Mapping of involute profile to create gear tooth profile. The black point moves in the direction of the blue arrows, while the gears rotate, to form the tooth shape. Here, the gear tooth shape is determined by the path the point on a string would follow as the string is unwound from one gear base circle onto the other. B: The pressure angle of an external gear pump is the angle between a line connecting the center of the two gears and a line tangent to the tangent plane of contact between the gear teeth. A larger angle puts less stress on the teeth, but more force on the gear shafts, which causes increased friction, wear, and power consumption..... 25

Figure 2: The model of the pump gears on the bottom illustrates the direction of gear rotation with a plot showing how the volume near the outlet (in blue) changes with rotation. Gear pumps use the meshing of gears to pump fluid trapped in the cavity between the teeth around the outside of the gears. Because the gears remain in contact, fluid cannot return through the center, so it is forced out of the outlet. In this design, there are 7 teeth, so the rotation per period is  $\sim 52^\circ$ . The two discontinuities in the plot are associated with transition points where the volume in the outlet region is abruptly included (VG), and abruptly removed (VL), as shown in the bottom right and left, respectively, highlighted in orange. The slope of the volume vs. angle or time is the volumetric flow rate and is theoretically constant for a fixed rotational speed of the gears. .... 26

Figure 3: Relative corrosion of stainless-steel gears after less than 24 hours of contact with Sn at  $\sim 300^\circ\text{C}$ . the gear on the left was coated with CrN ..... 29

Figure 4: Inconel 625 external gear pump. Notably, the base of this pump differs from the high temperature pumps, because this pump was mounted directly to its baseplate..... 31

Figure 5: Shapal Hi-M Soft™ external gear pump..... 33

Figure 6: Tungsten external gear pump ..... 35

Figure 7: Model of graphite packing shaft seal. This seal expands radially (here, vertically) when compressed axially (here, horizontally) by the symmetric gland plate. Also shown is the graphite sheet based face seal..... 38

Figure 8: Model of the pump with mount, shafts, and motor ..... 39

Figure 9: Ceramic (Shapal) bolts which failed from brittle fracture during installation .. 40

Figure 10: Thermal model of the pump system ..... 43

Figure 11: Thermal expansion of pump system at  $1350^\circ\text{C}$  ..... 45

Figure 12: Schematic of stylus based, visual shaft alignment tool..... 46

Figure 13: Commercial and custom in-situ stylus indicator tools .....	47
Figure 14: Image showing the resolution limitations of custom styli gap measurement system .....	48
Figure 15: Typical single universal joint for nonparallel shafts .....	49
Figure 16: Zirconia (ZrO <sub>2</sub> ) ball bearing failure .....	50
Figure 17: Filleted tungsten sleeve bearing to support zirconia shaft extension .....	51
Figure 18: Image of pump system .....	53
Figure 19: Model of pump with circulation loop. Reservoir shown illuminated for comparison to images from experiments, like Figure 57.....	55
Figure 20: Graphite Sealer applied to a pipe and glue joint. Pipe is filled with 931S sealer. Top of pipe is connected to nitrogen reservoir at 1 atm gauge pressure and bottom of pipe is plugged.....	57
Figure 21: Splashed Sn around the reservoir from freefalling Sn inlet .....	58
Figure 22: Tungsten mesh cover for reservoir to reduce splashing .....	59
Figure 23: C union, W union, CrN coated steel union, and Shapal bolt for reference (from left to right). The C union is the largest because it has the lowest strength. Both the C and W unions are compatible with liquid Sn above 1350°C. The Shapal bolt, which failed, is shown as an example of the need to oversize brittle components. ....	61
Figure 24: Static seal of a molten Sn fluid connection .....	62
Figure 25: SEM images of unsealed (left) and sealed (right) reaction bonded joints. Note that the sealed image is 4X magnified, relative to the unsealed image. The images are of different joints, so it was necessary to include a magnified image to show the sealed joint. ....	64
Figure 26: Weight based flow meter system (insulated) supported by steel legs which rest on a scale (Scale not visible).....	67
Figure 27: Flow meter dynamic cover which functioned as a guard against insulation particulate.....	68
Figure 28A: Weight flow meter calibration showing mass flow rate as a function of the weight of Sn in the flowmeter, B: zoomed in on the low flow rate regime, where experimental results are inconsistent, and on average diverge from the prediction based on Bernoulli's equation. C: Fully displayed experimental data, showing divergence from the theoretical curve at mass measurements above ~750 g. This was a result of delayed stopping of inlet flow. Each plot is an average of 10 tests. ....	70

Figure 29: Visual flow meter design and calibration. A: Plot of the measured flow rate vs. mass in the flow meter (mass uncertainty $\pm 5$ g), with identification of the flow regimes. B/C/D: Illustrations of three possible flow regimes that can be detected by the visual flow meter. The flow diverter used to keep the inlet flow from bypassing the flow meter is highlighted in D. ....	74
Figure 30: Flow diverter for visual flow meter (shown inverted) .....	76
Figure 31: Visual flow meter with alignment pins and cover attached with W bolts.....	77
Figure 32: Calibration of the visual flow meter, experimental setup .....	78
Figure 33: Circulation loop with the visual flow meter installed above the reservoir, shown in two-outlet flow regime. ....	79
Figure 34: Comparison of the temperature profile of a reservoir filled with Sn under transient inductive heating. A single coil resulted in $\sim 20\%$ more power coupled than four coils, although only half of the rated power was coupled.....	82
Figure 35: Comparison of single-coil and four-coil induction loops.....	84
Figure 36: Model of induction heater with circulation loop.....	85
Figure 37A: Fiberglass insulated heat tape, B: Alumina insulated Kanthal heater .....	87
Figure 38: Cooling network showing oil cooled tubing and components .....	89
Figure 39: Alumina blanket (left) and rigid (right) insulation.....	90
Figure 40: Insulation process for experiments above $1000^{\circ}\text{C}$ .....	91
Figure 41: LabVIEW Front Panel, with a view of the block diagram used to compare thermocouple temperature to the set point temperature.....	92
Figure 42: Control System showing flow of information from LabVIEW to $\text{N}_2$ Chamber .....	93
Figure 43: Sn Getter for oxygen removal via the formation of tin oxide .....	95
Figure 44: Oxygen content over time during oxygen removal process in preparation for high temperature experiments.....	95
Figure 45: Chamber view including seals and visual flowmeter port .....	97
Figure 46: Nitrogen Chamber railings and 80/20 frame for installing experiment table..	98
Figure 47: Corrosion on Inconel 625 gear teeth after scratching.....	100
Figure 48: Excessive oxidation after test with Sn at $400^{\circ}\text{C}$ .....	101

Figure 49: Sn leak at removable joint caused by inadequate ferrule compression.....	102
Figure 50: Leak caused by loosening of pump face seal bolts from thermal expansion	106
Figure 51: Backup monitoring/control system to circumvent signal interference issues	108
Figure 52: relative pore size of a new extruded graphite reservoir compared to one that was heated to 1350°C for ~10 hours in N <sub>2</sub> chamber when significant oxidation was observed.....	109
Figure 53: Tungsten mesh un-bonded from graphite mount after the reaction bond suffered severe oxidation .....	111
Figure 54: Pump failure caused by phase transformation and misalignment induced stress in the ZrO <sub>2</sub> bearing. The Shapal pump shaft has visibly failed, but this was preceded by failure of the bearing.....	113
Figure 55A: Shapal pump internal geometry and B: Shapal wear surfaces .....	115
Figure 56: Sanding pump shafts to reduce wear rate by minimizing surface roughness	117
Figure 57: Image from pump test which reached 1490°C .....	118
Figure 58: Pump temperature and throttle, during test which reached 1415°C.....	119
Figure 59: Pump system in configuration used for 72 hour test.....	120
Figure 60: Pump temperature and throttle, during 72 hours of pumping near 1200°C ..	121
Figure 61: Image depicting flow decrease (dripping) out of second outlet after 55 hours .....	123
Figure 62: Wear on Shapal gear teeth after 72 hours of continuous pumping .....	124
Figure 63: Example of lightweighting of tungsten components to reduce cost and weight induced stress .....	126
Figure 64: Diagram of sleeve bearing lubrication .....	129
Figure 65: Actively self-lubricated sleeve bearing. Here, the concept is to connect the pressure side of the pump to the angular position on the bearing/shaft interface with the highest pressure. This pressure is caused by a reaction force from the gear meshing, as shown. The lubricant is routed to the back of the bearing to maximize the leak path back out of the bearing. Thus, the (top) drive gear is pushed to the left, so it needs lubricant (Sn) on this side. Because this is the pressure side of the pump, a straight path connects the pressure cavity to the bearing. On the other hand, the (bottom) idler gear is pushed to the right, so a helical path is required to lubricate it—this bearing is detailed on the far right of this figure. ....	132

Figure 66: Continuous meshing of two herringbone gears ..... 134

Figure 67: Alternate pump mount design where the pump is bolted at the same vertical height as the drive gear, so that it expands about this plane, and thus remains in perfect alignment with the external bearing—independent of temperature..... 136

Figure 68: Alternate shaft actuation system. Here, both the hot (left) and cold (right) sides of the system accommodate misalignment through the use of flexible helical couplers. In this case, the hot coupler would be W or Mo based. .... 137

Figure 69: Alternate shaft actuation and mounting system. Here, thermally independent alignment can be achieved by mounting the pump directly to the motor at the plane of the pump drive shaft. This configuration would ideally have a vertical shaft axis to keep the forces symmetric. .... 138

## LIST OF SYMBOLS AND ABBREVIATIONS

Symbol	Definition
Al	Aluminum
Al <sub>2</sub> O <sub>3</sub>	Aluminum Oxide (Alumina)
Al <sub>2</sub> TiO <sub>5</sub>	Aluminum Titanate
AlN	Aluminum Nitride
Bi	Bismuth
BN	Boron Nitride
C	Carbon
Ca	Calcium
CA	Controlled Atmosphere
CaO	Calcium Oxide
CO	Carbon Monoxide
CO <sub>2</sub>	Carbon Dioxide
Cr	Chromium
CrN	Chromium Nitride
CSP	Concentrated Solar Power
CTE	Coefficient of Thermal Expansion
DBTT	Ductile-Brittle Transition Temperature
DSLR	Digital Single-Lens Reflex
EDM	Electrical Discharge Machining
EHL	Elastohydrodynamic Lubrication

Fe	Iron
FKM	Fluoroelastomer
Ga	Gallium
H <sub>2</sub> O	Water
HTF	Heat Transfer Fluid
HV	Vickers Hardness (kg mm <sup>-2</sup> )
In	Indium
K	Potassium
$\dot{m}$	Mass flow rate (kg s <sup>-1</sup> )
Mg	Magnesium
N <sub>2</sub>	Diatomic Nitrogen
Ni	Nickel
NiCrAlY	Nickel Chromium Aluminum Yttrium (spray for coating adhesion)
P	Pressure (Pa)
Pb	Lead
ppm	Parts per million
PTFE	Polytetrafluoroethylene
PVD	Physical Vapor Deposition
Re	Rhenium
RMS	Root mean square (surface roughness, often in $\mu\text{m}$ )
rpm	Revolutions per minute
S	Sommerfeld number
SEM	Scanning Electron Microscope

Si	Silicon
Si <sub>3</sub> N <sub>4</sub>	Silicon Nitride
SiC	Silicon Carbide
SiO <sub>2</sub>	Silicon dioxide
Sn	Tin
SnO	Tin Oxide
SnO <sub>2</sub>	Tin Dioxide
TEC	Thermoelectric Cooler
TEGS	Thermal Energy Grid Storage
TES	Thermal Energy Storage
Tl	Thallium
TPV	Thermophotovoltaics
TZM	Molybdenum based alloy with Titanium and Zirconium
U	Velocity (m/s)
$\dot{V}$	Volumetric flow rate (m <sup>3</sup> s <sup>-1</sup> )
W	Tungsten
WC	Tungsten Carbide
XRD	X-ray Diffraction
Y <sub>2</sub> O <sub>3</sub>	Yttrium Oxide (Ytria)
ZrO <sub>2</sub>	Zirconium Dioxide (Zirconia)
ZTA	Zirconia Toughened Alumina
$\mu$	Dynamic Viscosity (Pa s)
$\rho$	Density (kg m <sup>-3</sup> )

## SUMMARY

Thermal energy is fundamental to most power generation and many industrial processes, and because of the entropy associated with it, it is the most valuable at the highest temperatures. To do useful work, this thermal energy must be transferred, and convection is the ideal mode to do so because it has the advantage of energy advection and is not geometrically limited. To enable convective heat transfer at extreme temperatures, molten metals are attractive heat transfer media because they can have high-temperature stability, high heat transfer coefficients, and low viscosity.

Although it would be incredibly enabling to be able to manipulate heat at extremely high temperatures ( $> 1000^{\circ}\text{C}$ ), it has proven extremely difficult. The challenges are primarily in materials, as there are few classes of materials that remain solid and chemically stable above  $1000^{\circ}\text{C}$ . Further, current systems rely on metals and polymers for pumps, seals, and containment. Thus, liquid heat transfer has been largely limited to  $400^{\circ}\text{C}$  with oils, and state-of-the-art solar thermal systems are limited to  $565^{\circ}\text{C}$ , using molten salts.

The ability to pump a fluid is key because it enables circulation and includes the thermal and chemical constraints seen by an entire system, with the added challenge of dynamic sealing, stress, and wear. In this extreme chemical and thermal environment, it was critical to broaden the materials search to include ceramics—which have historically been avoided because they are brittle. However, many ceramics can maintain their mechanical stiffness and thermodynamic stability with respect to several liquid metals at extreme temperatures, so it is valuable to try to accommodate their brittle nature.

If liquid metal heat transfer above 1000°C was enabled, many technologies that have previously been non-competitive economically may become viable. For example, thermal energy grid storage (TEGS), concentrated solar power (CSP), and thermophotovoltaics (TPV) could become cost competitive if they operated above 1000°C. Further, this technology can be applied to nuclear power generation and enable new solar fuel concepts. Many industrial processes can also be made more efficient or effective by employing energy advection at extreme temperatures, including manufacturing and waste heat recovery.

In this thesis, the first successful demonstration of an all-ceramic mechanical pump is reported. The pump was used to continuously circulate liquid tin (Sn) at a flow rate between 24-108 g/s and a temperature of ~1200°C, in an all ceramic circulation loop, for 72 hours without failure. Tests at higher temperatures were successful for shorter periods, without metered flow rate, reaching nearly 1500°C without failure. The system is expected to operate successfully at even higher temperatures, perhaps above 1600°C, but was limited by the combination of heat loss (largely from a flow viewport) and heater power input limitation. Here, an aluminum nitride/boron nitride composite, known as Shapal, was used to fabricate an external gear pump, which relied on a graphite packing dynamic seal. External gear pumps use the meshing of gears to pump fluid trapped in the cavity between the teeth around pump body, Because the two gears remain in contact, fluid cannot return through the center, so it is forced to the outlet.

In addition to the primary Shapal pump investigated, two metal pumps were developed. First, a pump of the same geometry was made from Inconel 625, coated with CrN, for applications below 600°C. This pump has performed reliably for over 80 hours of use. Another pump was made from tungsten, which can be used in direct contact with Sn.

This pump has so far only been tested to 650°C for eight hours, but it is expected to perform well at 1350°C, and even much higher temperatures.

The pump system includes the novel design of an extreme temperature shaft actuation system, which tolerates misalignment from thermal expansion and enables thermal separation of the motor. Further, the design and modeling of a circulation loop, weight based and visual flow meter, and extreme temperature thermal management system is discussed. All these components were fabricated from graphite, including permanent and removable joints/seals. The entire system was held in an inert nitrogen environment to prevent oxidation. Here, standard, economical techniques were used to create the hermetic seal with the ambient environment, so the capability can be scaled to industrial application. Although the pump did not mechanically fail in the reported tests, it did experience significant wear, which resulted in performance degradation. Suggestions for future design improvements to resolve this issue and broaden the capabilities of the system are also included.

This first of a kind demonstration represents a major technological breakthrough, because it now enables heat transfer using a liquid, above 1000°C. This capability is enabling, because the notion of transferring, storing and converting heat at such extreme temperatures has been previously considered infeasible. This new ability represents a major step forward for the fields of heat transfer, energy, and chemical/materials processing and many new concepts are enabled by this approach.

## CHAPTER 1. INTRODUCTION

Thermal energy is fundamental to the nearly all power generation and industrial processes, but most of it is wasted [1]. Despite its pervasiveness, thermal energy has the highest entropy per unit energy of any form of energy and has limited usefulness. Its greatest value in our society is when it can be converted to more useful forms of energy, such as mechanical/electrical work or portable potential energy (*e.g.*, batteries). Therefore, heat has its greatest value when it can be transported, stored and converted at the highest possible temperatures—that is, the highest exergy and, thus, lowest entropy.

Convection, unlike conduction and radiation, is the only way to transfer heat that is neither geometrically limited nor hampered by the conduction rate of solids [2]. That is, unlike conduction, convection has the added benefit of mass transfer which enables energy advection. Fluids available for convective heat transfer include gasses, liquids, and fluidized solids. However, gasses have inherently low mass/number density and therefore have low energy density. Fluidized solids also introduce complications and have low density because they must be moved by a bulk fluid. Liquids, though, are dense with high energy density and can be flexibly adapted to almost any configuration. Liquids are frequently used for heat transfer, from water to oil to molten salts, but these all lack high-temperature stability or high boiling points [3-5]. Increasing the fluid temperature can improve performance, but only a few liquids are stable above 1000°C, notably glasses and metals [3, 5, 6]. Glasses have high viscosity, high melting point, and low thermal conductivity, so they are not ideal working fluids because of the high pumping power required and their poor heat transfer characteristics [5, 7, 8].

Liquid metals, on the other hand, can have ideal properties including low viscosity—similar to that of water—immediately above their melting point. Thus, the pumping power required to circulate liquid metal in a closed loop can be very low, e.g., less than 1% of the energy transferred. Similarly, they have high electrical and, thus, thermal conductivity which, as convective heat transfer is directly proportional to thermal conductivity, and in combination with their high volumetric energy density, can result in 2-3 orders of magnitude increase in the heat transfer coefficient, compared to non-electrically conductive fluids, like oils and salts. Also, they can have a very large liquidus range (e.g., 232-2603°C for tin (Sn)), with low vapor pressure, enabling them to operate stably at extreme temperatures without decomposing or vaporizing. And, critically, they can be abundant, inexpensive and are already mass produced at high volumes [5, 9, 10]. Therefore, liquid metals are the optimum heat transfer medium for very high-temperature energy advection.

## **1.1 Challenges and State-of-the-Art**

Although it is theoretically attractive and would be incredibly enabling to be able to manipulate heat at extremely high temperatures ( $> 1000^{\circ}\text{C}$ ), from a practical standpoint, it has proven extremely difficult and in many cases, impossible. In the few exceptions, such as gas turbines and rocket engines, it is important to note that the heat is contained in a gas, and it isn't pumped/pressurized where it is hot—*i.e.*, pumps/compressors are positioned in the coldest section of the circulation loop, or it is an open system, so that the moving parts are not exposed to the high-temperature fluid. To take full advantage of extreme temperature liquid metal convective heat transfer, the ability to circulate and seal the fluid flow is critical. All the components required to achieve this are challenging, but the pump is the key component to enable high-temperature liquid metal heat transfer because it is

subject to the most difficult thermal, mechanical and chemical constraints in an entire circulation loop.

It is important to note that because mechanical force can be transmitted *through* a fluid, a pump can often be located at any point in a circulation loop. In many systems, the circulation loop is not isothermal and, therefore, the pump can be placed in the coldest part of the loop. For example, with Sn as the heat transfer fluid (HTF), the pump could operate in a part of the loop that is near 300°C, since the Sn would still be liquid. However, there are important applications that depend on the loop being nearly isothermal or require auxiliary pumping near the peak temperature. As detailed in the forthcoming Applications section in this chapter, thermal energy storage (TES) of a fluid such as silicon (Si) can operate on the latent heat of melting, at nearly constant temperature. This system can be paired with thermophotovoltaic (TPV) electricity generation for a potentially very high-efficiency system [11]. Additionally, industrial applications detailed in the section on Applications are mostly isothermal, and thus a pump that can operate at the peak system temperature is required.

Liquid heat transfer has been largely limited to 400°C via high-temperature oils, although molten salt concentrated solar power (CSP) has commercially achieved temperatures as high as 565°C [6]. Some industrial applications, including those from Hazelett and CMI Novacast, have reached as high as 750°C using electromagnetic pumps, even pumping at up to 900°C for peak periods. This approach is temperature limited by the current carrying wires; and, in a permanent magnet approach, it is limited by the Curie temperature of the magnetic components [12]. The active cooling required to protect these components would incur massive heat loss if designed for use above 1000°C.

Theoretically, current carrying wires could be made from a refractory metal, such as tungsten (W). In that case, the system could be maintained at the peak temperature, and heat loss would be reduced greatly. Still, electromagnetic pumps are remarkably inefficient (*e.g.*, often less than 1-5% [13]), and as a result, the aforementioned primary advantage of low pumping power for liquid metal would be forfeited if an electromagnetic pump were used. Based on these limitations, mechanical pumps are the focus of this work.

Ultimately, the challenges boil down to materials limitations, as there are few classes of materials that remain solid, chemically stable, and can exhibit long life at temperatures above 1000°C. Thus, the transport, storage and conversion of heat at extreme temperatures is often viewed as infeasible from an engineering perspective. For example, even the relatively inert liquid Sn will degrade or react with virtually every other metal on the periodic table. At high temperatures, mass diffusion and reaction kinetics are highly accelerated, and therefore any piping/containment infrastructure made of conventional structural metals attempting to contain Sn( $\ell$ ) will degrade quickly [14-17].

## **1.2 Solution Approach**

In this extreme chemical and thermal environment, it was critical to broaden the materials search for pumps, valves, piping, and seals. Instead of metals, one could utilize another class of materials, namely ceramics—defined here to broadly include any inorganic non-metallic material. Ceramics, however, have been largely discarded as an unrealistic option, because they are brittle [18, 19]. The assumption is that if ceramics were used, for example, in a mechanical pump, they would fail immediately or with a short life, due to their low fracture toughness. This is in principle their key drawback, though, and because

of their major advantages, detailed below, it is, therefore, worthwhile to consider clever ways of overcoming this issue to realize major advances.

It should be emphasized that many ceramics not only retain their mechanical stiffness at extreme temperatures [20-22], but they can also be thermodynamically stable with respect to certain liquid metals (*e.g.*, Sn, lead (Pb), bismuth (Bi), aluminum (Al), and silicon (Si)) [10, 23]. In Chapter 2, on Material Selection, the relative reactivity of several potential HTFs with containment materials is discussed. The notion of thermodynamic stability is critical to emphasize as this is fundamentally an atypical situation. Frequently, materials in contact have a thermodynamic driving force to react, but there is a kinetically limited step in the reaction that prevents the reaction from occurring at a significant rate [10]. In some cases, such as CSP, this issue is what sets the temperature limit, as the molten salt would quickly corrode the stainless-steel infrastructure above 565°C [4], but below this temperature, the kinetics are sufficiently limited to enable a 30-year power plant life. Similarly, the reaction kinetics of acids with metal containment can also increase with temperature. For example, naphthenic acid, which is present in crude oil, limits the temperature of refinery processes in order to limit the rate of corrosion [24]. Further, steam can corrode stainless steel above ~200°C, and especially where water is supercritical [25, 26]. In this case, the temperature is either restrained, or protective coatings are required.

Instead of operating in the regime of rate-limited reactions, with liquid metal in a ceramic infrastructure an entirely different scenario is possible, whereby the metal and ceramic are chosen such that there is simply little or no thermodynamic driving force for them to react in the first place. This situation is extremely desirable from a reliability standpoint because it implies that there is no material reaction/dissolution at any time scale.

Therefore, one need not be concerned that there is a chemical degradation mechanism in the system that could become exacerbated with time, such as the shedding of a protective barrier. Then, the key question was whether brittle ceramics could be used to circulate and seal liquid metals at extreme temperatures ( $>1000^{\circ}\text{C}$ ), without breaking or leaking.

Given these considerations, the approach of this project was focused on enabling a mechanical pump and the auxiliary system to continuously circulate liquid metal above  $1000^{\circ}\text{C}$ . Key to achieving this goal was avoidance of low cycle brittle fracture of ceramics in rotating machinery and demonstrating the ability to seal liquid metal above  $1000^{\circ}\text{C}$ . These were the critical risks to address and it is clear that if the technology to enable liquid metal heat transfer above  $1000^{\circ}\text{C}$  existed, it would unlock new concepts in power generation, chemical/metals processing and beyond [2, 11, 23, 27-33].

### **1.3 Applications**

The ability to pump liquid metals above  $1000^{\circ}\text{C}$  is particularly enabling because they have low viscosity and high thermal conductivity, thereby leading to extremely high heat transfer coefficients. This, in combination with their high-temperature stability, suggests that they can be used in applications where high-temperature heat would be normally wasted. Similarly, they can be used to collect and store or convert heat to deliver high-value energy.

For example, CSP at twice the current peak temperature is enabled by this approach [11, 34], which can have a transformative impact on reducing cost. Such a high-temperature increase is expected to result in an efficiency increase of approximately 50% (relative) and can reduce the cost by 20-30% [5, 35, 36]. This route to achieving lower cost

is particularly attractive given that even lower temperature approaches (700-800°C) are slated to achieve parity with natural gas [37, 38]. Moreover, this ability to move heat at high temperatures can enable high-temperature nuclear power generation [17, 27] and can more generally enable high exergy thermal energy storage (TES) [30] and new solar fuels concepts [39]. Although non-intuitive, this technology can even make thermal energy grid storage (TEGS) economically viable, which can become very profitable (and necessary) if non-dispatchable renewables increase in market share [40]. There have already been several efforts to commercialize TEGS, by companies such as Siemens, Isentropic, and others, at varying stages of development, but all at much lower temperatures—as noted in Appendix A. By operating at the extremely high temperatures enabled by the usage of ceramics and liquid metals, the efficiency of such a system can approach > 60%, which would render the economics competitive with low-cost resources, such as pumped hydro.

Other new and innovative components are also enabled by this new approach. For example, wherever heat exchange at high temperatures with gas is needed, Sn could be used as an intermediate heat transfer fluid to drastically reduce the amount of surface area, and therefore cost and pumping power, required. This can be facilitated by using the liquid metal to transfer heat to and from a noble gas, such as helium via direct contact liquid droplet heat exchangers [5, 28, 29]. Such heat exchangers can be extremely efficient and can even take advantage of the heat of solidification [41], which is particularly large for materials such as silicon [11]. Just as liquid metals can help transport and store energy, they can also enable improvements to existing power cycles. For example, in gas turbines where up to 5% of the cycle efficiency is lost because of turbine blade cooling, the very high heat transfer coefficients obtained by liquid metals could theoretically be used to cool

turbine blades, and the heat could even be used to preheat combustion gasses [42]. Similarly, the ability to move heat at such extreme temperatures could make thermophotovoltaic (TPV) solid-state thermal-to-electricity conversion competitive as a CSP heat engine [11].

Furthermore, many industrial processes occur at high temperatures [2, 31-33, 43] and can be made more efficient or effective by employing the ability to pump liquid metal at extreme temperatures. For example, high-pressure injection molding of metal alloys can increase the speed and quality of castings, with less oxidation and without the geometric limits of current methods [31]. Similarly, by pumping liquid metal, one can have precise control over the cooling rate in single crystal super alloy castings to optimize the final properties [43]. There are also numerous industries where high-temperature waste heat is available and could be recovered/internally recycled or converted to electricity to ultimately reduce costs, *e.g.*, aluminum processing [32, 33].

Thus, it has been established that many important applications exist for liquid metal heat transfer above 1000°C. In fact, because nearly all power generation fundamentally relies on thermal energy, which is most valuable at the highest temperatures, developing technology that enables efficient heat transfer at higher temperature can increase the efficiency of the vast majority of power generation processes—a multi-terawatt market. However, the challenges that have so far prevented this technology from being developed—namely the extreme chemical and thermal environment—will be difficult to solve. Therefore, the question was posed: can a pump be designed from ceramics to circulate liquid metal that survives this extreme environment with long life, and without breaking or leaking?

Based on this question, Chapter 2 first lays out the selection of a gas environment and target temperature for a prototype system, and then a comparison of liquid metal candidates, as well as potential containment materials is considered. Next, in Chapter 3, the design of the pump system—containing the design/selection of pump materials, type, sealing, mounting, and actuation—is discussed. Chapter 4 details the experimental setup which includes the design of a circulation loop, in addition to a novel flow meter and the thermal management equipment used. Finally, Chapter 5 presents the primary results of experiments, including a section on initial failures and a discussion of future work, followed by concluding remarks in Chapter 6.

## CHAPTER 2. MATERIAL SELECTION

Extreme temperature liquid metal convective heat transfer presents a very challenging environment for the associated piping network and circulation components (e.g., pumps and valves). Why is liquid metal such a challenging environment? Firstly, metals are inherently unstable, as they are essentially ions floating in a sea of electrons. Thus, they easily react with non-metals and metalloids to form relatively stable ceramics. Similarly, the majority of metals have substantial solubility in other metals, so they may also form alloys.

For this reason, solid metals are rarely suitable to contain liquid metals, especially at extreme temperatures where reaction kinetics are accelerated. However, by considering ceramics as potential materials for contact with molten metals, the problem of containment becomes tractable. Ceramics are of interest because their strong, stiff covalent and/or ionic bonds, make them highly resistant to attack. Similarly, the rigid bonds in ceramics cause atoms to rest in a deep and narrow potential energy well, which results in their refractory nature and low expansion with temperature. That is, the minimum energy in ceramic bonds is highly negative and the location/bond distance of this minimum is not highly variant with temperature. This is in contrast to metals, where the potential well is relatively wide and shallow—thus, in general, metal bonds can be broken more easily and they experience greater expansion with temperature. Unfortunately, the same quality that makes ceramics stable also makes them brittle. Here, although ceramic bonds are strong, they can tolerate little plastic deformation. Interestingly, refractory metals introduce a useful blend of the high-temperature strength and low thermal expansion of ceramics with the ductility of metals, albeit without the same level of chemical stability of ceramics. The similarity of properties between ceramics and refractory metals is a result of similarly shaped potential wells, as both materials exhibit strong, stiff bonds.

Therefore, before approaching a solution, it was critical to define the system conditions and systematically compare candidate fluids and containment materials. Once a fluid was selected and incompatible solids containment materials were eliminated, design began. Although many studies have been conducted, especially recently, with respect to the reactivity of liquid metals at elevated temperatures, most experiments are limited to below 1000°C [10]. Therefore, based on the group of materials that appeared attractive from a thermodynamic standpoint, material testing was conducted by collaborators at The Georgia Institute of Technology [44].

## **2.1 Temperature**

Based on the practical limits of heaters, insulation, and stability of certain ceramic containment materials of interest, a temperature of ~1350°C was targeted. This isn't a fundamental limit of the technology developed, but instead a balance between confirming the system can survive extreme temperatures and experimental practicality. Although several applications require the pump to operate at the peak system temperature for many applications the circulation loop is not isothermal (see Introduction). In these systems, the pump can operate marginally above the fluid's melting temperature, and the design criteria for this medium temperature pump is included as well.

## **2.2 Gas Environment**

Early in the selection process, it was clear that oxygen sets severe limitations on temperature/material options. Therefore, to prevent oxidation of the molten metal working fluid and to enable other materials, which could suffer oxidation, the entire system was held in an inert environment. To balance this requirement with practical limitations, especially on a commercial scale, high purity nitrogen (N<sub>2</sub>) at (or slightly above)

atmospheric pressure was selected. The key principle here is that if the high-temperature components are kept in an inert environment, the hermetic seal between that environment and the atmosphere can be cold. Therefore, this approach removes the need for high temperature, high-pressure hermetic seals and can be implemented with commercially available polymer-based sealing materials. Furthermore, large low oxygen environments are frequently used commercially, *e.g.*, controlled atmosphere (CA) storage of tree fruits and electronics fabrication using the Czochralski processes [45-48]. As discussed in Chapter 4 on the Experimental Setup, oxygen partial pressure below  $1 \times 10^{-15}$  atm was consistently achieved.

### **2.3 Heat Transfer Fluid**

The requirements for HTFs of interest include low melting temperature, boiling/dissociation temperature above 1350°C, high thermal conductivity, low viscosity, and acceptable safety/corrosion behavior. As discussed in the introduction, at temperatures above 1000°C the options for heat transfer fluids are very limited. Having down selected to liquid metals, after eliminating glasses and gasses for their high viscosity and low density, respectively, metals are now compared.

In general, among the liquid metals that have acceptable liquidus ranges, the key was to determine their degradation behavior in contact with potential containment materials. Degradation can occur by reactive or non-reactive wetting of the solid by the liquid metal, which can allow penetration of molten metals into prospective containment materials. Thus, a nonwetting combination was ideal, as this case limits reactions to the interface surface and prevents damage by penetration through the wetting of grain boundaries, which

can dramatically lower the strength of the solid. Nonwetting is also key for leak prevention, either through the wall of a containment vessel, or at static and dynamic seals.

Either through wetting or confined to the interface surface, corrosion by liquid metals can occur through several processes including dissolution, oxidation, carburization, and the formation of intermetallic compounds [15]. Whether these corrosion mechanisms will occur depends first on the thermodynamic data of the liquid/solid material set considered—*e.g.*, phase and Ellingham diagrams depict equilibrium phases and their relative stability, respectively, based on their Gibbs free energy ( $G = H - TS$ , where H is enthalpy, T is temperature, and S is entropy). Remarkably, even once a fluid reaches its solubility limit with the constituents of a containment material, because circulation loops are always non-isothermal to some degree and solubility can be a function of temperature, dissolution will occur in hot zones and deposition will occur in colder regions of the system. This can then lead to major failures over time as a portion of the solid containment system can be removed and deposited elsewhere over time, ultimately resulting in an eventual blockage/constriction of flow. For example, in lithium (Li) cooled nuclear reactors, 316 stainless steel is considered as a containment material, however, the solubility of chromium (Cr), nickel (Ni), and iron (Fe) in Li increase with temperature. Thus, these metals deposit in colder portions of a convection loop, where the solubility is lower [49]. This issue has been found to be more immediate than the issue of material loss in the hotter portions of the loop.

The extent to which this effects the life of a system depends on the temperature gradient, the solubility gradient, and the solubility limit, among other factors. As is the case for several material combinations discussed below, if there is little or no thermodynamic

driving force for corrosion, there can be negligible reaction at any time scale—without reliance a protective scale.

Notably, if a reaction is predicted, thermodynamic data is insufficient to determine whether the phases predicted will actually form at an observable time scale, or the rate at which corrosion would occur. Here, kinetics data is necessary, and experimental validation is the ideal way to confirm whether appreciable corrosion will occur. For example, protective scales can form between two reacting materials, which may reduce corrosion to an acceptable rate (if the scale is thermodynamically stable and does not shed), where the life of a system can be many years.

**Table 1:** Compatibility of representative candidate fluids and some unprotected containment materials up to 1350°C. Adapted from [10, 50] and various sources in the open literature, including recent results for Sn at 1350°C from [44]. ✓ indicates good compatibility (corrosion rate below 1 mil/year (25.4 µm/year)); — limited (between 1 and 10 mils/year); × poor (larger than 10 mils/year). \*SiC can have good stability with Sn if ~0.5% Si is added.

Fluid Temperature °C	Na 300	Na 600	Na 800	PbBi 300	PbBi 600	PbBi 800	Sn 300	Sn 600	Sn 1350
<b>Ferrous metals</b>									
Pure iron	✓	✓	✓	✓	✓	—	—	×	×
Mild-carbon steel	✓	—	×	✓	—	×	—	×	×
Low chromium steel	✓	—	×	✓	?	?	—	×	×
2 to 9% chromium-steel	✓	✓	—	✓	—	—	—	×	×
Ferritic stainless steel	✓	✓	✓	✓	—	—	—	×	×
Austenitic stainless steel	✓	✓	✓	—	—	×	—	×	×
Gray cast iron	—	×	×	?	?	?	—	×	×
<b>Non-ferrous metals</b>									
Aluminum	×	×	×	×	×	×	×	×	×
Beryllium	✓	✓	—	✓	✓	—	✓	✓	×
Chromium	✓	✓	✓	✓	—	—	✓	—	×
Copper alloys (with Al, Si, Be)	✓	✓	×	×	×	×	×	×	×
Copper alloys (with Zn, Sn)	✓	—	×	×	×	×	×	×	×
Cobalt-base alloys	✓	✓	✓	?	?	?	×	×	×
Nickel alloys (with Fe, Cr, Mo)	✓	✓	✓	×	×	×	×	×	×
Nickel alloys (with copper)	✓	✓	—	×	×	×	×	×	×
Refractory metals (Mo, Nb, Ta)	✓	✓	✓	✓	✓	✓	✓	✓	×
Refractory metals (W)	✓	✓	✓	✓	✓	✓	✓	✓	✓
Platinum, gold, silver	×	×	×	×	×	×	×	×	×
Titanium	✓	✓	—	✓	—	×	✓	×	×
Zirconium	✓	✓	—	✓	—	×	✓	×	×
<b>Non-metals</b>									
Alumina (dense)	✓	—	—	✓	✓	✓	✓	✓	✓
Graphite (dense)	✓	✓	—	✓	✓	—	✓	✓	✓
Fused quartz glass (SiO <sub>2</sub> )	✓	—	×	✓	✓	—	✓	✓	×
Aluminum Nitride (AlN)	?	?	?	✓	✓	✓	✓	✓	✓
Silicon Carbide (SiC)	✓	✓	✓	✓	✓	✓	✓	✓	—*
Mullite (3Al <sub>2</sub> O <sub>3</sub> ·2SiO <sub>2</sub> )	✓	—	?	✓	✓	—	✓	✓	✓

Alkali metals, although of interest in several studies [6, 10], are infeasible at the target temperature of 1350°C because of their relatively low boiling points and high reactivity. Historically, alkali metals have been favored because of their compatibility with

several metal-based containment materials at moderate temperatures (up to  $\sim 800^\circ\text{C}$ ). Table 1 lists several metals, including iron and nickel based alloys that are compatible with sodium. Sodium (Na) and potassium (K) are generally considered to have the most desirable properties among alkali metals, but their low boiling points (below  $900^\circ\text{C}$ ) make them unusable in extreme temperature applications. Even at these lower temperatures, Na can be unstable in contact with several ceramics, including alumina ( $\text{Al}_2\text{O}_3$ ) and silica ( $\text{SiO}_2$ ) [10]. Here, porous ceramics are penetrated and dissolved by Na, even though they are thermodynamically stable—thus, ceramics must be sufficiently dense to resist attack [50]. Of the Alkalis, the only metal that remains liquid near the target temperature is lithium. Unfortunately, lithium is both expensive ( $\$60\text{ kg}^{-1}$  or  $\$14.4\text{ K kJ}^{-1}$ ) as shown in Table 2, and highly reactive, reacting with most ceramics near its melting temperature of  $180^\circ\text{C}$  [51].

**Table 2:** Properties and cost of selected liquid metals at  $600^\circ\text{C}$

Fluid	Mass Heat Capacity ( $\text{J g}^{-1}\text{ K}^{-1}$ )	Molar Heat Capacity ( $\text{J mol}^{-1}\text{ K}^{-1}$ )	Volumetric Heat Capacity ( $\text{J m}^{-3}\text{ K}^{-1}$ )	Cost per mass ( $\text{\$ kg}^{-1}$ )	Cost per Energy ( $\text{\$ K kJ}^{-1}$ )
Li	4.16	28.70	1976	60	14.4
Na	1.25	28.75	1010	2	1.6
Al	1.15	31.05	3105	2	1.7
K	0.76	29.72	536	2	2.6
Ga	0.36	25.09	2192	600	1666.7
In	0.24	27.55	1601	500	2083.3
Sn	0.24	28.49	1519	25	104.2
Th	0.135	27.59	1600	88	651.9
Pb	0.15	31.08	1491	2	13.3
Bi	0.15	31.35	1549	22	146.7

Only a few other metals have acceptable liquidus ranges. Among these are the group 13 and 14 elements, including several low ( $< 400^\circ\text{C}$ ) melting point metals and aluminum. Al is inexpensive ( $\sim \$2\text{ kg}^{-1}$ ) and has the highest volumetric heat capacity ( $3100\text{ J m}^{-3}\text{ K}^{-1}$ )

of the fluids considered in Table 2, however, it is highly reactive with other metals, and no known metal or alloy is unattacked by molten aluminum, even near its melting point [50]. Volumetric heat capacity is especially important if a fluid is to be used for energy storage, because it controls the tank size required to store a fixed energy amount—which influences cost and heat loss. Further, Al is relatively reactive with oxide ceramics, because it forms a very stable oxide ( $\text{Al}_2\text{O}_3$ ). Similarly, Al forms a stable nitride and carbide. Thus, in general, Al is neither stable with respect to metals or ceramics, unless they contain a strong Al content to begin with. Of the group 13 and 14 metals that melt below  $400^\circ\text{C}$  and boil above  $1350^\circ\text{C}$ , there are only six, namely thallium (Tl), gallium (Ga), indium (In), Bi, Pb, and Sn. Tl has high cost ( $\$88 \text{ kg}^{-1}$  or  $\$682 \text{ K kJ}^{-1}$ ) and toxicity. Pb and Bi, and especially lead-bismuth eutectic (LBE), are heavily studied and are attractive, except for having relatively low thermal conductivity, high toxicity and environmental contamination risks [50]. Furthermore, there is a lack of a high-temperature containment materials, as there currently has been no success above  $750^\circ\text{C}$  [10, 52]. Ga and In, which are very otherwise attractive because of their stability with ceramics and low melting points ( $30^\circ\text{C}$  and  $157^\circ\text{C}$ , respectively), are prohibitively expensive, with costs above  $\$500 \text{ kg}^{-1}$  or  $\$1600 \text{ K kJ}^{-1}$  [10].

Molten Sn, although reactive with most other metals, is stable with respect to several ceramics. Because Sn has a relatively low affinity for oxygen ( $\text{O}_2$ ),  $\text{N}_2$ , and carbon (C), it can be used in contact with many ceramics including C,  $\text{Al}_2\text{O}_3$ , SiC, BN, AlN and mullite ( $3\text{Al}_2\text{O}_3 \cdot 2\text{SiO}_2$ ) at  $1350^\circ\text{C}$  without appreciable chemical interaction. Additionally, it is inexpensive ( $\$25 \text{ kg}^{-1}$  or  $\$104 \text{ K kJ}^{-1}$ ) compared to several options such as Ga, In, and Bi [10] and is sufficiently inexpensive for use as a heat transfer fluid (HTF) in multiple

applications [5, 10]. Importantly, Sn also has a very wide liquidus range (232-2603°C) and high thermal conductivity ( $\sim 30 \text{ W m}^{-1}\text{K}^{-1}$ ), especially compared to oils and water. It also has low vapor pressure—less than 10 Pa at 1350°C. Therefore, as the least expensive extreme-temperature capable metal, Sn was selected as the primary HTF to evaluate in this study.

## 2.4 Potential Containment Materials

With molten Sn selected as the HTF, and the temperature and gas environment carefully chosen, potential containment materials were then considered. While the extreme temperature and corrosive liquid metal environment limit the material options, the inert gas environment widens the possibilities considerably, compared to air. The functions of these containment materials vary from simple bulk reservoirs and pipes to dynamic mechanical components and seals. For this reason, although mechanical properties are important, this section focuses on a wide array of *potential* containment materials—evaluating only reactivity/stability. Additional properties are discussed on a part by part basis in Chapter 3, on the Design and Modeling of The Pump System.

As noted, in many applications heat transfer circulation loops are not isothermal and in fact, one part of the loop may remain relatively cold. With molten Sn as the HTF, the minimum temperature is the melting temperature of Sn, 232°C. Therefore, for components that may be located in the cold section of a system, several compatible materials were identified.

In this moderate temperature regime, several metals are thermally stable, but few (see Table 1 above) are thermodynamically compatible with Sn. For this reason, iron and

nickel based alloys would only survive long-term use if a stable, protective barrier coating could be applied to prevent direct contact between molten Sn and the containment metal. This fact was realized early on in experimentation, as described in the section on Medium Temperature Pumps, in Chapter 3. Although several coating options exist, including SiO<sub>2</sub>, CrN, Al<sub>2</sub>O<sub>3</sub>, Al<sub>2</sub>TiO<sub>5</sub>, and others, their selection must be made with respect to the base metal [53]. This is because the two materials must be well matched with respect to chemical compatibility and thermal expansion; the coating may also need to stand up to wear and abrasion. Here, a bond layer of an alternative material, such as NiCrAlY can be used to bridge the bond between the main two materials. As the application temperature increases, the options for stable coatings narrow. Here, thermal expansion and thermal stability of the coating become key issues [54]. As noted above, ceramics and most metals are thermal expansion mismatched because of the shape of their respective potential energy wells—which is fundamentally because of the different type of bonding the two materials experience. Here, metal bonding is weaker, which results in larger expansion with temperature. In the experiments described in this thesis, coated metals were limited to 600°C.

Above 1000°C, both the low stiffness of many metals and the lack of reliable high temperature coatings necessitates the use of a containment material with bulk chemical stability. While molten Sn is incompatible in direct contact with most metals, it is stable with many ceramics, even beyond 1350°C. Here, the fundamental aspect of ceramics, namely their strong, stiff bonds, make them highly resistant to attack by Sn because it forms relatively weak oxides [55] and nitrides [56], and does not form a stable boride or carbide at ambient pressure; thus, it can be brought into contact with many oxides, nitrides, borides,

and carbides without appreciable reaction. Further, while Sn wets most metals, it is nonwetting on many ceramics, as experimentally verified at 1350°C for C, SiC, and Mullite [44].

As Sn forms a weak oxide, it is stable at the application temperature in contact with Al<sub>2</sub>O<sub>3</sub>, ZrO<sub>2</sub>, SiO<sub>2</sub>, CaO, and other oxide ceramics [55]. Further, many oxide-based technical ceramics have been developed in the last few decades with improved mechanical properties and thermal/chemical stability. For example, ZrO<sub>2</sub> (often of interest because of its very low thermal conductivity ( $\sim 2 \text{ W m}^{-1}\text{K}^{-1}$ ) is rarely used in its pure form because it undergoes a phase transformation from monoclinic to tetragonal at 1173°C, where it experiences a major volume change of about 9% [57]. This volume change causes macroscopic polycrystalline parts to immediately break apart. Instead, it is stabilized with magnesium (Mg) or yttria (Y<sub>2</sub>O<sub>3</sub>) in order to maintain the tetragonal phase at room temperature. The highest temperature stability of ZrO<sub>2</sub> is achieved when it is fully stabilized, that is, it is doped with 8 at% Y<sub>2</sub>O<sub>3</sub>.

Another interesting family of technical ceramics are the composites of Al<sub>2</sub>O<sub>3</sub> and zirconia. Known as ZTA, zirconia toughened alumina (2-20% ZrO<sub>2</sub>) exhibits very hardness (1650 HV kg mm<sup>-2</sup>) and fracture toughness (7.3 MPa m<sup>0.5</sup>). The mechanism by which the Al<sub>2</sub>O<sub>3</sub> is toughened is known as stress-induced transformation toughening, and is based on the phase transformation of the ZrO<sub>2</sub> particles, which are distributed throughout the bulk Al<sub>2</sub>O<sub>3</sub>, under applied stress. This transformation is accompanied by a volume increase of the zirconia particles which can prevent crack propagation through crack tip shielding—where the crack tip is compressed [58]. Other composites are of interest exist including alumina-silicates and CaO doped Al<sub>2</sub>O<sub>3</sub> hybrids.

Although oxide ceramics, such as  $\text{Al}_2\text{O}_3$ ,  $\text{ZrO}_2$ ,  $\text{SiO}_2$ , and their alloys, can be stable in atmospheric air to temperatures beyond  $1350^\circ\text{C}$ , there are several materials of interest that are critically enabled by the inert ( $\text{N}_2$ ) gas environment selected. Prominently, both C and tungsten (W) are limited to  $\sim 500^\circ\text{C}$  in air to prevent substantial oxidation rates [59, 60]. However, in a nitrogen environment, and even in contact with Sn, they are stable even beyond the  $2603^\circ\text{C}$  boiling point of Sn [61, 62]. Rhenium (Re) and Cr are also chemically compatible with Sn and  $\text{N}_2$  [63, 64], but Re is prohibitively expensive. Cr has very low strength and a high dissolution rate in Sn—over 12 at% at  $1350^\circ\text{C}$ . However, C and W have several attractive properties that will be discussed in detail in the next chapter, most notably low cost and high strength, respectively.

Of the three common allotropes of C (amorphous carbon, graphite, and diamond), the most practical for this application was graphite—because of the low cost and machinability. However, even amongst graphite, there are several forms and many grades. Here, one can take advantage of this assortment, where amorphous graphite can be used for components requiring (moderate) mechanical strength, while other grades can be used elsewhere, and all will be compatible with Sn. Several grades of varied particle size and purity are commercially available. Similarly, flexible graphite made from crystalline graphite flakes can be used for sealing since it can be soft and compliant. Graphite is one of the very few materials that can be flexible, thermally stable, and chemically inert with respect to the other elements present in this molten Sn system.

Many non-oxide ceramics are also enabled for use at  $1350^\circ\text{C}$  by the inert environment used, including AlN, BN,  $\text{Si}_3\text{N}_4$ , and others [65, 66]. These ceramics, in addition to SiC and WC, are compatible with Sn because of the lack of a stable tin carbide

or strong nitride. AlN and SiC are especially attractive because they can also be relatively stable with respect to other liquid metals of interest, like Al (although stability with SiC can be increased by adding Si to Al). In addition to these pure ceramics, composite materials such as Shapal Hi-M Soft™ have been developed which leverage the advantages of different materials. Here, Shapal is an 80/20 mix of AlN and BN with C, Ca, and Si as the major impurities (on the order of 100 ppm). This material is specifically designed to be machined in its fully fired state, which makes its precision fabrication economical, unlike most ceramics.

Several materials considered are sensitive to water vapor ( $\text{H}_2\text{O}(\text{g})$ ), especially at elevated temperatures. For example, even at moderate temperatures of  $\sim 300^\circ\text{C}$ ,  $\text{ZrO}_2$  experiences loss of mechanical strength when exposed to water vapor [67]. Similarly,  $\text{H}_2\text{O}(\text{g})$  accelerates the oxidation kinetics of AlN and can even oxidize it directly above  $1150^\circ\text{C}$  [68]. At the extreme temperatures present, all the oxidation-prone materials considered are susceptible to oxidation from water vapor; thus, it was important to minimize the  $\text{H}_2\text{O}(\text{g})$  in the gas environment. As described in the section on the Nitrogen Chamber, this was achieved by purging the chamber with dried ultra-high purity  $\text{N}_2$  and including moisture absorbing DampRid in the chamber.

Thus, having selected Sn as the primary HTF under study, there are many potential containment materials—including many ceramics and even some metals—that are thermodynamically compatible. Then, with an  $\text{N}_2$  gas environment and a target temperature of  $1350^\circ\text{C}$  selected as conditions for a prototype pump system, detailed design of the pump system then began.

## **CHAPTER 3. DESIGN AND MODELING OF THE PUMP SYSTEM**

Continuous circulation of a heat transfer fluid is fundamental to taking advantage of its energy advection capabilities. Therefore, it was necessary to design a pump to transport molten Sn. As discussed in Chapter 1 electromagnetic pumps were eliminated because of their low efficiency, high heat loss, and low-temperature limit [12, 13]. Having narrowed the design to a mechanical pump, mechanical material properties including tensile strength and fracture toughness were key to consider, in addition to thermal and thermodynamic properties. In the following sections, the Pump Type selected is discussed, followed by the Primary Pump Materials selected. Next, the issue of Pump Sealing (especially dynamic sealing) is included, followed by a description of the methods of Pump Mounting and Pump Actuation. Each of these sections presents unique issues associated with the extreme thermal and chemical environment.

### **3.1 Pump Type**

To choose a type of pump, several high-level configurations were considered including positive displacement, velocity, and electromagnetic pumps. The low efficiency, high heat loss, and low-temperature limit of electromagnetic pumps led to the elimination of that type from consideration [12, 13]. For many applications (including this lab scale experiment) displacement pumps are attractive because they provide an approximately constant flow rate, given a fixed input (e.g., rpm), at variable pressures [69-71]. On the other hand, velocity pumps have less flow rate control and require operation above ~500 rpm to achieve adequate performance—and much higher for peak performance. Also, electromagnetic pumps, and many velocity pumps, are very limited in the pressure head

they can deliver. Further, electromagnetic pumps cannot separate all electric components from the pump, unlike a mechanical pump. Based on these considerations, the family of positive displacement pumps was selected.

Within the realm of positive displacement pumps, external gear pumps offer a very simple design, requiring minimal components and simple machining techniques. Moreover, unlike internal gear pumps, this pump type doesn't require thin or flexible components, which is critical in this temperature regime. Among external gear pumps, several options exist for the gear tooth geometry. Straight spur teeth, unlike helix or herringbone designs (see Figure 66), are very simple to machine and enable very low (~100 rpm) speed operation because the flat gear teeth can form a nearly complete seal (even at zero rotational speed). This simplicity of machining was especially important for prototyping, because many ceramics must be ground to final dimension after firing—therefore this approach was able to reduce cost and lead time considerably. Further, unlike electromagnetic pumps, this mechanical pump enabled the separation of the pump and the electrical system that delivered the torque, thus protecting the polymers and metals in the electronics, while minimizing heat loss.

The final pump geometry, which was held constant for all the pumps tested (of varied materials), was an external gear pump with straight spur gears. Each gear has seven teeth an involute profile, and a standard 20° pressure angle—as shown in Figure 1B. The involute gear profile is the most common type, and refers to the fact that the gear tooth shape is determined by the path a point on a string would follow as the string is unwound from one gear base circle onto the other, as shown in Figure 1A. An animated version of this figure is available online [72]. The outer diameter of the gears was nominally 1.5

inches, and based on the tooth geometry this results in a theoretical (upper bound) flow rate of  $15 \text{ ml rev}^{-1}$  (1 gpm at 250 rpm). This geometry, and the pump flow path (which is common to all external gear pumps) is shown in Figure 2. In each pump, the pump gears are enclosed in a two-part cavity: a body (shown in Figure 2) and a cover. The inlet/outlet ports are located on the cover, rather than on the left and right of the pump as is common among commercial gear pumps.

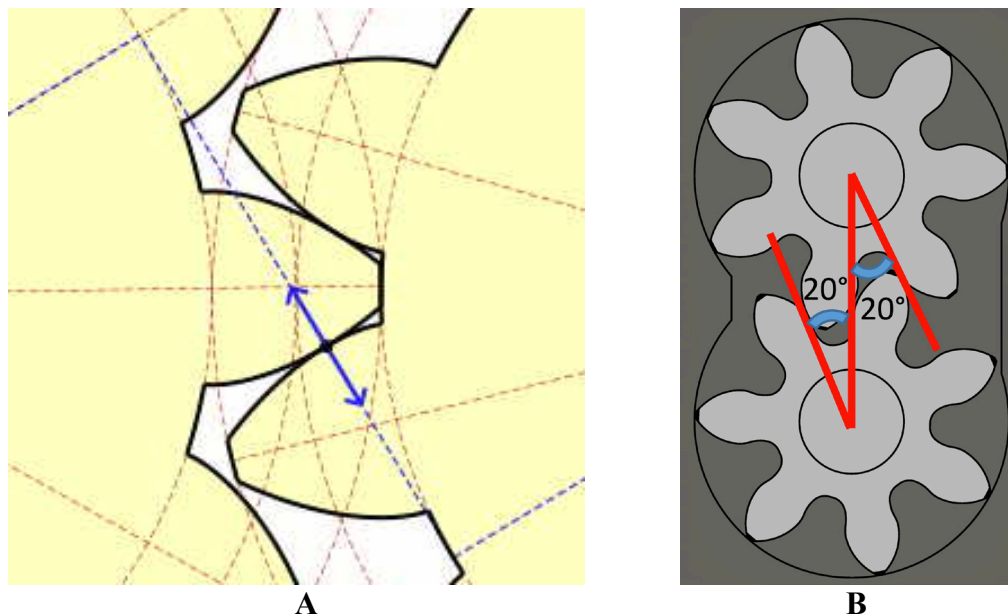


**Figure 1A:** Mapping of involute profile to create gear tooth profile. The black point moves in the direction of the blue arrows, while the gears rotate, to form the tooth shape. Here, the gear tooth shape is determined by the path the point on a string would follow as the string is unwound from one gear base circle onto the other. **B:** The pressure angle of an external gear pump is the angle between a line connecting the center of the two gears and a line tangent to the tangent plane of contact between the gear teeth. A larger angle puts less stress on the teeth, but more force on the gear shafts, which causes increased friction, wear, and power consumption.

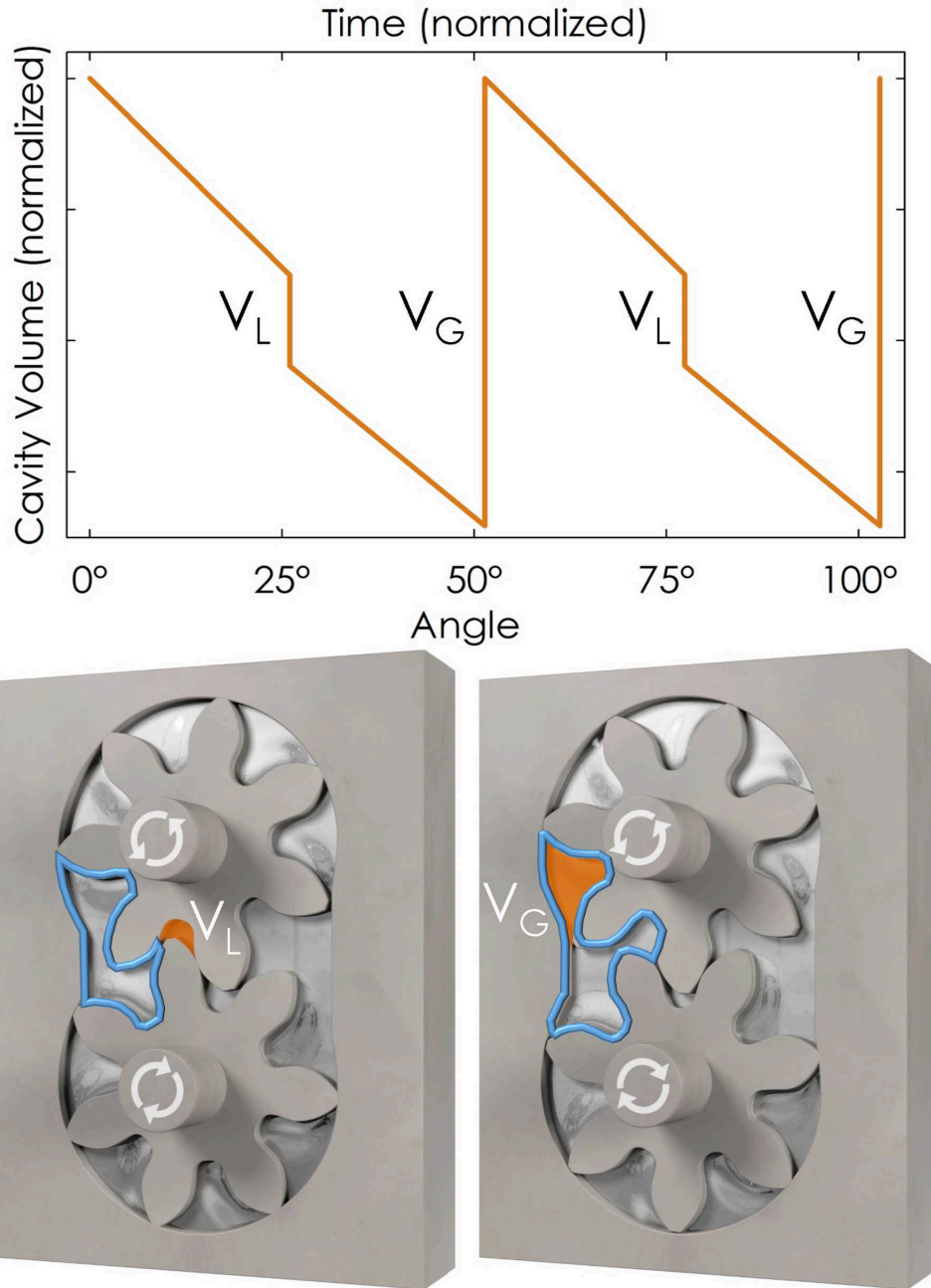


**Figure 2:** The model of the pump gears on the bottom illustrates the direction of gear rotation with a plot showing how the volume near the outlet (in blue) changes with rotation. Gear pumps use the meshing of gears to pump fluid trapped in the cavity between the teeth around the outside of the gears. Because the gears remain in contact, fluid cannot return through the center, so it is forced out of the outlet. In this design, there are 7 teeth, so the rotation per period is  $\sim 52^\circ$ . The two discontinuities in the plot are associated with transition points where the volume in the outlet region is abruptly included ( $V_G$ ), and abruptly removed ( $V_L$ ), as shown in the bottom right and left, respectively, highlighted in orange. The slope of the volume vs. angle or time is the volumetric flow rate and is theoretically constant for a fixed rotational speed of the gears.

### 3.2 Primary Pump Material

In this application, pump components, which rely on small clearances to perform well, needed to be very well matched in terms of thermal expansion—because of the wide range of temperatures through which this pump functioned. For example, the gears and the cavity they rest within should have minimal clearance ( $\sim 50 \mu\text{m}$ ). However, as the pump is heated, if the gears and pump body were made from different materials, this clearance could increase and reduce the pump performance by allowing increased internal-circulation. On the other hand, this clearance could also decrease, depending on the materials used, and could easily become negative, which would cause the pump to seize and not rotate. If the pump would only be used at a specific temperature, it could be designed to have the appropriate clearance at that temperature, but in order to enable pumping at a range of temperatures, it is necessary to match the expansion with temperature. Therefore, it was ideal to use the same material for all components along the flow path, pending other limitations. This is a major, novel constraint on the design of a pump, as pumps usually leverage the relative advantages of multiple materials, including metals of varied hardness and polymers for the gears, pump body, bearings, and seals.

As detailed in Chapter 4, graphite pipes were used to transport the molten Sn, and it was therefore necessary to select pump materials with a similar coefficient of thermal expansion (CTE) to graphite ( $\sim 5.0 \times 10^{-6} \text{ K}^{-1}$ ). Although thermal expansion is related to the melting temperature of a material, as noted above, even among refractory materials expansion coefficients range from  $\sim 0.5 \times 10^{-6} \text{ K}^{-1}$  to  $\sim 12 \times 10^{-6} \text{ K}^{-1}$ . It is important to note that because thermal expansion generally varies non-linearly with respect to temperature, the

maximum expansion mismatch can occur at temperatures below the peak temperature, so this was taken into account during the material selection process.

In many applications, the circulation loop is not isothermal, and the pump can be located at the coldest point in the loop, in this case  $\sim 300^{\circ}\text{C}$ . On the other hand, as discussed in Chapter 1, several important applications require the pump to operate near the peak system temperature [11, 31-33]. For this reason, multiple pumps were designed, to meet the different use cases. Also, although C is thermodynamically compatible with Sn, it was not used as a mechanical component in the pump because of its poor strength and wear properties. Strength—especially tensile strength—and wear properties are important for gear pumps because the gear teeth are subject to bending stress, and the gears and shafts experience sliding wear.

### *3.2.1 Medium Temperature Pumps*

Since some applications enable the use of a medium temperature ( $\sim 300^{\circ}\text{C}$ ) pump, naturally the first step was to design a pump compatible with molten Sn that could operate in this range. At these moderate temperatures, the thermal expansion mismatch between the pump and pipes causes less absolute discrepancy, and therefore a wider array of materials can be used, from this perspective. Early in the design phase, metal pumps made from steels were tested, uncoated, and with polymer based seals. Although a few flexible polymers are stable at slightly above the melting point of Sn these seals have very short life and are very sensitive to slight increase above the melting temperature of Sn [73].

Aware that thermodynamic data showed Sn would react with these materials, there was interest in determining the life of these components at this moderate temperature. For

example, a 316 stainless steel external gear pump was procured from the Lobe Pump and Machinery Company, version LOE. During testing, the gears corroded very quickly and failed to function after only a few hours. Figure 3 shows two originally identical gears from this test, with the uncoated gear nearly completely corroded.



**Figure 3:** Relative corrosion of stainless-steel gears after less than 24 hours of contact with Sn at  $\sim 300^{\circ}\text{C}$ . the gear on the left was coated with CrN

Following these initial tests, a pump was made from Inconel 625 (a nickel-based alloy from Special Metals) and coated with CrN. Inconel 625 was selected for two key reasons, the first being that it was one of only a few candidates that were compatible with the necessary CrN coating. Haynes 230 (another nickel-based alloy) and 304 stainless-steel were also candidates, however, Haynes 230 was prohibitively expensive and the 304SS option was not selected because of its lower strength at elevated temperature. Therefore, based on the compatibility with a CrN coating, and to enable retention of mechanical strength at temperatures up to  $600^{\circ}\text{C}$ , the primary medium temperature pump was made from Inconel 625. This pump performed very well, and details of its testing are included in

Chapter 5. Although this pump was limited to 600°C, it was the least expensive, and reliable molten Sn pump developed during this experimental campaign and was the only one which was ductile at room temperature. It is important to emphasize that this pump depended on a thin (3µm) CrN coating which prevented corrosion of the base material. This coating was applied using a physical vapor deposition (PVD) process known as sputtering, where the base metal was mounted inside a vacuum chamber and sputtered with CrN at ~400°C [74]. The CrN is vaporized and ejected from a solid toward the base metal by bombarding it with high energy ions. Because dynamic components are subject to wear, this coating has a limited life—although it has not failed from wear after approximately 80 hours of operation. An image of the fabricated pump is shown in Figure 4.

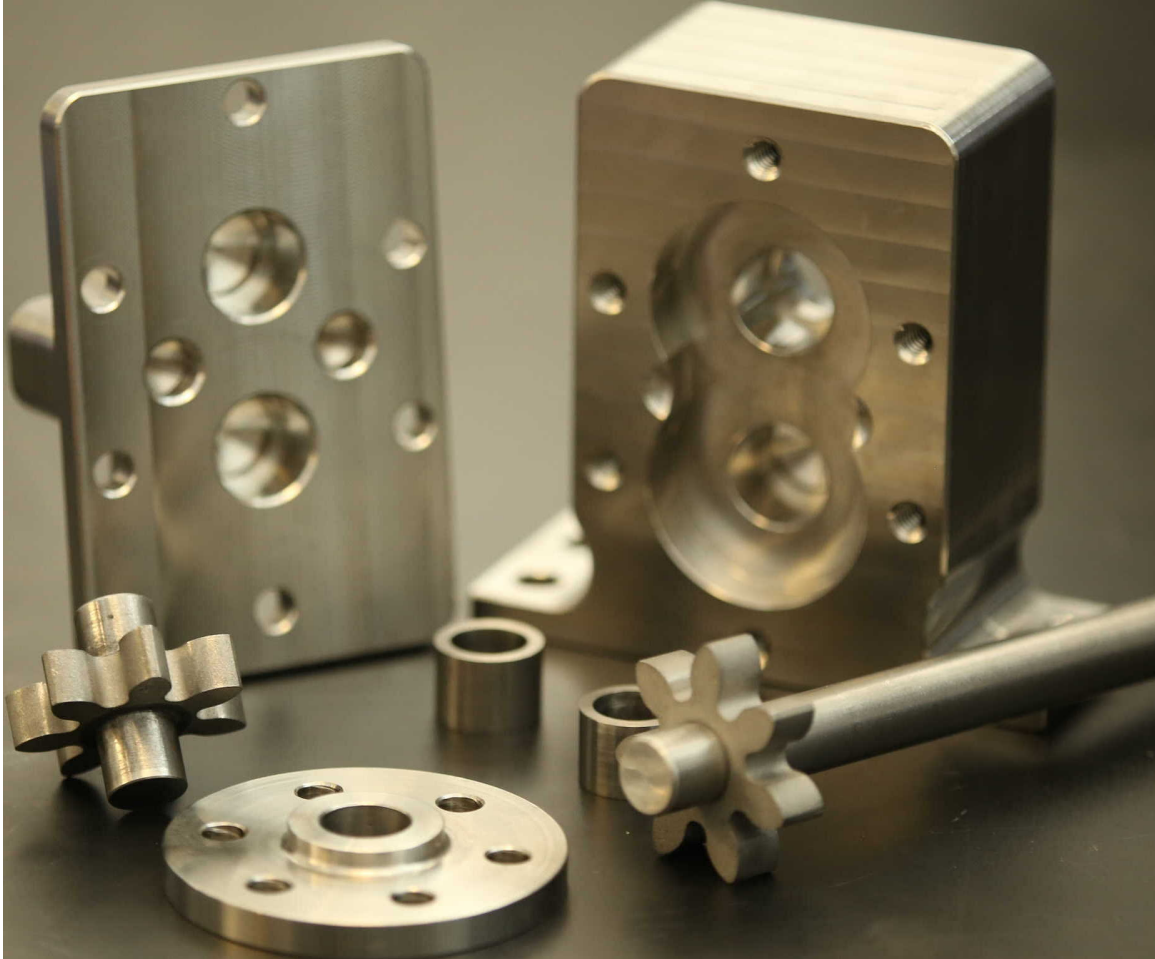


**Figure 4:** Inconel 625 external gear pump. Notably, the base of this pump differs from the high temperature pumps, because this pump was mounted directly to its baseplate.

This pump employs Graphalloy (a commercial copper impregnated graphite) sleeve bearings to support the gear shafts. For thermal expansion matching, it is ideal to use the same materials for pump components. However, the need to prevent galling (the onset of friction welding) and/or wear of the protective coating necessitated the use of a softer, self-lubricating sleeve bearing. Moreover, in this medium temperature range, thermal expansion was less critical of an issue since the temperature difference was much smaller; in this case, the result was a slight increase in bearing clearance, so no binding or noticeable efficiency loss was experienced.

### 3.2.2 *Shapal Hi-M Soft™*

While many ceramics are compatible with Sn, as discussed in Chapter 2, the primary material investigated in this work was Shapal, a machinable AlN/BN composite. Candidates for future work are included in Chapter 5. Shapal contains 20 at.% BN, which gives it the important property of machinability, where small ( $\sim 5 \mu\text{m}$ ) particles of AlN are abraded during machining. This property enables Shapal to be precisely machined into complex geometries in its fully fired state, with standard carbide tools. Here, the relatively soft BN particles stop crack propagation so that relatively smooth surface finishes ( $\sim 0.4 \mu\text{m}$  RMS roughness) can be achieved using cutting tools, rather than grinding or polishing. Further, Shapal's thermal expansion is very well matched with graphite, with a CTE of  $4.9 \times 10^{-6} \text{ K}^{-1}$  compared to  $5.0 \times 10^{-6} \text{ K}^{-1}$  of graphite. Notably, both of these materials exhibit a nearly linear increase in CTE with temperature in the range of interest. An image of the fabricated pump is shown in Figure 5.

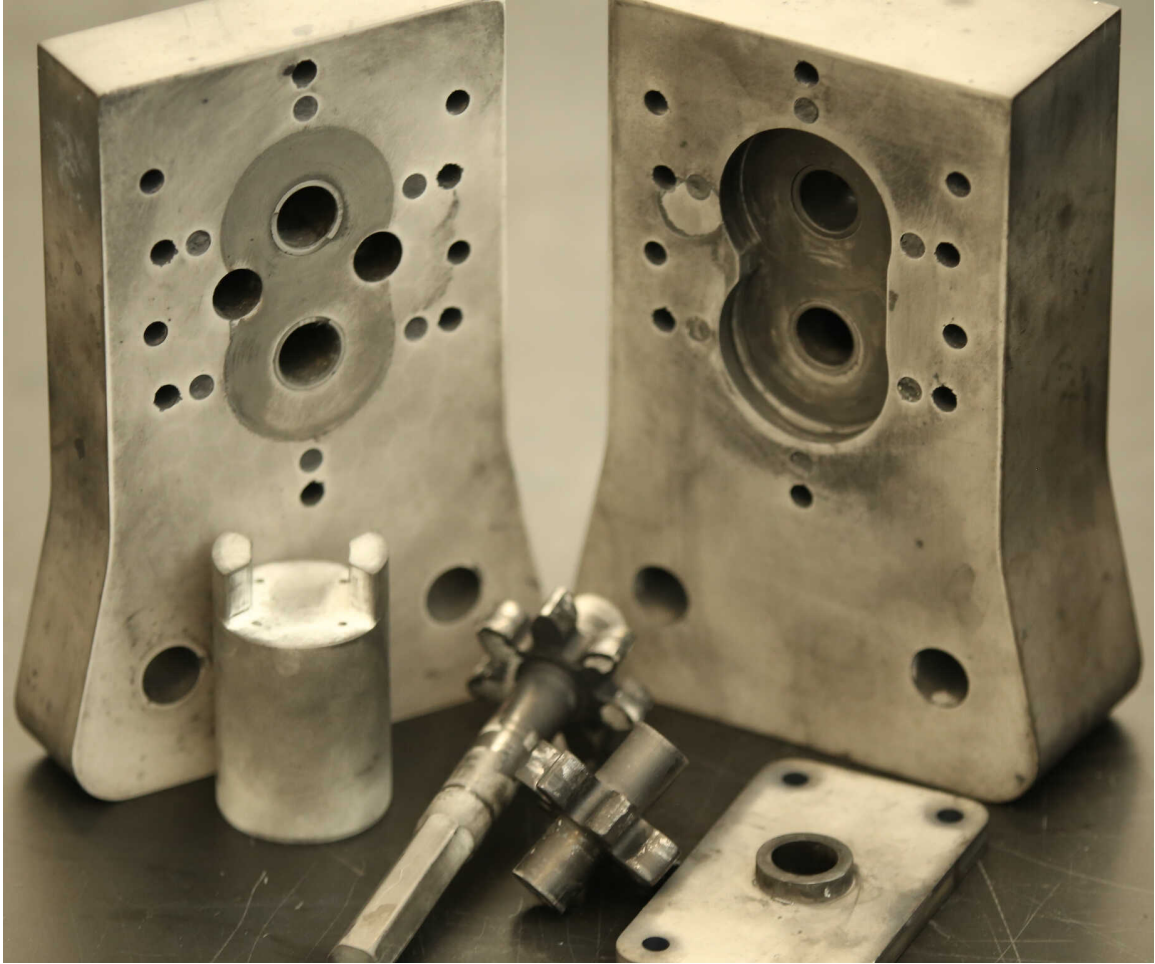


**Figure 5:** Shapal Hi-M Soft™ external gear pump

Shapal also has attractive mechanical and thermal properties including a competitive fracture toughness ( $3.77 \text{ MPa m}^{0.5}$ ), flexural strength of 300 MPa, and high thermal conductivity ( $35 \text{ W m}^{-1}\text{K}^{-1}$  at  $1000^\circ\text{C}$ )—all desired properties in a component experiencing extreme temperature, and large temperature gradients. Also, as noted in the Introduction, as a nitride ceramic, Shapal is compatible with several molten metals heat transfer fluids including Sn, Pb, Bi, Ga, and In. Therefore, although it was only tested with Sn, the results imply the broader capability to pump other liquid metals—at least without changing the primary pump material.

In this pump, unlike the medium temperature pump, the same material was used for all flow path components, including sleeve bearings. Thermal expansion was especially critical for this pump design because it reached the peak system temperature, so matching the bearing, shaft, and pump body expansion was critical. Notably, dynamic components typically avoid having sliding surfaces of the same material in contact, to prevent galling—a type of severe wear caused by adhesion between sliding surfaces. Here, if the two materials are similar, or identical, galling can be caused by the slipping of the crystal structure beneath the surface, and is the onset of friction welding. While galling was not an issue with this ceramic pump, significant wear issues were encountered with the bearings and gear teeth, partially because a softer material was not used for the bearing. Unfortunately, the same property that makes Shapal machinable, also makes it a poor material for wear applications. Here, graphite could have been used for the sleeve bearings, but this was not tested. This topic is discussed extensively in Chapter 5.

### 3.2.3 *Tungsten*

As noted in Chapter 2, Sn does not react with W, even at temperatures well above the current application. Tungsten has attractive material properties for a high-temperature pump because it is ductile at the application temperature, but also very strong. The yield strength of tungsten at 1350°C is ~410 MPa, which is similar to that of low carbon steel at room temperature [75]. Tungsten transitions to ductile between 70°C and 320°C depending on its structure—typically as a result of cold working [76]. Because the W used in these experiments was machined from hot pressed base material, it was not cold worked, and had a ductile-brittle transition temperature (DBTT) of ~300°C; thus, it was not prone to brittle fracture at the application temperature. Therefore, although limited in the HTFs it

can pump, a tungsten pump was also fabricated, which enabled the highest potential temperature application of the materials considered, above 2000°C. An image of the fabricated pump is shown in Figure 6.



**Figure 6:** Tungsten external gear pump

In this pump, graphite bearings were used to prevent galling and because the tough material could tolerate more misalignment (relative to Shapal) resulting from improperly toleranced bearings. These bearings were made custom made from AR-14 Molded EDM graphite rather than the Graphalloy used for the medium temperature Inconel 625 pump

because copper is liquid at this extreme application temperature and therefore would not provide the beneficial friction and wear reduction.

As C was used in contact with W in this pump, it should be noted that these elements are not inert with respect to each other, and indeed form tungsten carbide (WC)—the kinetics of which are accelerated in this high-temperature environment. However, the WC scale that develops inhibits further diffusion of C across the scale. The scale thickness begins to plateau after a thin layer forms, due to diffusion limited transport (thickness proportional to  $\sqrt{t}$ , where  $t$  is time) and therefore this caused no measurable problems in experimentation. In fact, a separately applied WC coating was used as a protective oxidation barrier on the exterior of the tungsten components [77].

### **3.3 Pump Sealing**

The most significant issue with attempting to make a mechanical pump for extreme temperatures is dynamic sealing. Most pumps employ polymer based seals both to dynamically seal the shaft and to seal the two parts of the pump gear cavity. However, even for the medium temperature pump, polymer based seals were not suitable. Although a few flexible polymers are stable slightly above the melting point of Sn, the most notable of which are silicone, fluoroelastomer (FKM), or Polytetrafluoroethylene (PTFE) based seals. However, these seals have very short life and are very sensitive to slight increase above the melting temperature of Sn [73]. Above their design temperature, these seals begin to decompose and lose their ductility—resulting in leaks. Therefore, even for the lowest temperature pump, polymers were not compatible and a new sealing design was used for all three pumps.

Mechanical face seals are a potential solution, although they require the added complexity of multiple components and extreme precision. This approach also typically depends on a constant leak rate to lubricate the seal, which could lead to containment and freezing issues. Here, two hard ceramics could be used, but because of the extremely low vapor pressure of Sn, the necessary lubrication would result in liquid Sn leaking and eventually freezing on the pump components. Another challenge with extreme temperature mechanical face seals is that they frequently rely on a spring to apply pressure to the seal surface, but an appropriate material that could perform well at 1350°C for this application was not identified. A tungsten-based material is likely ideal, although fabrication may be difficult because of its brittle nature at low temperatures. This brittle behavior may also cause it to fail during assembly.

Instead, the property of graphite that made it unfavorable as the pump construction material, namely its low strength, was leveraged. More specifically, what is similar between graphite and polymers is the mixture of bonding within the material. Polymers contain very stiff intramolecular interactions that make them corrosion resistant, but the weak van der Waals interactions between molecules allow the individual polymer chains to easily slide/deform and accommodate sealing surfaces. Similarly, graphite consists of stiff intramolecular bonds in each graphene layer, with much weaker van der Waals bonds in between layers that allow comparable deformation. Here, individual graphene layers can easily slide parallel to another layer. Conceptually, other refractories, such as BN, with a similar crystal structure or bond heterogeneity could also serve as a sealing material, or in some applications, seal-less sump pumps could be used [78, 79].

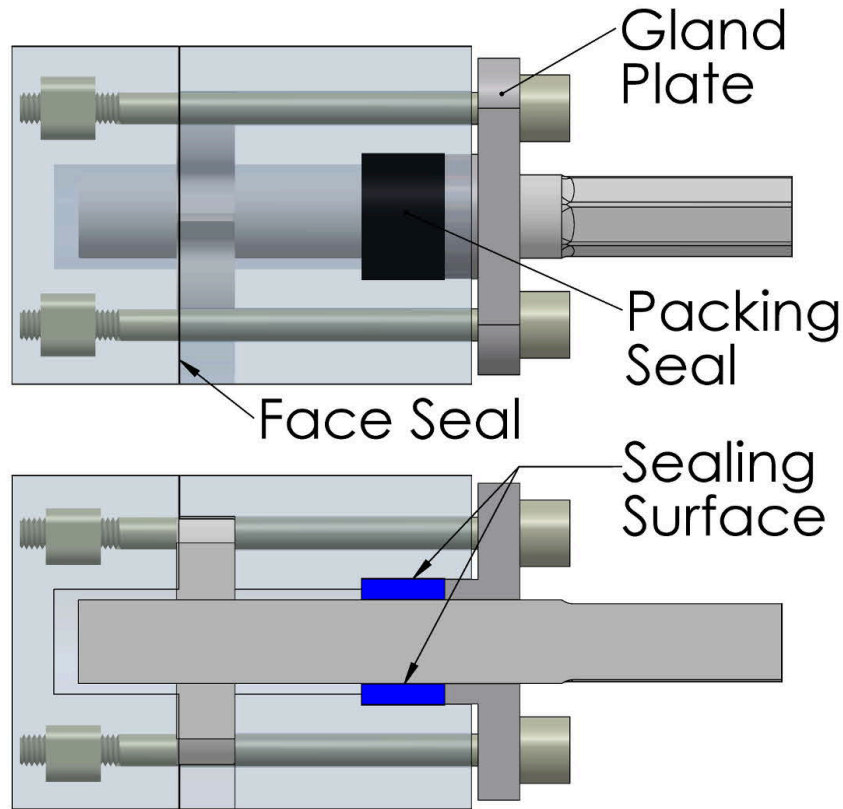


**Figure 7:** Model of graphite packing shaft seal. This seal expands radially (here, vertically) when compressed axially (here, horizontally) by the symmetric gland plate. Also shown is the graphite sheet based face seal.

Based on these design principles, the seal along the gear shaft that prevents the Sn from escaping the high-pressure region inside the pump to the lower pressure outside gas environment was made of graphite packing material (Palmetto 5000). Sealing was achieved through radial expansion when the seal was compressed axially, see Figure 7. Although this seal was designed to slowly wear over time, it can be periodically tightened, or even automatically tightened, by employing Belleville (conical) washers for *in situ* actuation.

### 3.4 Pump Mounting

The pump was bolted to a refractory brick base which, in series with a steel cold plate, was bolted to the steel baseplate. The base was made from SILRATH AK-60, an andalusite based brick which is stable to 1400°C, and balances low thermal conductivity ( $\sim 2 \text{ W m}^{-1}\text{K}^{-1}$ ) with high compressive strength (70 MPa). The rigid mounting to the baseplate ensures the pump and motor do not rotate with respect to each other, so the only rotation was of the gears. The cold plate maintains the baseplate below 40°C, ensuring that it remained rigid and that it did not contribute to the thermal misalignment discussed in the next section. Figure 8 depicts the components used to mount the pump, as well as the shaft design, which is discussed in the next section.

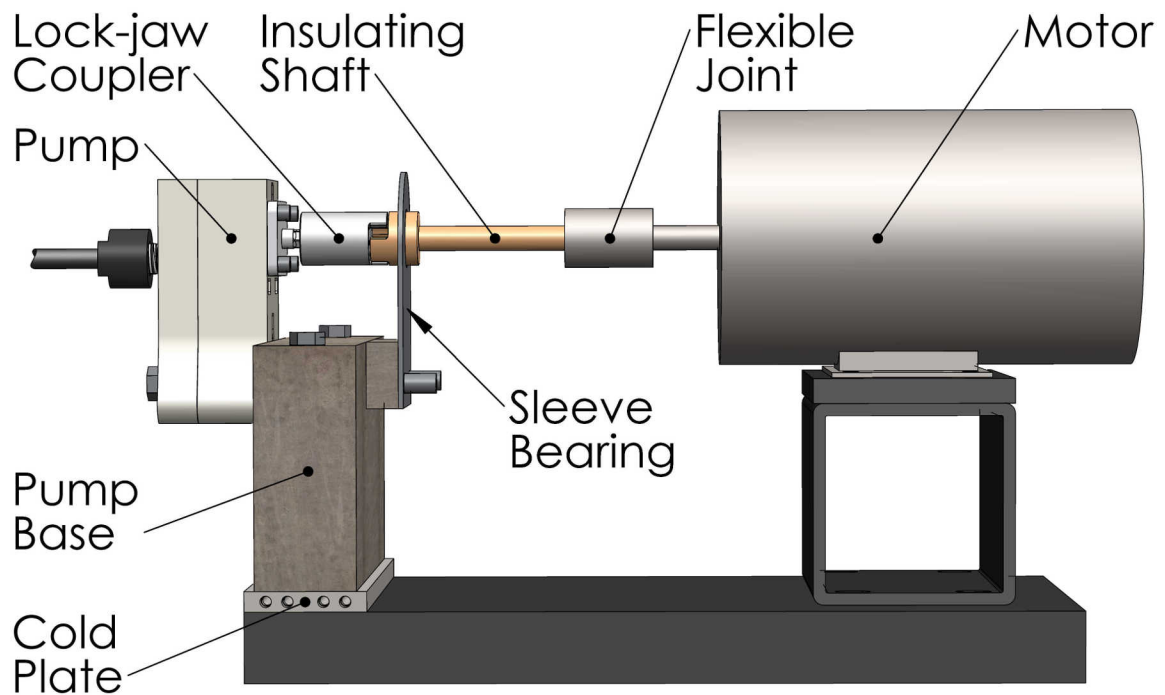


**Figure 8:** Model of the pump with mount, shafts, and motor

During the design process, bolting was a major concern. Initially, Shapal bolts were fabricated for clamping the pump cover to the pump body, but the small threads on the 5 mm diameter bolts introduced such high-stress concentrations, that they failed even below

0.1 Nm of torque. Several of the fractured bolts are shown in Figure 9. Another issue arose in using TZM (a Molybdenum alloy) bolts. Here, TZM bolts were used to mount the Shapal pump to the andalusite base, but the CTE of TZM ( $6.1 \times 10^{-6} \text{ K}^{-1}$ ) is larger than that of Shapal ( $4.9 \times 10^{-6} \text{ K}^{-1}$ ) so the bolts became loose at high temperature, resulting in a gap of  $\sim 0.2 \text{ mm}$  which caused a major leak at the pump cover face seal (see Figure 50). Also of concern was the possibility of the nuts self-loosening, which could be resolved by various methods of locking the nuts angular position relative to the bolt, but in practice, self-loosening did not occur.



**Figure 9:** Ceramic (Shapal) bolts which failed from brittle fracture during installation

Based on these considerations, W was employed for most high-temperature bolts, because of its high tensile strength, ductility at the application temperature, and low CTE ( $\sim 4.5 \times 10^{-6} \text{ K}^{-1}$ ). Because these bolts are brittle at room temperature, heating to  $\sim 300^\circ\text{C}$  prior to installation increases ductility, thereby reducing the risk of brittle fracture upon installation [76, 80]. Also, the thermal expansion of the bolt enabled an additional preload without added torsional stress. TZM bolts could be used in regions where the temperature remained below  $1200^\circ\text{C}$  and the material being clamped had a sufficiently high CTE. In such situations TZM is preferable over W because it exhibits similar properties to tungsten,

but at a lower cost, although their strength drops sharply above 1200°C. To determine where the system temperature permitted the use of TZM bolts, a thermal model was developed, which is described in the following sub-section.

### *3.4.1 Thermal modelling using COMSOL Multiphysics*

Several thermal models were numerically solved using COMSOL Multiphysics to determine temperature profiles, heat loss, and thermal expansion. In each of these models, Equation 1, the heat equation, was solved. Heat flux,  $q''$ , was non-zero for models that included inductive heating, as described in Chapter 4. Here, the inductive heating was approximated as uniform heat generation, as the special profile was unknown and it was beyond the scope of this work to model it. In most cases, studies were steady, so  $\partial T/\partial t$  was equal to zero. However, in the case of optimizing induction heat input, a transient study was conducted, as described later in this chapter. Interfaces between solids were treated as in thermal contact without contact resistance. Where available, temperature dependent thermal conductivity was used to solve Equation 1—this was especially important for insulation, through which the largest temperature differences occurred. Further details of the inputs to the thermal models, including thermal conductivity of materials used, are provided in Appendix B.

Radiative heat transfer was solved using the Stefan-Boltzmann law, shown in Equation 2. Similarly, convection heat transfer was solved by prescribing a convection coefficient and solving Equation 3, Newton's law of cooling. These equations were solved using the finite element method, and were checked for mesh convergence, as shown in Appendix B.

$$\frac{\partial}{\partial x} \left( k \frac{\partial T}{\partial x} \right) + \frac{\partial}{\partial y} \left( k \frac{\partial T}{\partial y} \right) + \frac{\partial}{\partial z} \left( k \frac{\partial T}{\partial z} \right) + q'' = \rho c \frac{\partial T}{\partial t} \quad (1)$$

$$q''_{rad} = \sigma \varepsilon (T_1^4 - T_2^4) \quad (2)$$

$$q''_{conv} = h(T_1 - T_2) \quad (3)$$

The model of the pump system used to determine the temperature profile in the pump mount included the insulation to be used (although hidden here), and is shown in Figure 10. This model was also used to determine the required length of the insulating ZrO<sub>2</sub> shaft, and whether it required active cooling, as discussed in the next section. The boundary conditions used in this model included: the ambient air temperature of 30°C, a prescribed natural (although enhanced by fan coolers) convection coefficient of 5 W m<sup>-1</sup>K<sup>-1</sup>, a prescribed fluid temperature of the pump flow path (1350°C), and radiative losses from the insulating shaft and the exterior of the insulation, based on Equation 2. Here, the environment temperature,  $T_2$ , was prescribed as 30°C. This model showed that the edges of the brick base would remain cool enough to use TZM bolts, and the zirconia shaft would cool sufficiently if left exposed to ambient air, so that active cooling was not needed.

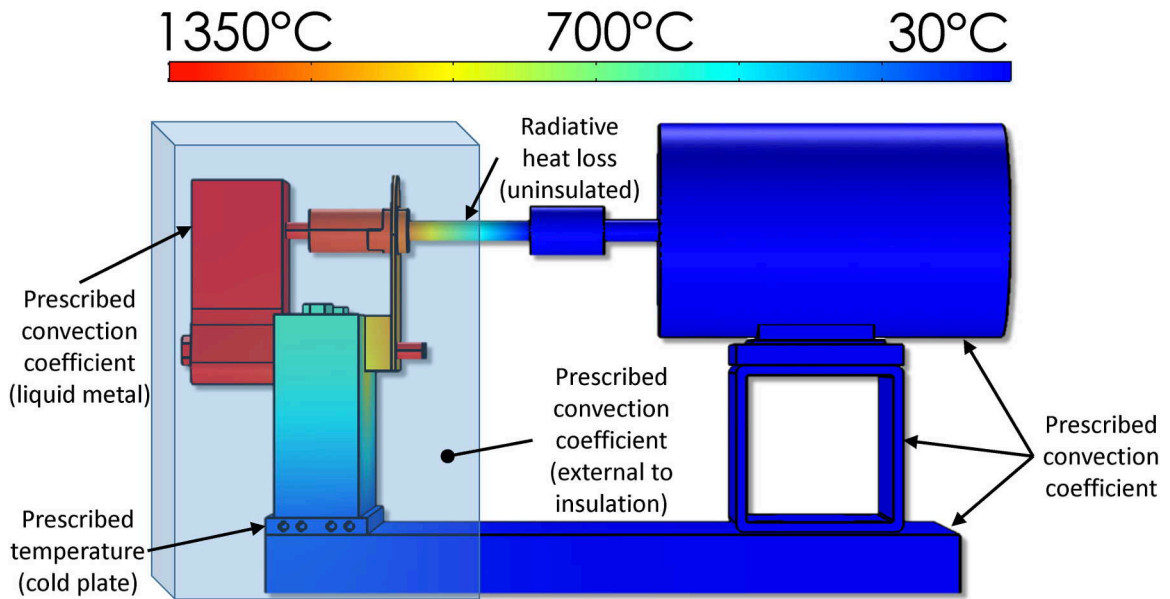


**Figure 10:** Thermal model of the pump system

The method used to mount the pump exhibits the general design principle of leveraging the compressive strength of ceramics while avoiding tensile stress. Therefore, the chemical compatibility of ceramics was leveraged in direct contact with the fluid, but threaded metal bolts and nuts were used wherever tensile forces were needed. Although tungsten is compatible with direct contact with tin, this principle enables other refractory metals that are not compatible with Sn( $\ell$ ) such as Molybdenum to be used in these locations since there is no direct contact with the fluid being pumped. Similarly, if other fluids were pumped, this would be the only way to enable the use of tungsten.

### 3.5 Pump Actuation

In order to drive the pump, it had to be connected to a motor. Typically, this is a simple task: the pump shaft is coupled directly, and often rigidly, to the motor shaft, and the two shafts are aligned. In this case, however, because the pump operates at an extreme

temperature and the motor must remain cold, the two devices had to be thermally separated, thus significant misalignment was caused by vertical thermal expansion between the pump and motor. A basic calculation shown in Equation 4, suggested that a vertical misalignment of 1.37 mm would occur at 1350 °C, taking  $\alpha = 4.7 \times 10^{-6} \text{ K}^{-1}$ ,  $L = 220 \text{ mm}$ ,  $T_{hot} = 1350^\circ\text{C}$ , and  $T_{cold} = 20^\circ\text{C}$ . This thermal expansion was appropriate because the Shapal pump and andalusite base have similar thermal expansion coefficients ( $4.9 \times 10^{-6} \text{ K}^{-1}$  and  $4.5 \times 10^{-6} \text{ K}^{-1}$ ). This predicted misalignment was also computed by calculating the displacement of each element in the model via Equation 4, using the solution for the steady state temperature distribution in COMSOL. The resulting thermal expansion is shown in Figure 11. The temperature profile input to this model was the solution from the model shown in Figure 10 and described in the previous section on Thermal modelling using COMSOL Multiphysics.

$$\Delta L = \alpha L (T_{hot} - T_{cold}) \quad (4)$$

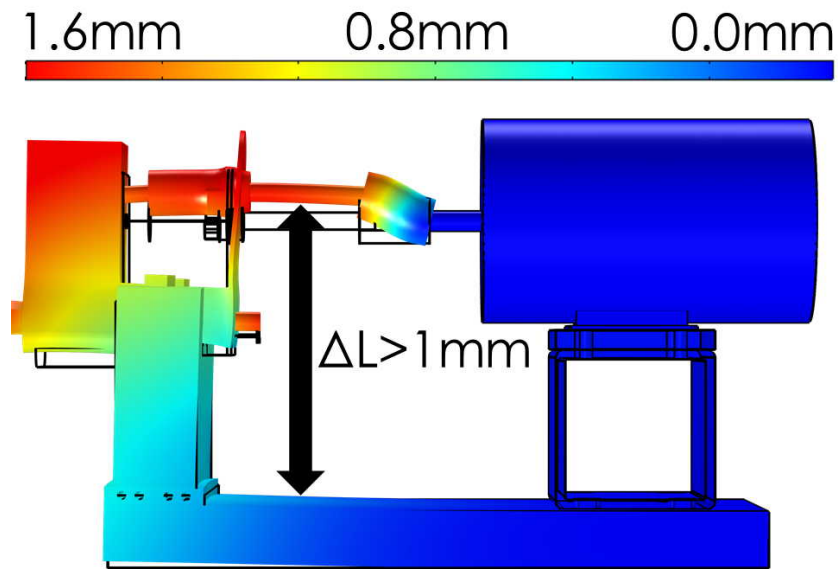


**Figure 11:** Thermal expansion of pump system at 1350°C

To experimentally verify this model, an *in-situ* alignment monitoring system was designed and tested to monitor the shaft angle. This system employed a stylus indicator, designed to mimic commercially available shaft alignment tools. This type of tool enables the user to check angular alignment by measuring the distance between the styli at various angular positions, as shown in Figure 12. For aligned shafts, this measurement will be constant as the shaft is rotated (independent of angle). An added motivation for developing this tool was to use it as an input in a closed loop alignment control system. Here, the motor could be mounted to a digitally controlled stage which could be used to zero out misalignment.

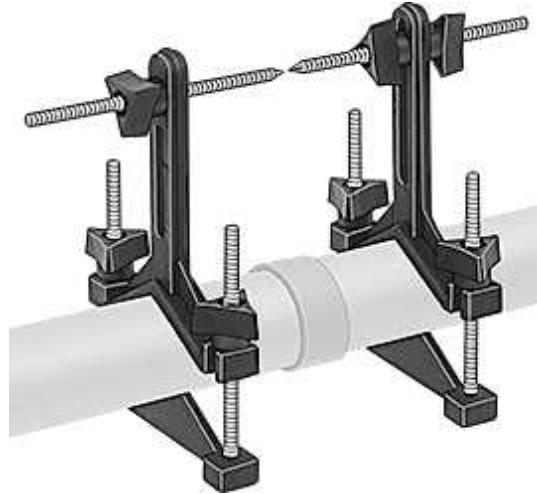


**Figure 12:** Schematic of stylus based, visual shaft alignment tool

Unlike commercially available stylus tools, this custom tool was compact, mechanically strong, and made entirely of stainless steel so that it could remain installed during operation, where it was subjected to a temperature of  $\sim 200^{\circ}\text{C}$  and mechanical stress caused by centrifugal acceleration. It also included two sets of styli, which was necessary to balance center of mass of the system but also enabled comparison of two opposite angular positions at once, which was convenient for processing. In this way, the alignment indicator could continuously monitor the alignment. The indicator is shown in Figure 13, with the commercial indicator installed external to it for reference.

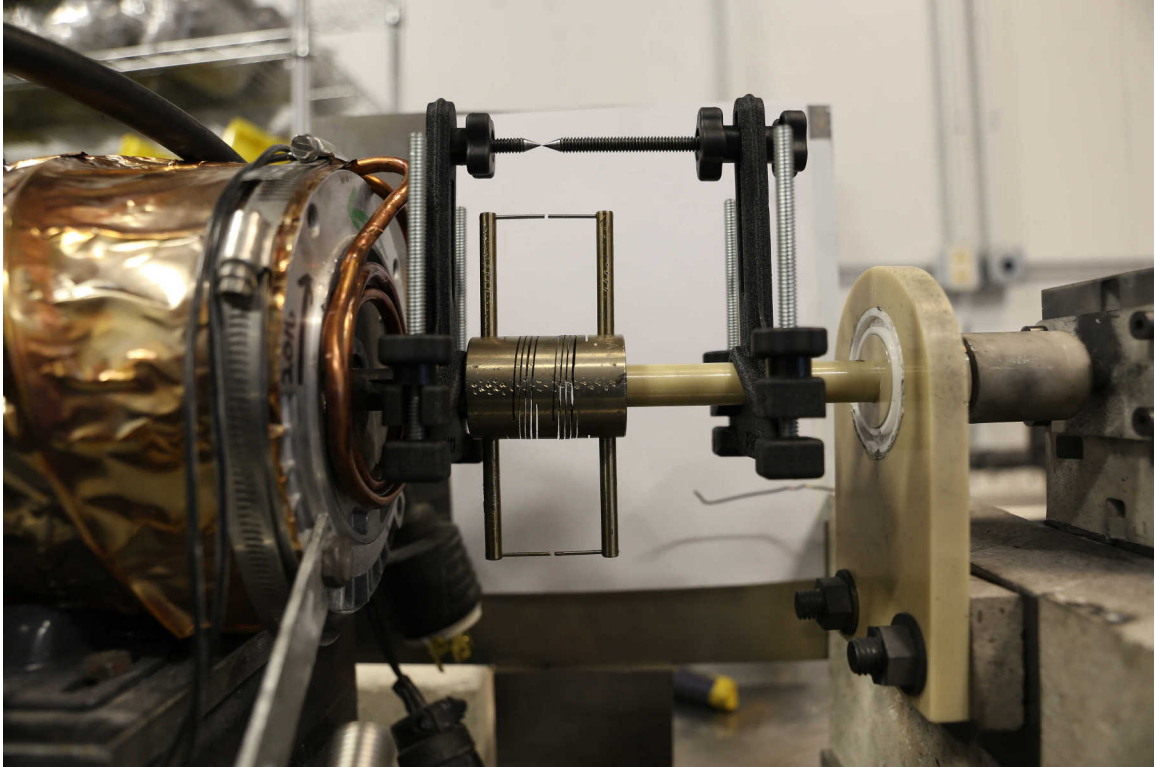


**Figure 13:** Commercial and custom *in-situ* stylus indicator tools

While the stylus gap is conventionally measured with a feeler gauge (a tool with several precision thickness metal plates), which enables high precision measurement, for this *in-situ* system the gap needed to be measured without physical access, so it was measured via a camera and image processing. A Canon 6D DSLR camera, with an 180mm macro lens, was used to capture these images. However, even with this nearly ideal equipment, because of the inert environment present, the camera was separated from the styli by a window, which limited how closely the image could be taken. Therefore, in practice, although the trends matched simulated data, the resolution of the stylus gap was insufficient to reliably predict the amount of shaft misalignment.

This issue was further complicated by the fact that the shafts elongated as temperature increased—because of thermal expansion. Figure 14 shows the styli tips both

as captured and after converting to a binary bitmap image; as shown, the resolution limited the accuracy to about  $\pm 10\%$  of the absolute gap, which only changed by  $\sim 20\%$  from ambient to peak temperature, so the system could essentially only indicate the direction, rather than the amount, of misalignment. This resolution could have been improved with different optical equipment, although with the short focal distance required and the constantly moving subject this would provide limited improvement. Alternatively, the styli could be made longer radially, but this would increase the risk and consequence of mechanical failure, where a steel rod could be ejected from the tool at high speed.

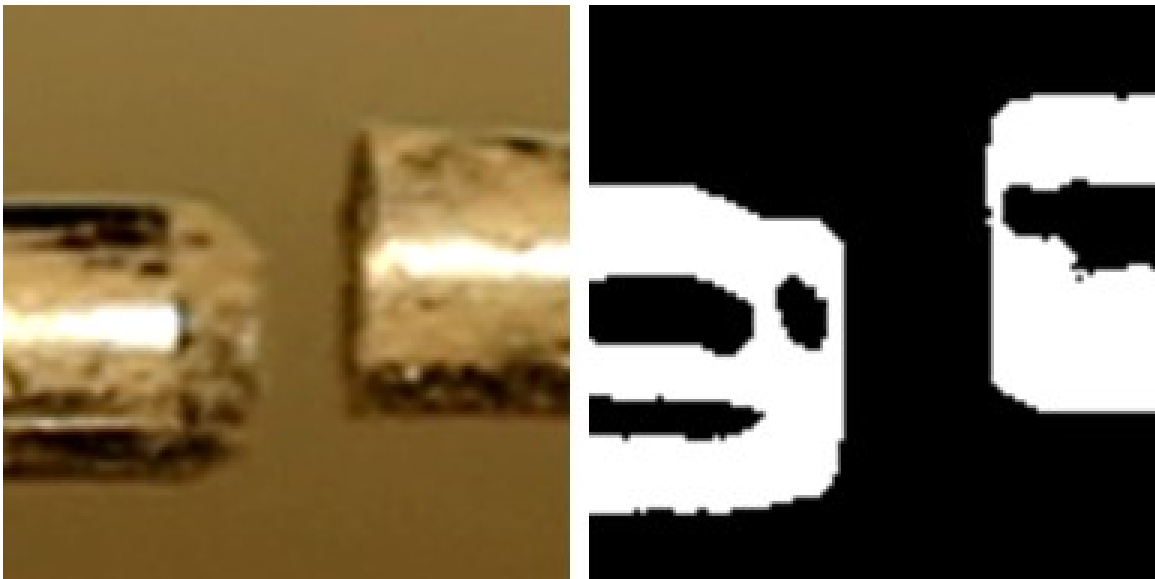


**Figure 14:** Image showing the resolution limitations of custom styli gap measurement

### 3.5.1 *Potential Alignment Solutions*

Once the alignment issue was confirmed and quantified, several potential solutions were considered. Notably, there are many industrial and commercial applications where the ends of a linkage system move with respect to each other, *e.g.*, the front axles of most cars. These systems often employ universal joints, supported by metal ball bearings and

lubricated by grease. The materials used in such joints, however, include polymers and iron-based metal alloys. A representative universal joint is shown below in Figure 15.



**Figure 15:** Typical single universal joint for nonparallel shafts

Above 1000°C, however, the options were very limited and a simple design was preferred. For example, while tungsten could be used for some components, to achieve the required temperature drop (with minimal heat loss) across the shaft system, a portion of it should have low thermal conductivity. For this reason, the longest shaft component used was stabilized  $ZrO_2$ , which has a thermal conductivity below  $2 \text{ W m}^{-1}\text{K}^{-1}$ . A thermal model of the pump system, developed in COMSOL, was used to determine the necessary length of this shaft to achieve sufficiently low temperature ( $\sim 200^\circ\text{C}$ ) at the metal coupler and motor shaft and to determine if active cooling would be required. The conditions employed in this model are described in the section on Pump Mounting and shown in Figure 10.

It was important to use fully stabilized  $ZrO_2$  for this extreme temperature application because pure unalloyed  $ZrO_2$  exists in the monoclinic phase at ambient temperature, but transforms to tetragonal at  $1173^\circ\text{C}$  which would result in a volume change and, therefore mechanical failure of the component. This phenomenon is discussed in detail

in Chapter 2. Similarly, although ceramic ball bearings are commercially available (in limited sizes and materials), few are designed for extreme temperature use. For example, commercially available  $ZrO_2$  ball bearings are not fully stabilized, which limits their use to dry environments below  $\sim 1000^\circ C$ . This limitation was realized experimentally, as this type of bearing was initially used and it experienced brittle fracture during multiple experiments, as shown in Figure 16. This failure was partially caused by misalignment, although the lack of a fully stabilized bearing exacerbated the issue.



**Figure 16:** Zirconia ( $ZrO_2$ ) ball bearing failure

Based on these constraints, the actuation system was designed using ductile metals wherever possible and fully stabilized  $ZrO_2$  wherever necessary. As mentioned earlier, the motor shaft was extended with a 10 cm long, 1.5 cm diameter insulating  $ZrO_2$  shaft. This shaft bridged most of the  $1200^\circ C$  temperature difference between the pump and the motor and was attached to the motor shaft via a flexible, stainless steel, helical coupler. The hot end of this shaft was supported by a tungsten sleeve bearing, which was custom made for this application—shown in Figure 17. The inner surface of this bearing was fully filleted,

to prevent over constraining the shaft, which deflected by  $\sim 1^\circ$ . To minimize misalignment during operation, the shafts were aligned to target the average operating temperature of  $1000^\circ\text{C}$ , based on the simulated thermal growth of 1.03 mm at  $1000^\circ\text{C}$  as shown in Figure 11. In this way, the maximum misalignment between  $650^\circ\text{C}$  and  $1350^\circ\text{C}$  was less than 0.4 mm instead of 1.37mm.

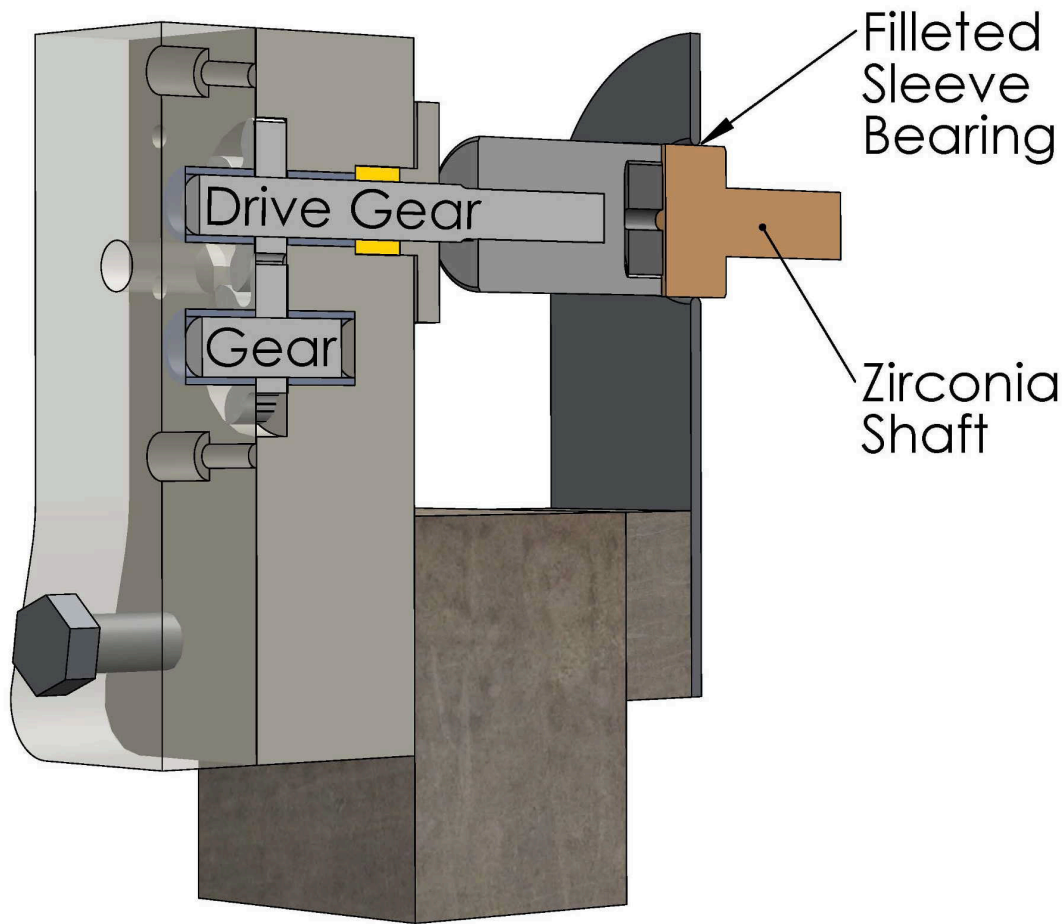


**Figure 17:** Filletted tungsten sleeve bearing to support zirconia shaft extension

The  $\text{ZrO}_2$  shaft interfaced with the Shapal Hi-M Soft™ pump shaft via a custom jaw coupling (see Figure 17), which accommodated thermal growth mismatch radially, and a small amount of axial and angular misalignment. While this type of coupling typically

employs an elastomer “spider” to dampen the interface, because of the extreme temperature present, this component was fabricated from TZM (a molybdenum based alloy)—which does not serve the original damping purpose but is nonetheless required as a mechanical linkage.

Fully assembled, the Shapal pump was driven by a motor situated 30 cm away, which was outside the insulated region, where it remained cool via natural convection. An active cooling jacket made of copper was also added as a safety precaution and this setup is shown in Figure 18 and modeled with annotations in Figure 8. Because two of the shafts used in this system are ceramic ( $ZrO_2$  and Shapal) there was significant fear of brittle fracture from misalignment or vibration. The former was realized and is discussed in Chapter 5.

Thus, three pumps were designed: from Shapal, W, and Inconel 625. Further, a system was designed to seal, mount, and actuate the pump, accounting for thermal expansion. This system thermally isolated the pump, while maintaining a strong mechanical connection to the motor. The next step was to develop an experimental setup so the key question of this study could be addressed. That is, can a pump be designed from ceramics to circulate liquid metal that survives this extreme environment with long life, and without breaking or leaking?

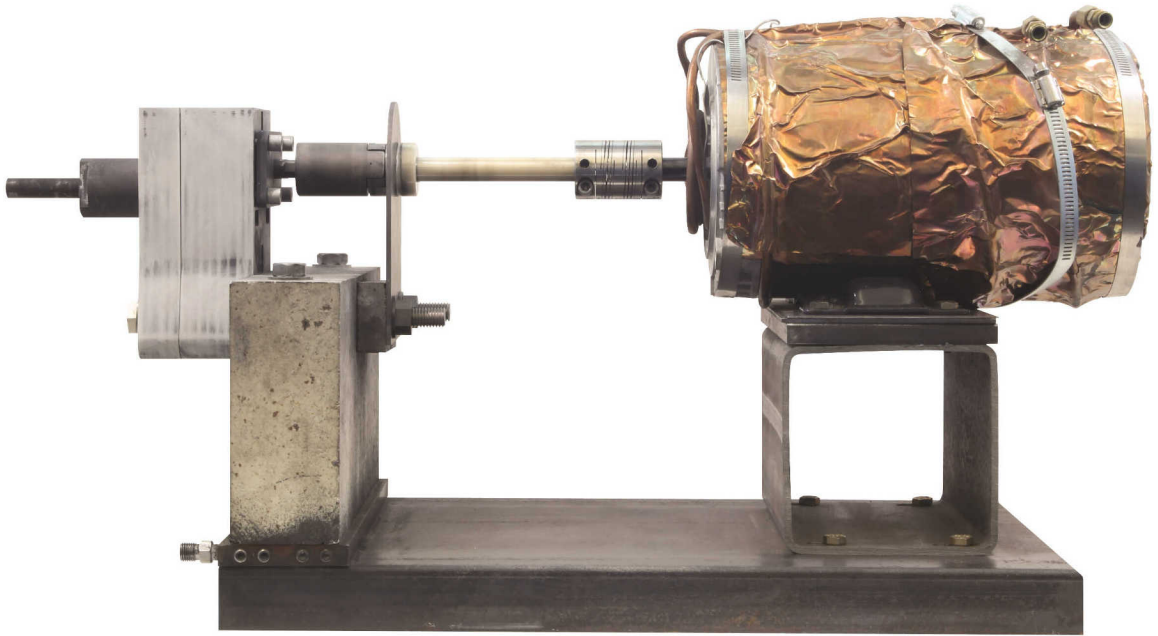


**Figure 18:** Image of pump system

## **CHAPTER 4. EXPERIMENTAL SETUP**

Following the design and fabrication of the pump, a system was developed to test its capabilities. This system included the components for a molten Sn circulation loop as well as supporting components including a flow meter, heating, cooling, insulation, and measurement components, and an inert gas chamber. The circulation loop was geometrically simple, consisting of a reservoir (10 cm high x 10 cm diameter) with a 1 cm inner diameter pipe connected to the base so that it drained into and primed the pump by gravity. The Sn was then pumped out of the pump uphill to the outlet above the reservoir, where it fell back into the reservoir completing the circulation loop. In several initial experiments, as shown in Figure 19, a flow meter was not used and the liquid metal stream exiting directly from the outlet pipe could be observed via a viewport in the insulation and a window installed on the inert containment vessel. However, later experiments employed a flow meter to quantify and actively control the flow rate, as will be described later in this chapter.

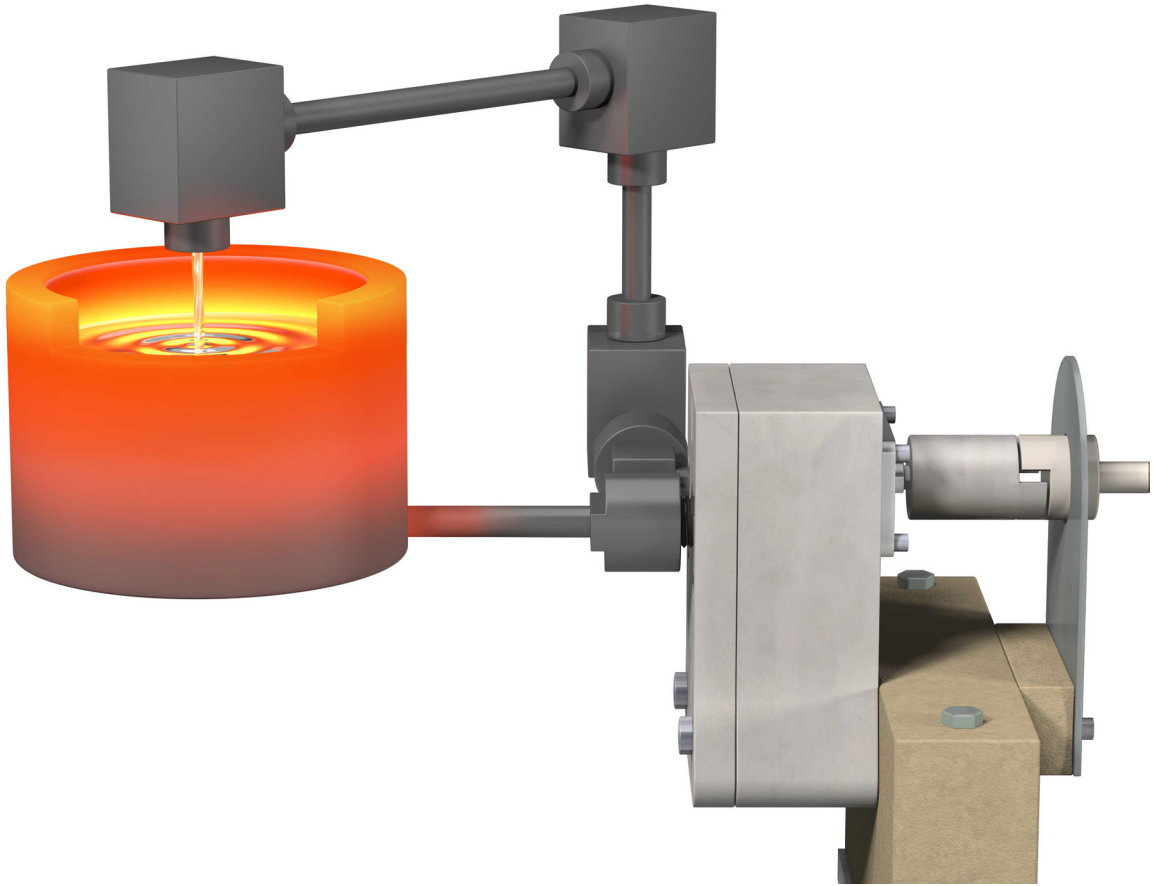


**Figure 19:** Model of pump with circulation loop. Reservoir shown illuminated for comparison to images from experiments, like Figure 57.

#### 4.1 Circulation Loop

The circulation loop included a reservoir, pipes, elbows, unions, seals, and in the final tests, a flow meter. During early experiments, which were conducted near the melting temperature of Sn, iron based alloys were used for many of these components. Here the metal pipes, unions, and reservoirs were coated with a protective ceramic barrier coating—usually CrN, as described in the chapter on Material Selection. For long pipes, commercially available glass lined metal pipes were originally used. These frequently suffered cracking from mechanical and thermal stress. Alumina ( $\text{Al}_2\text{O}_3$ ) pipes were also used in some experiments, but their low strength and difficulty in machining made them

more difficult to work with. Instead, graphite was eventually selected as the preferred containment material.

Therefore, for high-temperature tests, C was employed for all components in contact with liquid, except for the pump, as noted in the previous chapter. Although other materials are thermodynamically compatible, graphite was used because of several favorable characteristics. Notably, C is inexpensive compared to other compatible ceramics, especially when the manufacturing/fabrication cost is considered. This is because C is easily machinable in its final (fully fired) state, and can, therefore, be machined with standard carbide tools without the added step of grinding, which is required for most ceramics. Graphite also remains solid, and inert with respect to Sn and the nitrogen gas environment, to temperatures above 3000°C. Similarly, graphite is not wet by tin, which makes the components less prone to leaks—although this was a major challenge. C also has high thermal conductivity ( $\sim 60 \text{ W m}^{-1}\text{K}^{-1}$  at 1350°C), which minimizes thermal stress and it is electrically conductive, which enables inductive heating, as will be discussed in the Thermal Management Equipment section later in this chapter.

Commercially available graphite was used for all the circulation loop components including the reservoir, flow meter, piping, and joints. The reservoir, and other bulk components, were purchased from [graphitestore.com](http://graphitestore.com), which supplied inexpensive ( $\sim \$0.10/\text{cc}$ ) large particle size ( $\sim 0.7 \text{ mm}$ ) GR030 graphite. In addition to large particle size, this graphite was 20% porous. Wherever this grade of graphite was used, it was sealed with Resbond 931S graphite sealer, at a differential pressure exceeding 1 atm, in order to prevent Sn from seeping through the pores. Figure 20 shows a graphite pipe pressurized with sealer, where the sealer is visible as it seeps through the graphite pores. Here, pipes and other flow

path components were first filled with liquid sealer, then connected pneumatically with a hose to a gas ( $N_2$ ) reservoir at 1-1.5 atm gauge pressure. Without this sealer, components such as the reservoir have been found to leak slowly, although this rate increased with temperature and can be exacerbated by thermal cycling. For custom and critical dimension components, Ohio Carbon Blank supplied both machined and bulk graphite. The grade purchased was ultra-fine molded EDM graphite AR-14, which has grain size below  $5\ \mu\text{m}$ . Although this ultra-fine graphite typically did not exhibit leaks, it was also sealed as a redundant precaution and because of the need to seal bonded joints as discussed in the next section.

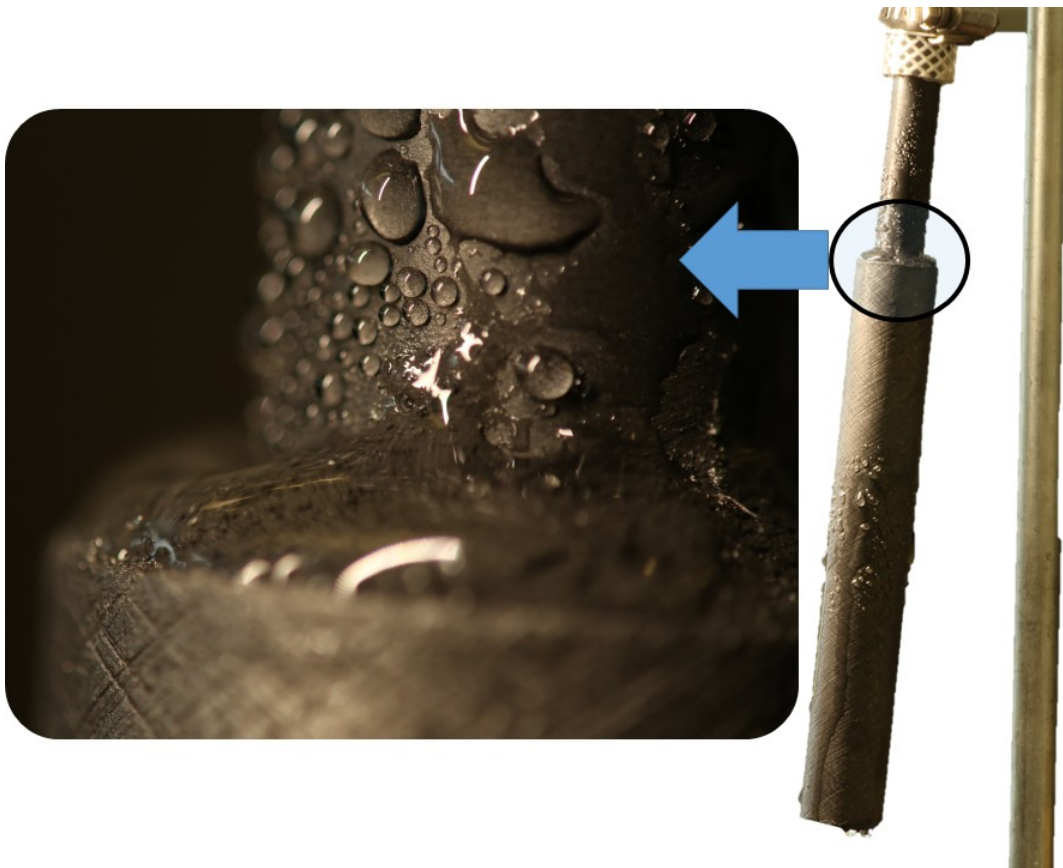


**Figure 20:** Graphite Sealer applied to a pipe and glue joint. Pipe is filled with 931S sealer. Top of pipe is connected to nitrogen reservoir at 1 atm gauge pressure and bottom of pipe is plugged.

In all tests, whether a flow meter was used or not, it was necessary to have a line of sight to the Sn exiting the pump outlet network (or flow meter), as shown in Figure 19, in order to verify the system was successfully circulating. This, of course, required to Sn to fall freely into the reservoir beneath it. This freefall resulted in significant splashing of the Sn out of the reservoir, as shown in Figure 21.



**Figure 21:** Splashed Sn around the reservoir from freefalling Sn inlet

Although several options were considered to mitigate this loss of Sn, a W mesh was finally selected to rest directly above the reservoir to reduce splashing, as shown in Figure 22. This W mesh had a spacing of 1 mm between the 0.3 mm wires, and was sandwiched between two thin layers of reaction bonded graphite (see the section: Static Seals) to keep it in place. The idea here was that the mesh would allow a steady stream of Sn to penetrate it while preventing most splashed droplets from escaping when they collided with it. This method reduced the rate of Sn lost from splashing by an order of magnitude and was largely

effective because Sn wets W, which gave the mesh an added blockage ability from surface tension. Additionally, during medium temperature tests, Sn froze on the mesh, except at the location of the main stream inlet. In this case, the frozen Sn covered nearly the entire top of the reservoir and created a lid which minimized splashing.



**Figure 22:** Tungsten mesh cover for reservoir to reduce splashing

## 4.2 Static Seals

Static seals in the circulation loop were based on two main approaches: removable and permanent. The preferred method was removable and was based on the compression of soft graphite, similar to the dynamic pump seal discussed in Chapter 3.

For the static seal between the two parts of the pump cavity (shown in Figure 7 and Figure 5), a graphite (Graphoil brand) sheet based seal was used. This method was applied to the tungsten and Inconel 625 pump as well the Shapal pump. Here, the seal was thin and

only needed to deform to fill the minute surface roughness of the pump surface. The most reliable seal approach was found to be when three sheets were used, with the middle thicker (0.8 mm) than the two outer sheets (0.2 mm). This seal was achieved by compressing the sheets using six 5 mm diameter tungsten bolts, torqued to 0.5 Nm. In the case of the tungsten and Shapal pumps, this seal was reinforced by the bolts that mount the pump.

For static sealing of pipes, commercially available soft (flake) graphite ferrules were compressed in a geometry similar to typical compression pipe fittings. Because of the extreme temperature and chemical environment present, however, the unions and nuts used to compress the ferrules were made from graphite. These components were large and coarsely threaded in order to deliver adequate compressive force without failure of the weak graphite components. Notably, graphite threads were able to survive where Shapal threads did not, even though Shapal is 1-2 orders of magnitude stronger than graphite; that is, Shapal has a tensile strength of  $\sim 300$  MPa, while graphite varies from  $\sim 4$ -40 MPa depending on the grade. Here, the key reason for the survival of the graphite threads was their large size—25mm vs. the 5mm Shapal bolts. In bolting design, this size increase corresponds to an increase in allowable load of  $\sim 25X$  because area scales with the square of diameter [81]. An image of a graphite union (and a Shapal bolt for comparison) is provided in Figure 23.

The general design principle of oversizing weak, specifically ceramic, components to enable transmission of mechanical force without failure can be applied elsewhere, too. For example, a pump could theoretically be made from C, if the shaft diameter was increased and tooth geometry was modified for higher strength—although the poor wear properties of C are expected to limit the life.



**Figure 23:** C union, W union, CrN coated steel union, and Shapal bolt for reference (from left to right). The C union is the largest because it has the lowest strength. Both the C and W unions are compatible with liquid Sn above 1350°C. The Shapal bolt, which failed, is shown as an example of the need to oversize brittle components.

Alternatively, W unions and nuts have also been developed and successfully tested, which are significantly more compact and strong. An example of this union is also included in Figure 23. These joints are, however, heavier and have a similar cost, so in situations where space allowed, C unions were used. A more complex geometry could significantly reduce the weight of these tungsten components, but in order to keep manufacturing cost down, only necessary sealing features were included.

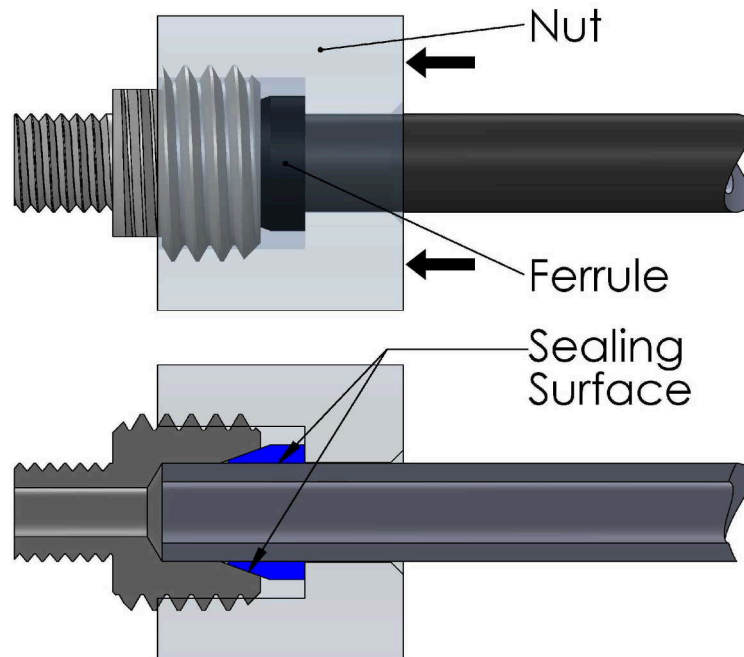


**Figure 24:** Static seal of a molten Sn fluid connection

Similarly, commercially available steel unions could be used at lower temperatures (once coated with CrN or TiN), and these were employed during early low-temperature tests where all or a portion of the loop was below 400°C. An image of these joints can also be found in Figure 23. A model of a graphite union is shown in Figure 24, which was used to interface with the pump. In this case, the male threaded component was Shapal, while the nut was graphite. Shapal is an order of magnitude more expensive and more difficult to machine, but was useful in this case because the opposite side of it was reaction bonded into the pump body. This joint represents the second approach used to achieve static seals: permanent reaction bonds.

In several situations, geometric constraints or complexity made it infeasible to use compression fittings to join components. Here, permanent connections were made via reaction bonding components to each other. This method can deliver a reliable connection

for many refractory materials, including C, Al<sub>2</sub>O<sub>3</sub>, AlN, SiC, and ZrO<sub>2</sub>, using adhesives from Cotronics, Aremco, or other suppliers.

Three materials were reaction bonded in these experiments. As mentioned above, the Shapal fittings in Figure 24 were reaction bonded into the pump body using Ceramabond 865 from Aremco. Here, the straight threaded feature was used to add mechanical strength and increase the leak path length. This joint was necessary not only in order to reduce to cost of the pump (which is a function of the maximum dimensions of each part) but also because the machining of the pump body made it geometrically infeasible to include these unions as part of a continuous component with the pump cover. Similarly, in the first set of high-temperature experiments, a ZrO<sub>2</sub> bearing was used. This bearing was bonded to its housing using Resbond 904 zirconia adhesive from Cotronics, as shown in Figure 16.

Additionally, a C reaction bond was used to adhere the reservoir to its outlet pipe. In this case, the reservoir wall thickness was insufficient to accommodate a ferruled connection. To bond these C components, Resbond 931 was used, and sealed using Resbond 931S, see [5], under pressure as described in the section on the Circulation Loop, and as shown in Figure 20. These bonding processes require relatively low (<130°C) curing temperatures, and can therefore easily be applied in the field; the process is even less complex than welding.

Unlike the bulk graphite, bonded joints were found to have medium to large pores (~1 mm), which could take several sealing processes to completely seal. However, once sealed to the extent that the sealer itself would not leak through the joint, Sn also did not leak through the joint. Here, sealer was applied as a leak test; if it leaked, the process of

pressurizing the joint with sealer and curing it was repeated. In order to qualitatively understand the effect of this sealing process, secondary electron images were rendered using a scanning electron microscope (SEM), and the elemental content of a sealed joint was determined using X-ray Diffraction (XRD). This analysis showed that, after curing, the only element present was C (at least 98.5%), and images comparing an unsealed and sealed joint are shown in Figure 25. Once the circulation loop and sealing methods were developed, the pump could be used to circulate Sn. Several initial tests were conducted after these components were developed, however, in order to control and characterize the system the flow rate needed to be metered.

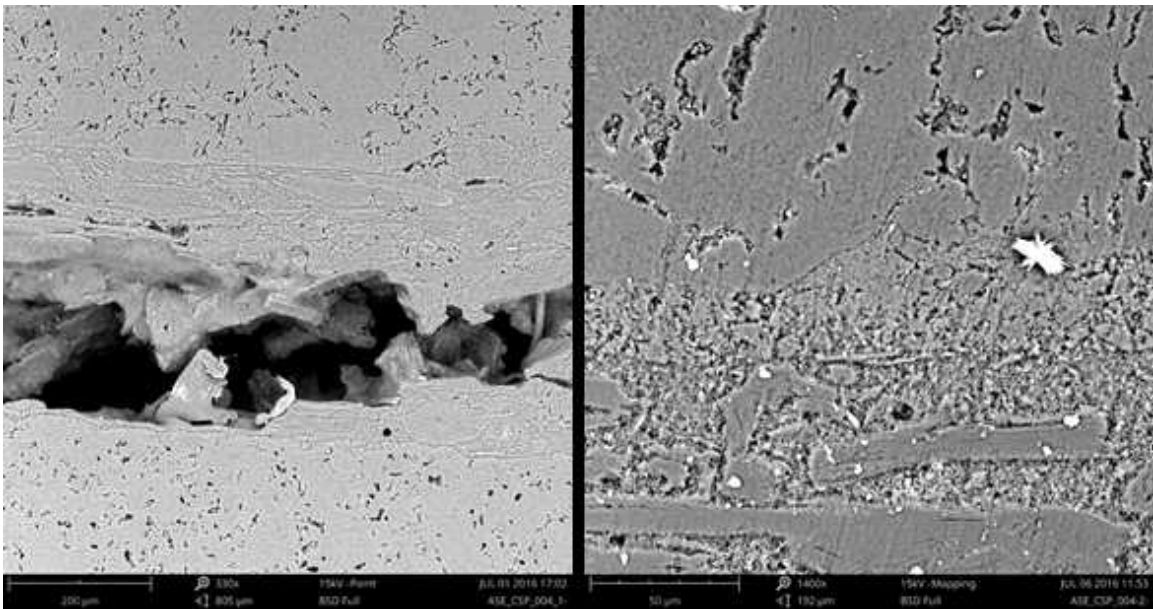


**Figure 25:** SEM images of unsealed (left) and sealed (right) reaction bonded joints. Note that the sealed image is 4X magnified, relative to the unsealed image. The images are of different joints, so it was necessary to include a magnified image to show the sealed joint.

### 4.3 Flow Meter

Although initial experiments were conducted without flow rate measurement, it was important to determine the flow rate quantitatively in order to characterize the system capabilities. Commercial flow meters could not be used because of the extreme thermal and chemical environment, so other custom flow meter designs were considered. While there are many types of flow meters that have already been developed, many were eliminated because of their complexity (which would be compounded by the extreme environment). These included vortex flow meters, positive displacement flow meters, and turbine flow meters. Here, each of these designs would require dynamic sealing, and large size to isolate electronic sensors from the extreme temperature fluid.

An array of flow meters which have only static components was also eliminated because their accuracy would be insufficient for the low flow rates present. These included several differential pressure flow meters (*e.g.*, orifice plate, venturi tube, flow nozzles, and pitot tubes). Here, the dynamic pressure in the fluid was low because its viscosity and flow rate were low. Moreover, the density of the fluid ( $\rho$ ) is relatively high (especially compared to gasses which are best suited for differential pressure measurement) so slight misalignment of a flow meter, and especially if alignment changed during an experiment, would cause major measurement error. Electromagnetic flow meters were eliminated for a similar reason, as the low flow rate would induce a very weak magnetic field, and permanent magnets could not be located near the hot zone because they must be kept below their Curie temperature ( $\sim 600^\circ\text{C}$ ) to preserve their magnetic properties [82].

Thus, with these considerations in mind, a weight based flow meter was designed. The equilibrium mass in this flow meter, which consisted of a reservoir with a base orifice was a function of the inlet flow rate. By measuring the weight of this reservoir over time,

when it was allowed to drain without inlet flow, a calibration curve was determined to relate mass to the *in-situ* flow rate. This was possible because the transient rate at which Sn drains through the orifice at a given weight is equivalent to the steady state flow rate that would maintain that height/weight. Here, the mass vs time was recorded; then, numerically differentiating in time, mass flow rate as a function of time was found. Lastly, by eliminating the time variable, mass flow rate vs mass was determined.

The weight based flow meter is shown (insulated) in Figure 26, where it was installed into the pump system. This flow meter was subject to clogging at the outlet by alumina insulation fibers circulating in the chamber, because of the small outlet orifice. In order to prevent this issue, an adjustable lid was designed to enable a continuous seal against particulate, while also allowing the flow meter to move horizontally, as shown in Figure 27. Here, the layered discs allowed the flow meter to rest completely on the scale, rather than be partially constrained by the inlet pipe. This freedom of motion was critical to prevent over constraint, which would cause significant error in the weight measurements. For example, in early experiments the flow meter was found to rub on rigid insulation which prevented its full weight from resting on the scale. Here, the change in weight of the flow meter was underpredicted by up to 50% because much of the weight was supported by the insulation.

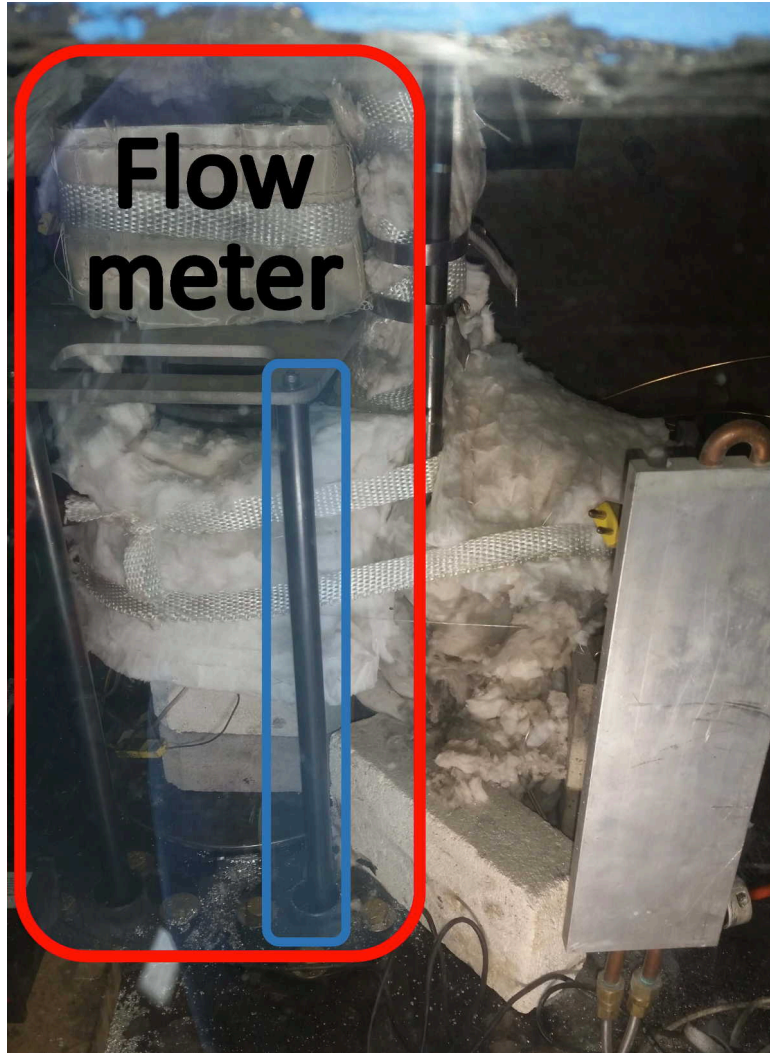


**Figure 26:** Weight based flow meter system (insulated) supported by steel legs which rest on a scale (Scale not visible)

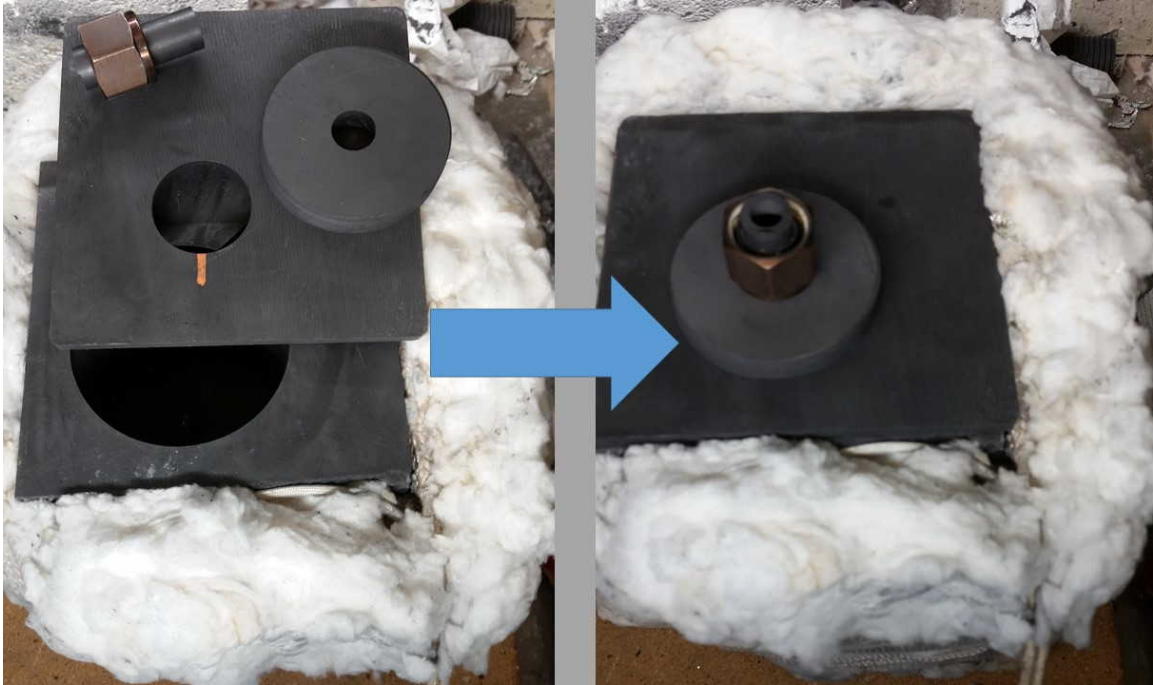


**Figure 27:** Flow meter dynamic cover which functioned as a guard against insulation particulate

Subsequent testing showed that the performance of this first flow meter matched well with predictions based on simple application of Bernoulli's equation (Equation 5) over a wide range of flow rates. Here, Bernoulli's equation (which neglects viscous effects) can be solved for velocity, as shown in Equation 6. Here, velocity is directly proportional to the mass flow rate for liquid (assuming incompressibility) flow of fixed cross section. Then, the mass flow rate is shown to be a function of mass (proportional to fluid height) as described above and shown in Equation 7. Here,  $m$  represents mass,  $g$  is acceleration due to gravity,  $\rho$  is density,  $A_i$  is the (horizontal) cross section area of the reservoir,  $A_e$  is the exit orifice area, and  $C_D$  is discharge coefficient—a fitting parameter that is a function of the orifice geometry. This equation applies at all points along a streamline.

$$\frac{U^2}{2} + \frac{P}{\rho} + gz = \text{Constant} \quad (5)$$

$$V = \sqrt{2gH} = \sqrt{\frac{2gm}{\rho A_i}} \quad (6)$$

$$\dot{m} = \frac{\partial m}{\partial t} = C_D A_i \sqrt{\frac{2g\rho m}{A_e}} \quad (7)$$

The calibration results are shown in Figure 28A, where the average of 10 drain curves is displayed, along with the theoretical function based on Equation 7. This plot depicts the calibration curve for the weight based flow meter, which was relatively simple, and involved recording mass as a function of time during a calibration drain test. Here, the pump was first run at high rpm in order to fill the weight flow meter. Once filled, the pump was quickly stopped, and the weight of the flow meter was recorded with respect to time. Mass flow rate vs mass was determined with this data, as described above.

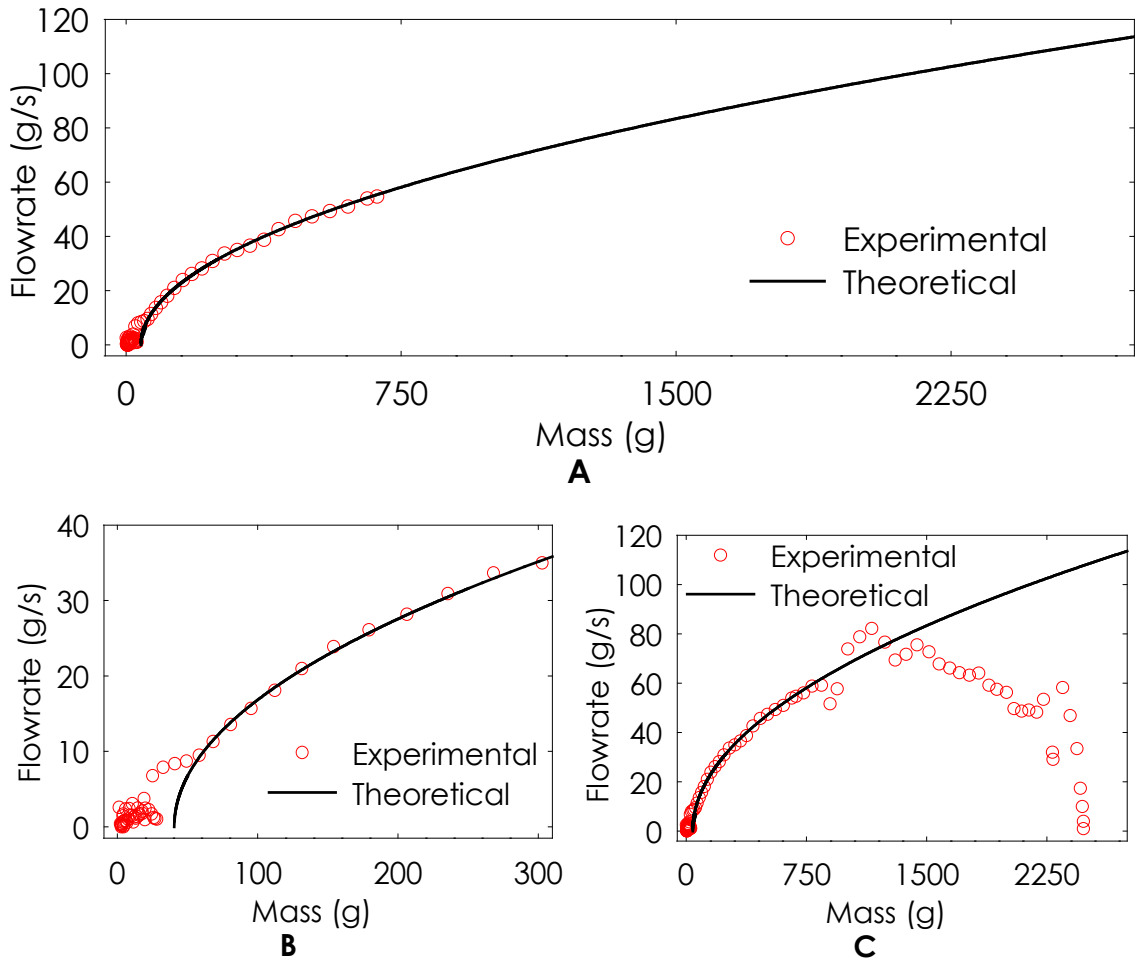


**Figure 28A:** Weight flow meter calibration showing mass flow rate as a function of the weight of Sn in the flowmeter, **B:** zoomed in on the low flow rate regime, where experimental results are inconsistent, and on average diverge from the prediction based on Bernoulli's equation. **C:** Fully displayed experimental data, showing divergence from the theoretical curve at mass measurements above  $\sim 750$  g. This was a result of delayed stopping of inlet flow. Each plot is an average of 10 tests.

Notably, the experimental data is only reported up to 750 g because above this mass, Sn was still flowing into the flow meter, as shown in Figure 28C. Here, during steady flow, the mass is constant, and thus  $\partial m/\partial t = 0$ . This explains why zero flow rate is predicted for a mass near 2500 g in Figure 28C. As the inlet flow rate decreasing when the pump stopped, the measured flow rate slowly increased, peaked, and then decreased. This was caused by a long horizontal pipe feeding into the flow meter. Therefore, as shown by

the noisy data on the right of Figure 28C, inlet flow did not completely stop until the mass in the flow meter was below 750 g. As explained above, the calibration required that the flow meter had no inlet flow, so the initial data where the mass was high could not be used. Here, the delayed stop in inlet flow resulted in the data showing artificially low flow rate until the inlet flow completely stopped. This is the case because the change in mass is proportional to the outlet flow minus the inlet flow. Nonetheless, the excellent fit to the theoretical curve suggests that at higher flow rates, the Bernoulli based model is a good approximation. In any case, the experimental data is sufficient to confirm the flow rate up to  $\sim 60$  g/s which is sufficient to report a lower bound on flow rate.

A different phenomenon was observed at very low flow rates; as shown in Figure 28B, the experimental weight measurements diverge from the prediction at flow rates below 10 g/s, which was likely caused by the effects of surface tension and tilt/angle of the flow meter becoming important when the fluid height was only a few mm. Here, the outlet flow is only dripping and does not fully drain (a disc of Sn  $\sim 3$ mm thick remained in the flow meter after each test), thus a smooth curve is not expected. Additional information about this flow meter, including theoretical performance, is shown elsewhere [34].

Another challenge presented by the weight based approach was signal drift of the weight scale. When this phenomenon was first observed, the cause was unclear, so a control test was conducted where the scale sensor and electronics were independently heated while monitoring reported mass. The scale reading drifted as much as 10%, for a fixed mass, when ambient temperature increased from 20°C to 40°C. This problem occurred even if either the electronics or the sensor were heated independently; so, to minimize the drift, only the sensor was kept in the experiment chamber. Here, the scale was essentially a beam

and strain gauge. Therefore, as the temperature changed, the modulus of elasticity of the beam changed, the electrical resistance of the strain gauge changed, and the analog electronics monitoring the strain gauge drifted. Further, as the scale temperature increased, the beam and strain gauge experienced thermal expansion, which also induced strain from the mismatch in thermal expansion rates. This issue was partially mitigated by locating the electronics outside of the nitrogen chamber and by re-zeroing the scale before and after each test. However, this did not completely solve the problem. A thermoelectric cooler (TEC) was used to control the temperature of the scale beam and strain gauges, but because the control system used simply switched between full power cooling to off at low frequency ( $\sim 0.05\text{Hz}$ ), it produced an inherently transient cooling profile, especially because the hot side of the TEC quickly conducted heat to the scale sensor when switch off. This then resulted in significant temperature swings during cycling, which simply caused the drift to correspondingly swing. Given that the mechanism responsible for the drift was identified, if a variable voltage control system was used, the scale drift could perhaps have been reduced to nearly zero. However, this issue was not sufficiently important to warrant the effort needed for continued improvement, since even the drifted signal was able to provide a sufficiently accurate signal for the intended testing.

Although this weight based flow meter performed sufficiently well, its large size (see Figure 26) made it difficult to simultaneously meter the flow and reach the target temperature of  $1350^{\circ}\text{C}$ , due to increased heat loss and limited heater power input. In light of this problem, an alternative *visual* flow meter was designed and used for the higher temperature experiments—here, temperatures as high as  $1220^{\circ}\text{C}$  were reached and even

higher temperatures ( $>1400^{\circ}\text{C}$ ) were obtained by not using a flow meter at all (see Figure 19 and Figure 57).

The visual flow meter was designed to visually confirm a flow rate between two bounds and was otherwise very similar to the mass flow meter. Shown in Figure 29, as the flow rate increased, the equilibrium height of the Sn increased, and at a certain point, flow began out of the second outlet. Similarly, at an even higher flow rate, the third outlet was also activated. Therefore, when flow was observed out of only two outlets, the flow rate was confirmed to be in between two bounds.

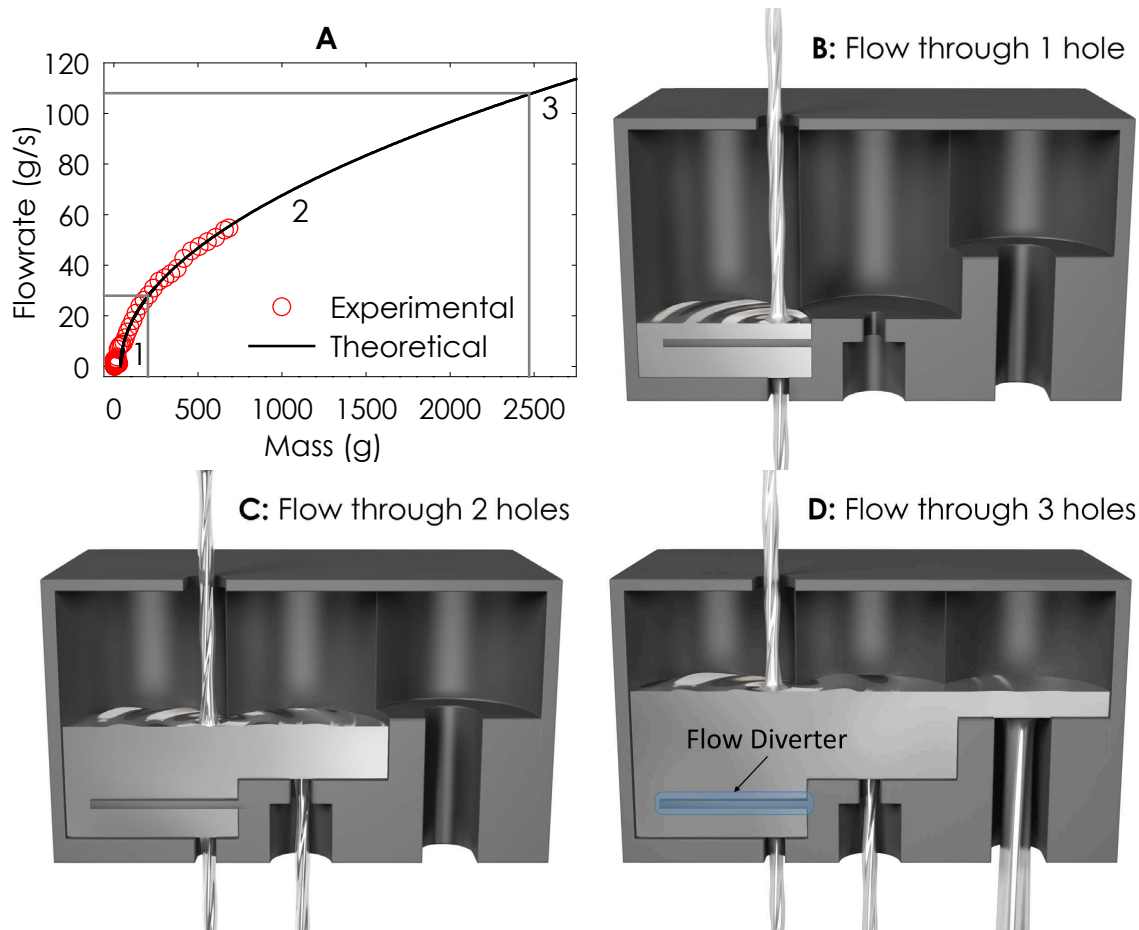


**Figure 29:** Visual flow meter design and calibration. **A:** Plot of the measured flow rate vs. mass in the flow meter (mass uncertainty  $\pm 5$ g), with identification of the flow regimes. **B/C/D:** Illustrations of three possible flow regimes that can be detected by the visual flow meter. The flow diverter used to keep the inlet flow from bypassing the flow meter is highlighted in **D**.

Although the principles behind this flow meter are simple, designing a compact flow meter in such a way that all three flow regimes were achievable—without clogging, splashing, or missing the flow meter entirely—was non-trivial. The first design variables decided were the height of each outlet and the diameter of each hole. Based on previous experience from the mass flow meter, a minimum hole size of  $\sim 4$  mm was selected to prevent clogging from tin oxide or other particulates present. Next, using Bernoulli's equation (see Equation 5), a predicted flow rate was determined for each hole as a function

of height. This model includes a discharge coefficient (see Equation 7) which was estimated based on data from the mass flow meter and is shown in Table 3. With this tool, and knowledge of the flow rate range of the pump from the mass flow meter, the visual flow meter was designed.

**Table 3:** Theoretical performance of visual flow meter

	Control (Mass FM)	Bottom Outlet	Middle Outlet	Top Outlet	
Variable	Value	Value	Value	Value	Units
Discharge Coefficient	<b>0.802</b>	0.8	0.8	0.8	N/A
Diameter	4.2	<b>3.91</b>	<b>3.91</b>	<b>11.11</b>	mm
Area	1.39E-05	1.20E-05	1.20E-05	9.70E-05	m <sup>2</sup>
Gravitational Const.	9.81	9.81	9.81	9.81	m s <sup>-2</sup>
Height	0	0	<b>0.0127</b>	<b>0.0254</b>	m
Sn Relative Height	0.06985	0.0254	0.0127	0	m
Density of Sn	7000	7000	7000	7000	kg m <sup>-3</sup>
$\dot{V}$	1.30E-05	6.79E-06	4.80E-06	0	m <sup>3</sup> s <sup>-1</sup>
$\dot{m}$	<b>0.091</b>	0.048	0.034	0	kg s <sup>-1</sup>
Two outlet flow indicates:			<b>33.6 to</b>	<b>81.1</b>	g/s

During initial testing of this flow meter, large disagreement was found with the theoretical model. One issue that occurred was that flow was only observed out of the first outlet even at very high flow rates. After some investigation, which was challenging because the experiment was conducted in a sealed chamber, it was determined that the mass and visual flow meter outlets were aligned to the extent that the fluid went straight through the visual flow meter without building up any height. The simple solution of better (mis)alignment was difficult to attain because the mass flow meter was floating on 60 cm long legs to reach the scale below the rest of the system (see Figure 26 and Figure 32). Instead, a flow diverter was designed to prevent the Sn flow from bypassing the visual flow

meter. This diverter, which directs the inlet flow to the left, down, and then to the right is highlighted in Figure 29D and shown before installation in Figure 30. Moreover, to prevent clogging and minimize alignment error, a cover was made for, and bolted directly to, the visual flow meter. Similarly, the flow meter itself was fixed to the reservoir below it by alignment pins, as shown in Figure 31.

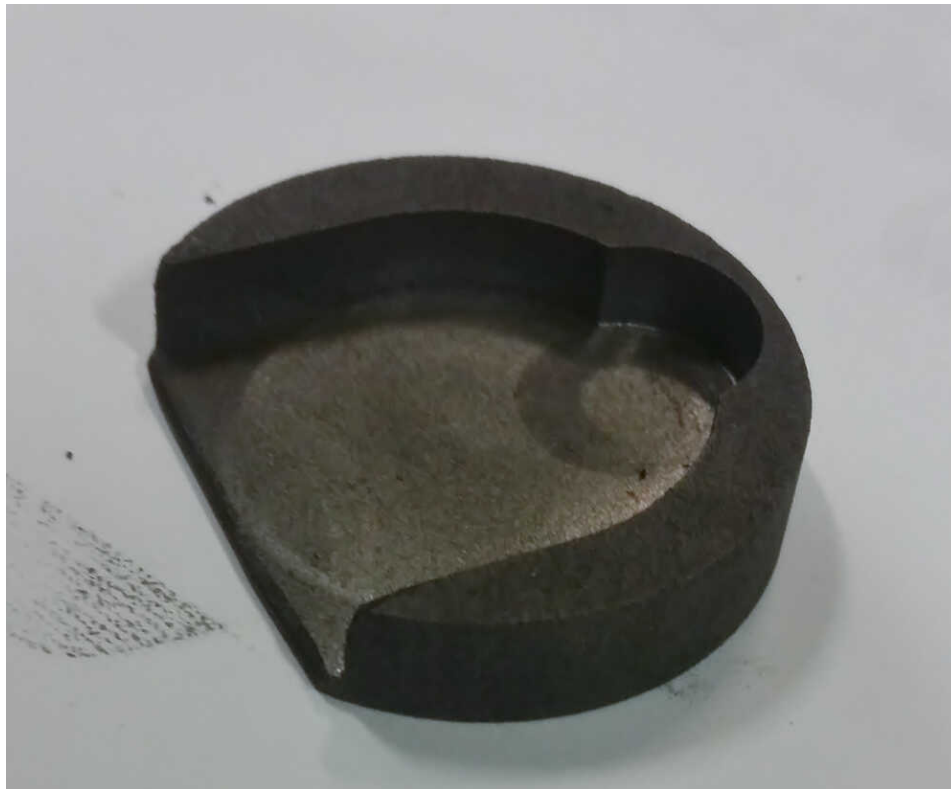


**Figure 30:** Flow diverter for visual flow meter (shown inverted)



**Figure 31:** Visual flow meter with alignment pins and cover attached with W bolts

In order to determine the upper and lower bound on flow rate, the visual flow meter was calibrated using the original weight based flow meter. To quantify the flow rate into the visual flow meter, the mass flow meter was positioned above it. This arrangement, as shown in Figure 32, allowed the mass flow meter reading to be directly related to the number of streams of liquid  $S_n$  produced. The final calibration curve shape, as shown in Figure 29A, matched very well with the theoretical result from Bernoulli's equation (see Equation 7)—flow rate proportional to the square root of fluid mass/height—over a wide range of flow rates. The theoretical and experimental curves are shown in Figure 29, along with the regimes of one, two, and three outlet flow.



**Figure 32:** Calibration of the visual flow meter, experimental setup

These regimes were confirmed by repeatedly targeting a flow rate where the 2<sup>nd</sup> or 3<sup>rd</sup> outlets were activated, and then verified by targeting this weight and verifying the same conditions existed. Here, activation of the second outlet was defined as the flow rate at which the  $S_n$  stream was continuous (not droplets) where visible. To account for the

uncertainty from visual measurement, rather than basing the reported minimum flow rate on the average value that achieved this, the lowest flow rate that achieved this condition out of the 10 tests is reported as the lower bound on two outlet flow. For three outlet flow, a steady stream was not achieved because this third outlet was large, as a safety overflow. As shown in Figure 32, the third outlet is  $\sim 10X$  the area of the others so that the flow meter would not overflow even at very high flow rates (up to  $\sim 375$  g/s). Here, activation was based on any consistent flow (more than 1 drop per second). The complete pump system, including the circulation loop and visual flow meter, is shown in Figure 33.

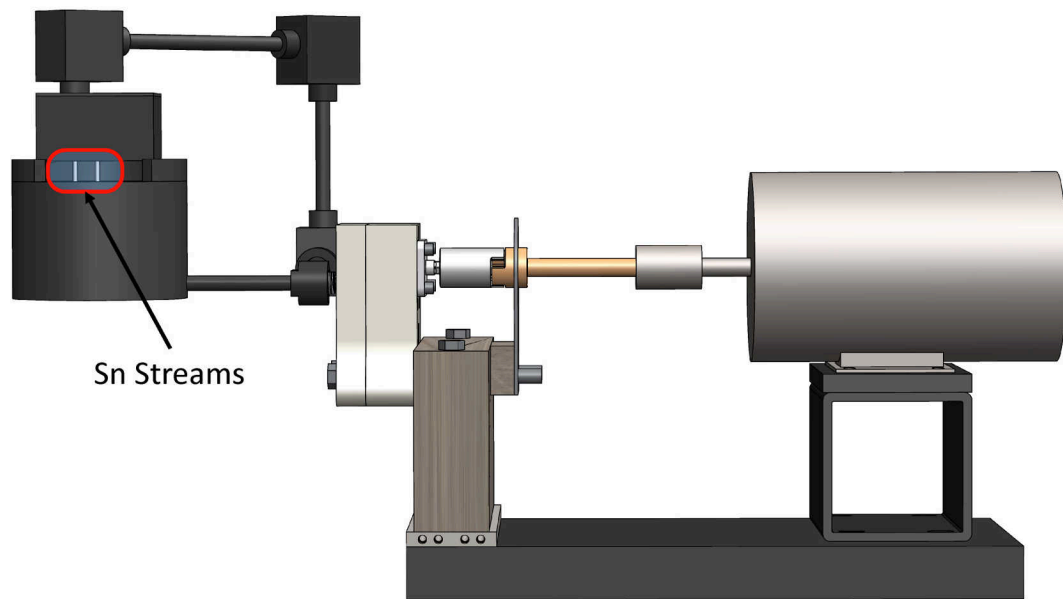


**Figure 33:** Circulation loop with the visual flow meter installed above the reservoir, shown in two-outlet flow regime.

Although this flow meter adequately performed the task it was designed to, its output was essentially ternary. In order to achieve a continuously variable signal, without the large size and complexity of a weight based flow meter, a method to directly measure

the height of fluid in a similar reservoir with orifice could be developed. For example, this height could be determined using a laser-based technique. A laser and detector could be located above the reservoir, sufficiently far away to remain cool. The time delay of a laser pulse can be measured by the detector, and its variation can indicate Sn height, and by the relation explained previously, flow rate. A similar approach based on a sonic sensor could also be applied, although local changes in temperature affect the speed of sound and would cause measurement error. This exemplifies one key benefit of the laser based system: it is temperature independent (neglecting the very small effect of the temperature variable refractive index of N<sub>2</sub> gas). Nonetheless, these methodologies would be ideally explored in future work.

#### **4.4 Thermal Management Equipment**

Heating, cooling, and insulating components in this experiment involved significant effort, because of the extreme temperatures, thermal gradients, and limited space. Although in commercial systems (*e.g.*, CSP) the heat source is large and, by design, capable of heating the working fluid sufficiently, in this lab-scale experiment, the temperature was actually limited by the heater—instead of the material limits of primary system components. In addition to the challenge of getting the system as hot as possible through heaters and insulation, maintaining metal and polymer components (*e.g.*, motor, thermocouple plugs, and other sensors) near room temperature while in close proximity to the circulation loop at the peak temperature was also difficult, and required multiple active and passive cooling methods.

##### *4.4.1 Heating Equipment*

The pump and circulation loop were heated to the target temperature primarily by a 10kW maximum high frequency (100-500 kHz) induction heater. Inductive heating enables extremely high-temperature tests—only limited by the combination of heater power and insulation—with a simple, reliable, and precisely controllable setup. Extreme temperatures are enabled because the heater itself remains cold, and only heats the workpiece by exciting electron eddy currents within it. After testing multiple configurations, the highest power input was found to occur where the cylindrical Sn reservoir was heated by a single circular coil around it. In addition to higher heat input, the single coil design also had lower heat rejection through the water-cooled coil, which was had a more significant effect at high temperature and the marginal increase in power input by reducing the number of coil loops.

These power optimization tests included monitoring the temperature rise of the reservoir and the induction heater power output indicator for each configuration. In order to estimate the amount of heat generated in the reservoir, a transient thermal model, developed in COMSOL and described in Chapter 3, was fit to the temperature data from two tests: with one loop and with four loops. In this model, radiation and convection were simulated on all external surfaces, except the bottom which was insulated. The emissivity of graphite and Sn was taken as 0.75 and 0.15 [83, 84], respectively and the natural convection coefficient was prescribed as  $5 \text{ W m}^{-2} \text{ K}$ . Here, the convection coefficient was estimated by approximating  $L$  as 0.1 m, the length scale,  $u$  as  $0.1 \text{ m s}^{-1}$ , the average velocity inside the  $\text{N}_2$  chamber. These inputs, as well as the properties of  $\text{N}_2$  at  $40^\circ\text{C}$  were used to solve Equation 8, the average convection coefficient for laminar external flow over a flat plate [85].

$$h = 0.664(uL/\nu)^{1/2} \text{Pr}^{1/3} k/L \quad (8)$$

It is important to note that the thermocouple was buried in the reservoir wall, 3 cm from the top. This location was not ideal because there was a significant thermal gradient in this region. Therefore, the simulated fitting curves likely have significant error—~500 W variation in power is predicted if the thermocouple, or level of Sn, was 10 mm off in the vertical direction--although the relative comparison is valid. Nonetheless, this location was matched in the COMSOL model to enable 1:1 comparison.

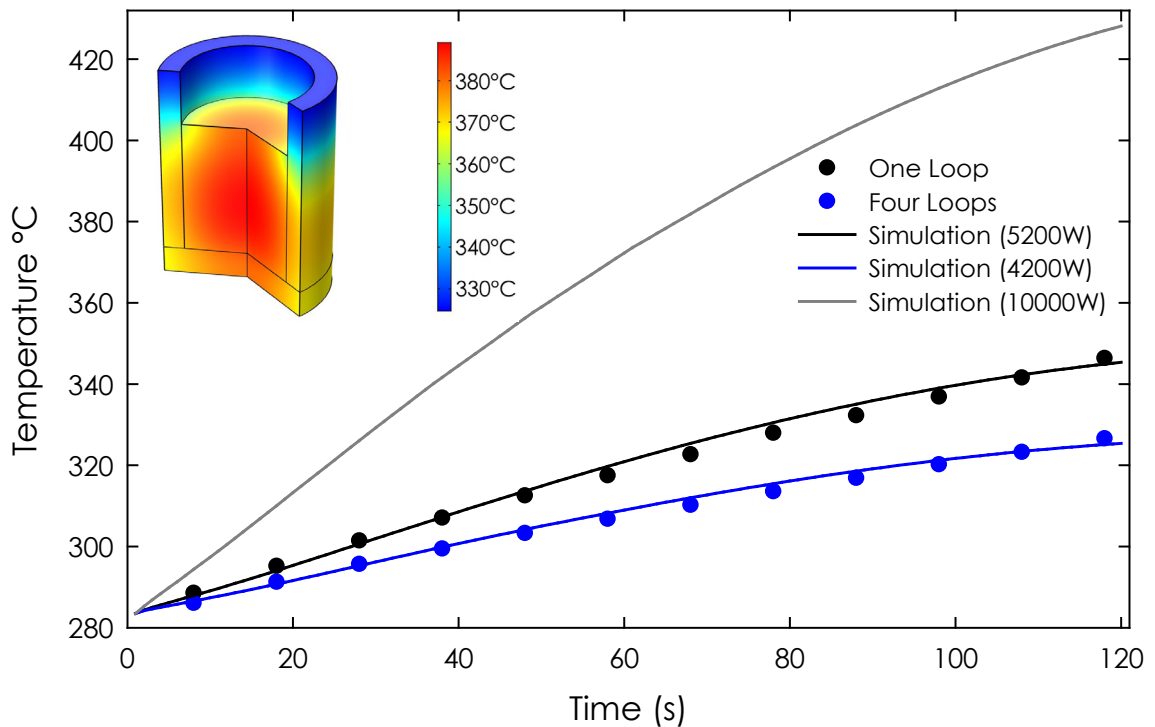


**Figure 34:** Comparison of the temperature profile of a reservoir filled with Sn under transient inductive heating. A single coil resulted in ~20% more power coupled than four coils, although only half of the rated power was coupled.

In future tests, the thermocouple was buried in the bottom of the reservoir, near the Sn, and thus gave a better indication of the average temperature of the reservoir. Shown in Figure 34, the estimated power coupled (based on uniform heat generation) with one loop of induction coil is 5200 W, which is 1000 W more than the four-loop case. Notably, the induction heater displayed a power of 6100 W, which is based on the electrical current through, and voltage drop across, the coil, and is thus an upper limit on the actual heat generated in a workpiece. Also included is the predicted temperature rise if the full 10,000 W of rated power was able to be coupled, for reference. Overlaid on this plot is the temperature profile of the Sn filled graphite reservoir after two minutes of heating at 5200 W. It is important to note that this test was conducted at a starting temperature of  $\sim 280^{\circ}\text{C}$ , in order for the Sn to be liquid. This was desirable both to better match actual experimental conditions and to simplify the modeling so that only sensible heating was considered. This high starting temperature was also necessitated by the fact that many coil geometries were being tested and test frequency was increased by not waiting for complete cooling. That is, to start each experiment near room temperature would have caused each test to take several hours. Unfortunately, operating this test well above ambient temperature increased the heat loss from the reservoir, which increased error in the modeled results as the main uncertainty was in radiative and convective heat loss. For example, the emissivity of the Sn is highly variable as its surface became increasingly oxidized throughout the tests. Further, the convection coefficient estimation did not account for drafts in the room or temperature dependence.

During each of these tests, the coil spacing was kept constant, by winding the coil around the same cylinder of appropriate diameter. An image comparing two of the several

configurations tested is included in Figure 35. This water-cooled coil, shown in Figure 36, was spaced 3 cm from the reservoir, separated by rigid alumina insulation, to minimize heat loss to the coil caused by the 1300°C temperature gradient which existed during the primary experiments, although this pretest was conducted below 400°C.

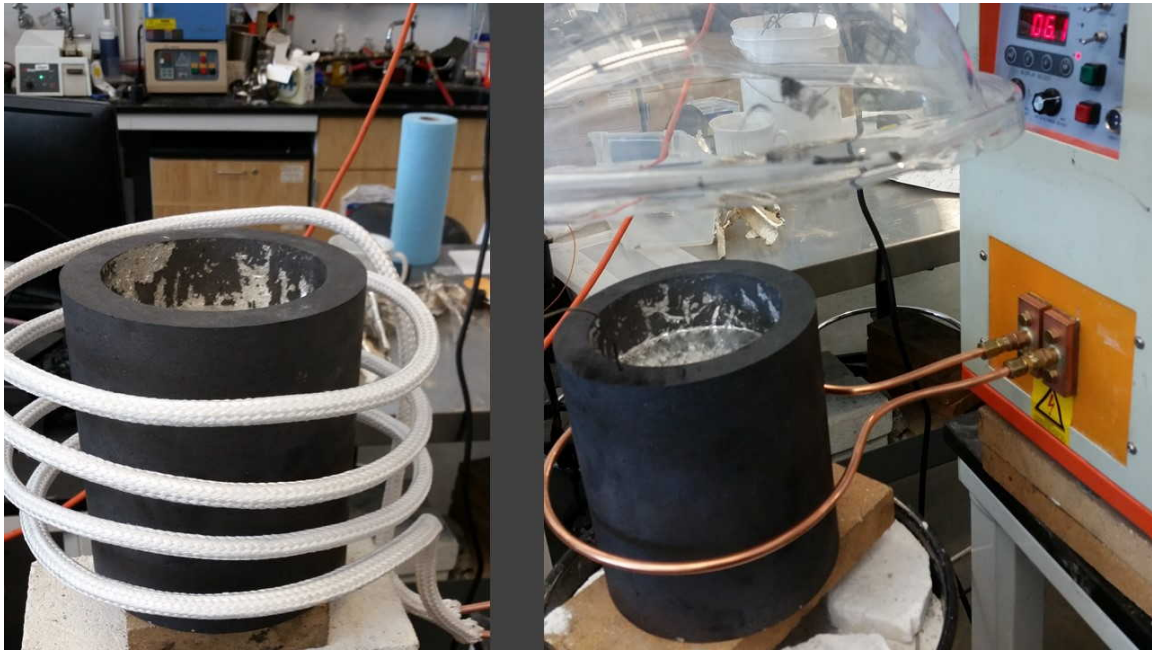


**Figure 35:** Comparison of single-coil and four-coil induction loops

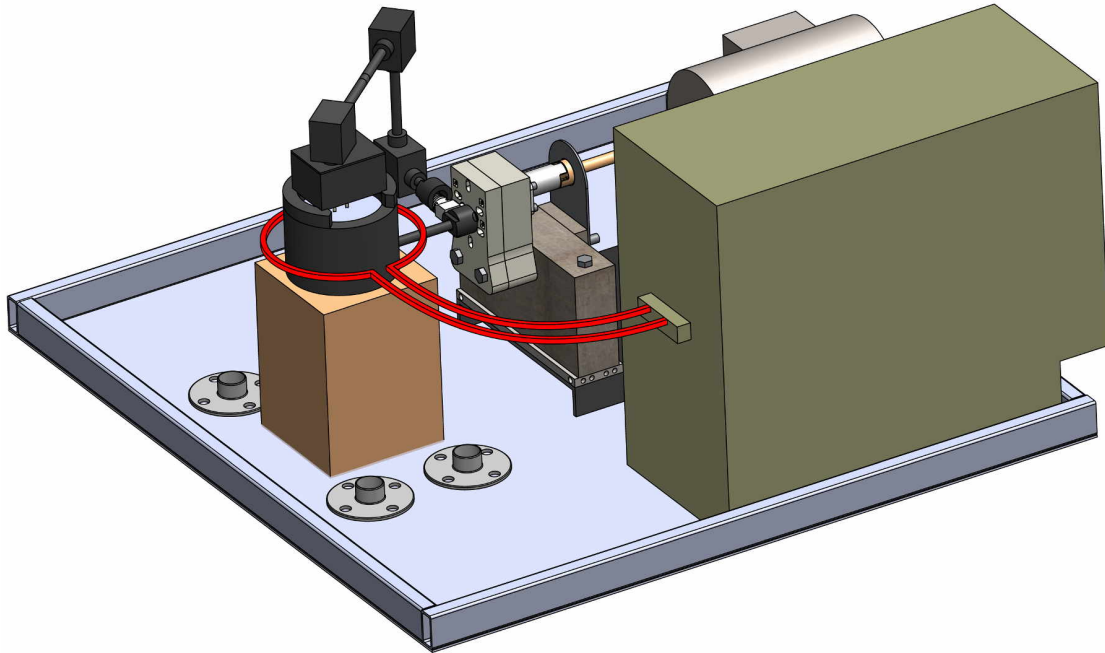


**Figure 36:** Model of induction heater with circulation loop

To determine the appropriate coil spacing, which is a balance between maximizing power input by magnetic coupling and managing the heat removed by the coil, the effect of coil diameter on power input was experimentally checked. It was found that at a coil spacing of 2 cm, as shown above, power coupling was  $\sim 5$  kW, and only a few hundred more watts were coupled with closer spacing. Thus, because a detailed thermal model of this situation was both beyond the scope of this work and would rely on unknown opacity of the porous insulation, the heat loss to the coil was monitored in an experiment. Here, the coil cooling water flow rate was measured to be 2 gpm, and the temperature rise in the coolant when the reservoir was at  $1350^{\circ}\text{C}$  was found to be  $2 \pm 1^{\circ}\text{C}$ . The uncertainty on the temperature measurement is high because the thermocouples were not calibration; instead, the difference in voltage generated when the two thermocouples were at the same temperature was subtracted from the difference in use to estimate the actual temperature

difference. Thus, from an energy rate balance based on Equation 9, the heat loss was found to be ~1kW. Notably, with four coils, the heat rejection would be ~4X that of the one coil design, except that this massive heat loss would prevent reaching very high temperatures.

$$q = \dot{m}c\Delta T \quad (9)$$

As described in Chapter 5, in the final experiments, the temperature was limited by heater input, so coupling more power would be been very useful. Two ways to do with without purchasing new equipment include reducing heat loss to the coil and increasing the coupling between the coil and workpiece. One way to reduce heat loss to the coil (which was about 25% of heat input) would be to decrease its radiative absorbance. Since this coil was copper, it could be coated with a more reflective metal, like silver. To increase coupling, the coil could be spaced slightly closer, but the largest increase was found to result from using a taller reservoir (20 cm instead of 10 cm) full of Sn. Here, a short reservoir was used to keep the system compact, but about 2 kW of additional power can be coupled by using a taller reservoir, and in retrospect, this benefit outweighs the cost of increased system size. Another approach to increase heater input is to use multiple heaters. Although it was cost prohibitive to purchase another induction heater, resistance heaters were used to supplement the induction heater.

Since Sn has an extremely high convective heat transfer coefficient, it can effectively distribute heat throughout the loop during operation. However, in order to preheat the system and provide auxiliary heating to reach higher temperatures, two types of heaters were used. For experiments/locations below 600°C, fiberglass insulated resistance heat tapes from Omegalux (model STH051-0X0, where X is length in feet) were

used, as shown in Figure 37A. On the other hand, as most experiments exceeded 1000°C, Kanthal A1 based resistance heaters were used—insulated by high alumina sleeving—as shown in Figure 37B. Kanthal A1 is a ferritic iron-chromium-aluminum alloy (FeCrAl), with the primary dopant being chromium, at ~22%.

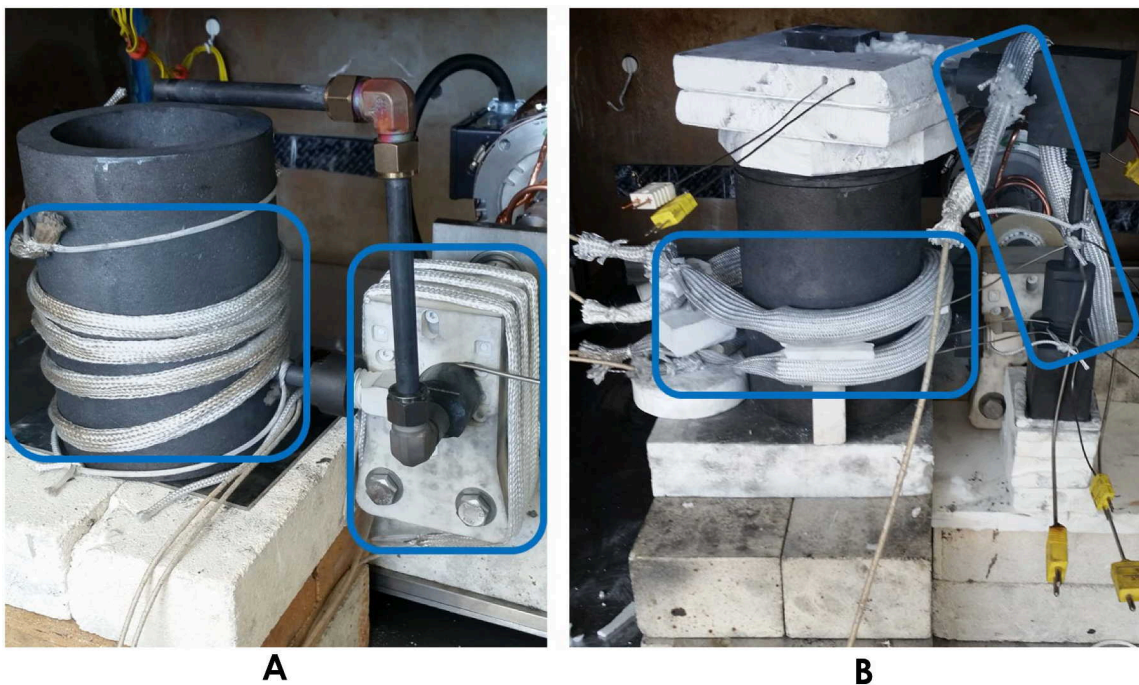


**Figure 37A:** Fiberglass insulated heat tape, **B:** Alumina insulated Kanthal heater

#### 4.4.2 Cooling Equipment

Components closest to the hot zone—the pump base plate, motor, and induction furnace—were actively cooled. As noted in Chapter 3, the motor was oil cooled with a cooling jacket and the pump base plate was isolated from the refractory brick the pump was mounted to by a custom steel oil cooled plate. This plate had four large channels which effectively maintained the bottom of it near the oil temperature (<50°C). In addition, the section of the induction heater control unit that was near the hot zone was separated by a

cold plate as a precaution (visible in Figure 26, without the heater installed). These three components were cooled in parallel, sharing a flow rate of 2 gpm, with Paratherm NF, a high purity mineral oil.

The ambient gas inside the nitrogen chamber was cooled by two fan coolers, which in series also received 2 gpm of Paratherm NF. Also, importantly, the induction heater coil and internal electronics were cooled using a water based coolant with ethylene-glycol additive. Optimally, the induction heater would have also been cooled with oil as well, but this would have required exchanging the many internal EPDM rubber O-ring seals with Buna-N seals, which are compatible with mineral oil. . All these fluids were transported through the chamber boundary using steel cord grips with rubber gaskets and were redundantly sealed with silicone and vacuum grease. It was critical not to have any oil or water coolant leaks as these introduce reactive vapors into the system, especially in the hot zone. The oil was cooled outside the N2 containment system by pumping it through a shell-and-tube heat exchanger where it exchanged heat with chilled water. Figure 38 shows the coolant tubing network for the oil cooled components.

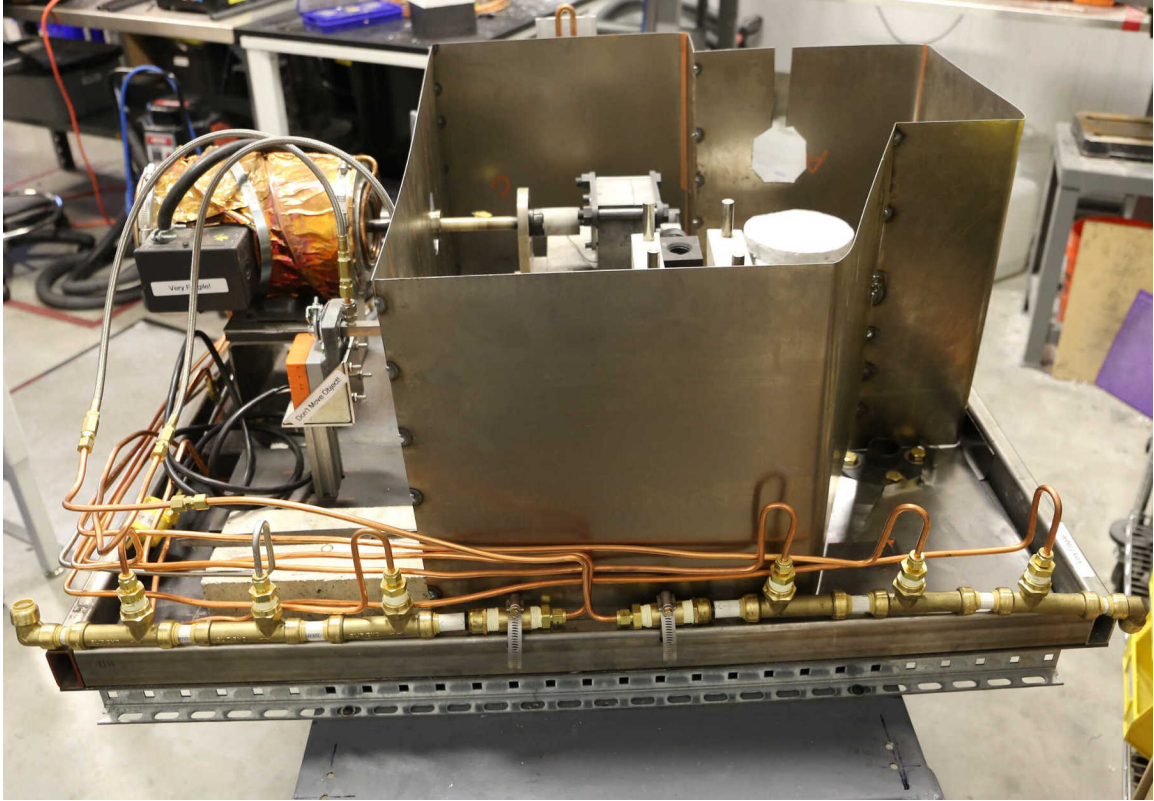


**Figure 38:** Cooling network showing oil cooled tubing and components

#### 4.4.3 *Insulation*

The hot zone, which included the pump and the circulation loop, was insulated primarily with ZIRCAR Ceramics AB high alumina blanket (95% alumina). This material is very flexible and has an uncompressed packing density of about 6% and a thermal conductivity at 1350°C of  $0.30 \text{ W m}^{-1}\text{K}^{-1}$ . Where possible, ZAL-15AA (97% alumina) rigid insulation was used for its lower thermal conductivity ( $0.20 \text{ W m}^{-1}\text{K}^{-1}$ ) and its uniform structure—which enabled access to its stated thermal conductivity (whereas the blanket insulation required careful installation to minimize thermal conductivity). A comparison of the rigid and blanket insulation is shown in Figure 39.



**Figure 39:** Alumina blanket (left) and rigid (right) insulation

External to this alumina-based insulation, MICROSIL microporous silica blanket and rigid insulation was used for its very low thermal conductivity ( $0.04 \text{ W m}^{-1}\text{K}^{-1}$  at  $1000^\circ\text{C}$ ). It could not be used in direct contact with the hot zone because it is limited to  $1000^\circ\text{C}$ , above which it would sinter and lose its insulating properties. Additionally, in the very low oxygen content environment present, silica favorably forms SiO gas above this temperature. This insulation, unlike the alumina which is bulk fibers, consists of ultra-fine silica powders contained in a box stitched blanket—similar to a down comforter. Because of this composite structure, when the insulation was cut to fit specific geometry, the powder was exposed, which made it difficult to keep the powder in place. The loss of powder reduced the insulative ability and easily became airborne because of its low density, settling all over the surrounding area. An example of the insulation process is shown in Figure 40. In some experiments, an insulation shell made with sheet steel (see Figure 38) was used, which enabled more consistent insulation and provided a rigid surface to pack the flexible

alumina blanket against. This shell was bent/welded to shape and included ports for the pump shaft and other auxiliary components—as such, it could only be used for a specific setup, so it was not used for most tests.



**Figure 40:** Insulation process for experiments above 1000°C

#### 4.4.4 *Temperature Measurement and Control*

To monitor the temperature in this experiment, K-type thermocouples were predominantly used, along with B-type thermocouples where temperatures exceeded 1250°C. Although much of the system was designed to be above 1250°C, in practice there was a significant temperature gradient throughout the circulation loop, so B-type thermocouples were only required to monitor the temperature of the reservoir and pump. Wherever possible, thermocouples were buried in the bulk component in order to acquire an accurate temperature measurement. In several locations, but most notably the reservoir, the metal thermocouples would react with the graphite components at temperatures above

~700°C. To prevent this, the thermocouple tips were shrouded in rigid alumina tube, which caused a temporal lag, due to the additional thermal resistance, but did not significantly affect the steady temperature measurement.

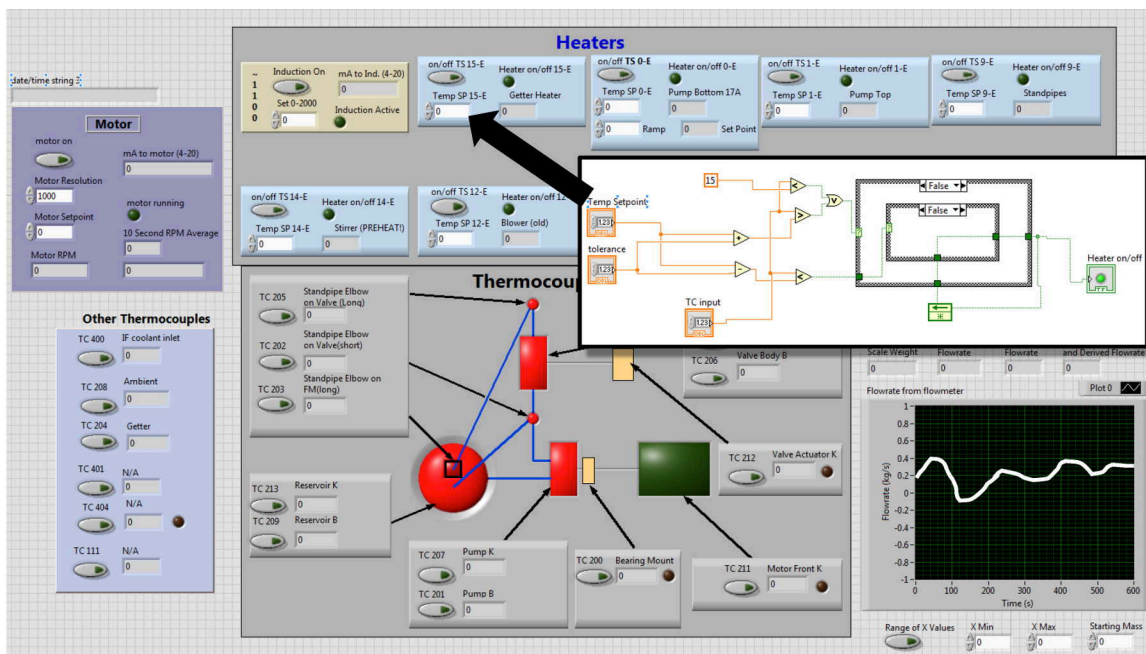


**Figure 41:** LabVIEW Front Panel, with a view of the block diagram used to compare thermocouple temperature to the set point temperature.

The entire experiment was controlled in LabVIEW, as displayed by the Front Panel shown in Figure 41. Here, thermocouples, motor rpm, and flow meter scale signal was displayed; similarly, heater temperature, motor throttle, and cooling fans were controlled. All heat tapes and Kanthal heating elements were controlled via on/off triggers (shown in Figure 41), based on relays triggered by respective thermocouple signals. The induction heater was controlled using proportional control in order to target both a ramp rate and final temperature. LabVIEW was also used to initiate the oxygen getter (described in the section on the Nitrogen Chamber) and coolant fans and to monitor the temperature of each component, in addition to the ambient and coolant temperatures. The system, shown in

Figure 42, was capable of monitoring 51 temperature measurements and controlling 23 power outputs, for a total of more than 40 kW power input to the system. Moreover, the system was monitored with cameras displayed and recorded on the control computer.

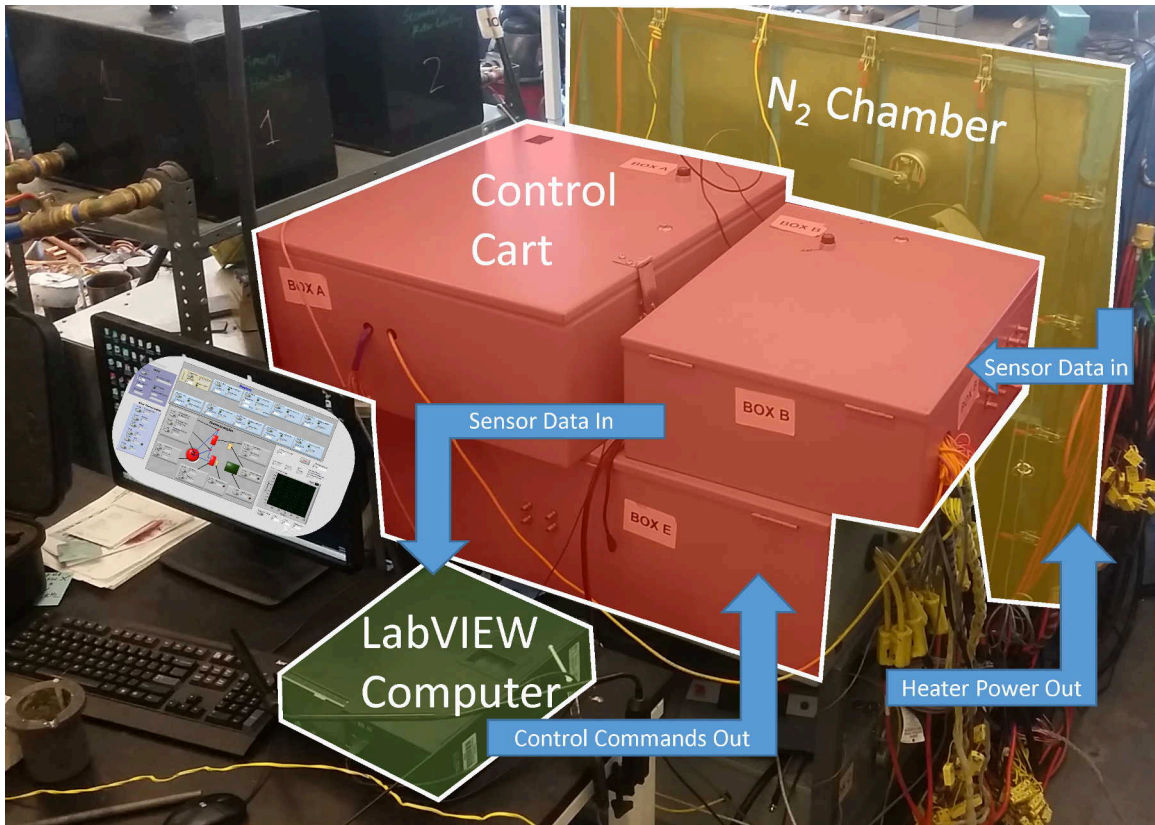


**Figure 42:** Control System showing flow of information from LabVIEW to N<sub>2</sub> Chamber

#### 4.5 Nitrogen Chamber

As discussed previously, the inert gas environment was key to the stability of the system designed. Literally every material used in the pump and circulation loop would suffer severe oxidation if exposed to ambient air at the target temperature of 1350°C; it was, therefore, critical to create a hermetic system boundary and remove oxygen from it to maintain a low partial pressure. Although a vacuum chamber can achieve the desired

results on the lab-scale, that approach is largely infeasible at large scale because of the pumping power and pressure difference required; the latter makes the system more prone to leaks and also requires very stiff walls.

Instead, this experiment relied on a nitrogen gas environment supplied by a custom nitrogen chamber. The chamber measured 4 feet by 4 feet wide and 5 feet tall. It included an 18 inch by 24 inch window and one full vertical wall as a door (see Figure 45). The seals on the door and all other joints relied on a silicone seal backed by vacuum grease. In order to remove oxygen from the chamber, it was first purged with dried ultra-high purity nitrogen (<1ppm), until the oxygen level was about 100 parts per million (ppm). Then, the vast majority of the remaining oxygen was removed by forming tin oxide in a separate getter, shown in Figure 43. This getter consisted of a graphite blade which stirred a heated vat of Sn in order to continually create a free surface of Sn for formation of tin oxide. This actively stirred getter, unlike conventional static getters, enables the entire volume of Sn to be converted to oxide which enabled consumption of a large amount of oxygen in a compact space. The getter also operated at relatively low temperature (~300°C compared to 400-1400°C) and collected oxide which could be later quantified. A combination of factors influenced the equilibrium oxygen partial pressure while the getter was activated, but further knowledge of the oxidation kinetics of Sn as a function of oxygen pressure is needed to quantify the practical lower limit for oxygen content using this Sn getter. DampRid moisture absorber was also used to remove water vapor from the gas environment. This vapor can crack and oxidize components at these extreme temperatures, and is also detrimental to the strength of ZrO<sub>2</sub> at moderate temperatures [67], as described

in the Material Selection chapter.  $ZrO_2$  was used to extend the pump shaft, and was initially used to support this shaft, as described in Chapter 3.

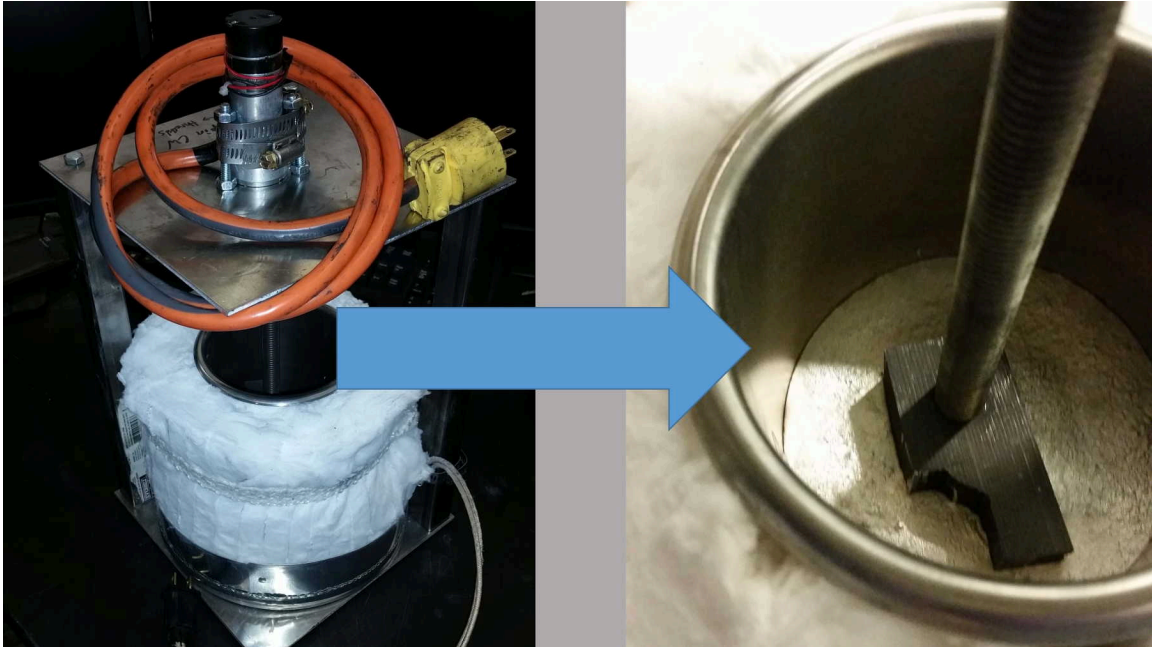


**Figure 43:** Sn Getter for oxygen removal via the formation of tin oxide

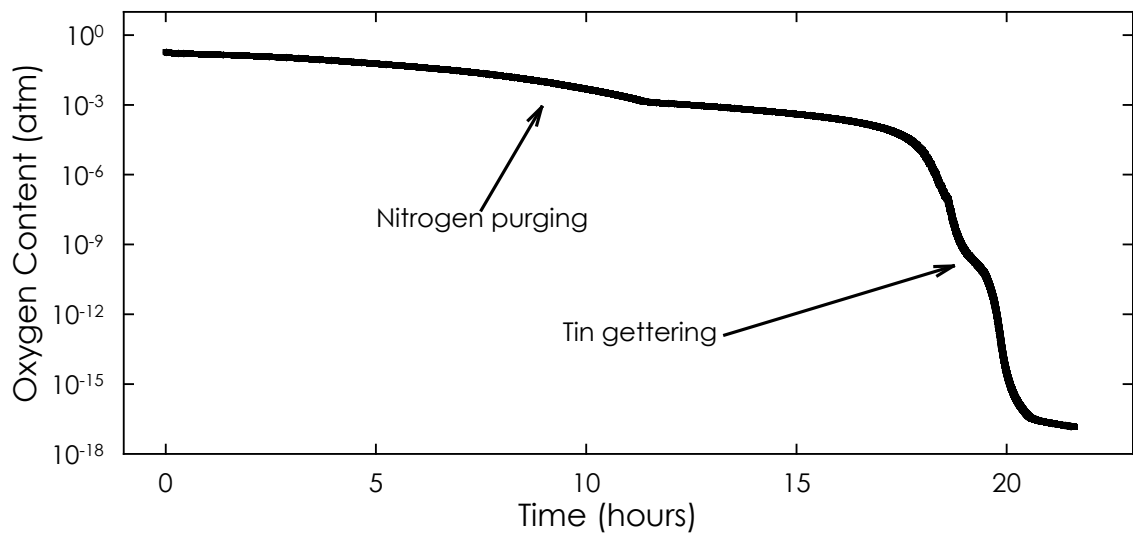


**Figure 44:** Oxygen content over time during oxygen removal process in preparation for high temperature experiments

Oxygen content in the experiment chamber was measured with a Zirox ZR5 zirconia based sensor. This sensor measures the electrical conductivity of a zirconia electrode, which conducts both electricity and oxygen ions, and the electrical conductivity is a function of oxygen content. By purging with ultra-high purity nitrogen, and gettering with liquid tin, oxygen levels near  $1 \times 10^{-16}$  atm were achieved, even reaching as low as  $1 \times 10^{-22}$  atm in some experiments. Figure 44 shows the oxygen content vs. time on a log scale, with the change in slope due to the primary purging mechanism changing to gettering. At oxygen levels this low, the remaining oxygen can react with the C and Sn in the system with negligible oxide formation.

Quantifying the leak rate was also important, because partial pressure may be artificially suppressed by a rapid oxidation process inside the chamber. Here, once the circulation loop was heated to  $1350^{\circ}\text{C}$ , any moderate leak could be suppressed by the oxidation kinetics of C and Sn, which are greatly accelerated at high temperature. By leaving the chamber sealed but not purging or gettering over several days and measuring the change in oxygen concentration, the leak rate was calculated as only corresponding to  $1 \times 10^{-13}$  grams of tin oxide formation after 30 years of operation. Even when this is scaled to the length of seals in a representative CSP plant, far less than a gram of oxide would be formed in 30 years. This leak rate can be reduced even further by maintaining a slight positive pressure ( $\sim 0.05$  psi) in the chamber. Further, as noted, the sealing technique used to achieve these leak rates is not complex or cost prohibitive [45-47]. Here, joints are located away from the hot zone and sealed with silicone, backed by vacuum grease. Figure 45 shows this sealing method applied to a window and welded joints.



**Figure 45:** Chamber view including seals and visual flowmeter port

This chamber includes an 80/20 extruded aluminum frame to support the experiment table, shown in Figure 46. Because of the constraints imposed by the walls of this chamber, the circulation loop was completely assembled outside the chamber and then rolled in from a cart by the use of two sets of rolling rails, as shown in Figure 46. Once installed, coolant, power, thermocouple, and other signal connections were made.

Now that the auxiliary components had been designed and fabricated to support the pump system described in Chapter 3, tests could finally proceed in order to answer the key question: can a pump be designed from ceramics to circulate liquid metal that survives this extreme environment with long life, and without breaking or leaking? The results of these tests, including several successes and many failures, is reported in Chapter 5.



**Figure 46:** Nitrogen Chamber railings and 80/20 frame for installing experiment table

## **CHAPTER 5. EXPERIMENTAL RESULTS AND DISCUSSION**

Once the pump system and experimental setup were complete, testing of the entire system began. Although a successful test was eventually run, which validates the principles asserted and serves as a proof of concept that liquid metal can be continuously circulated above 1000°C, it was preceded by many failures. These failures tested the assumptions employed throughout the design process and provided critical information for the design revisions applied to the final system which used a Shapal pump to circulate Sn for 72 hours at an average temperature of 1200°C (see Figure 60).

### **5.1 Medium Temperature Pumps**

As discussed in the section Primary Pump Material, in Chapter 3, a pump was made from Inconel 625 and coated with chromium nitride (CrN). This pump was tested many times without failure or leaks including two 40 hour tests, at flow rates above 28 g/s. It is important to emphasize that this metal pump relied heavily on a CrN coating, which slowly wears off the gear teeth during operation. Although this wear did not cause failure in the timespan in which the pump was used, it is likely the life limiting component. As an example of the sensitivity of this coating, it failed after light scratching from a stainless-steel pick. Here, during an inspection of the pump gears, Sn was lightly picked off using a dental pick, and after reassembling and testing the pump its performance degraded rapidly, and the teeth were found to have corroded significantly, as shown in Figure 47.



**Figure 47:** Corrosion on Inconel 625 gear teeth after scratching

Another issue that was encountered during these initial experiments with the Inconel 625 pump was excessive oxidation. Although during most future tests the  $N_2$  chamber sealed well, during some tests, significant amounts of tin oxide formed as was visible in the getter and on the surface of most components inside the chamber. This oxidation did not cause failure during short, medium temperature experiments, but it indicates significant oxygen levels which would eventually cause graphite components to fail from oxidation, cause excessive depletion of Sn, and could cause SnO clogs in the circulation loop. Severe oxidation observed from one of these tests is shown in Figure 48, where the SnO is a greenish powder that deposited on the fan cooler and cooling pipes, in addition to the what was found on the surface of the reservoir and getter.



**Figure 48:** Excessive oxidation after test with Sn at 400°C

Additionally, during these medium temperature experiments, many tests failed due to Sn leaks. Leaks typically occurred at joints, although in some cases they occurred through the wall of bulk graphite and the pump shaft seal. The shaft seal leak was always found to be a result of the bolts that compress the seal being loose. Tightening these bolts solved the issue, although a thread locking solution and/or the use of Belleville (conical) washers to maintain sealing force during wear could prevent this issue. Similarly, leakage through the bulk/body of graphite components was prevented by applying a sealer as described in the section on Circulation Loop of the Experimental Setup chapter.

Leaks at fluid connections were caused by two issues, depending on the joint type. For reaction bonded joints, most joints leaked unless sealed as described in the Static Seals section of the Experimental Setup chapter. However, after applying this sealer these joints did not leak. Leaks at removable fluid connections, on the other hand, were typically caused

by insufficient compression of the graphite ferrule, as shown in Figure 49. While torque is typically used a metric for installing compression fittings, it is an insufficient method in this case because the graphite components are too dissimilar/unique. For example, at a given torque, one joint may be adequately sealed while another may not have engaged the ferrule at all. This is because the hand tapped graphite threads caused an inconsistent amount of friction, which could dominate the torque required install the compression nut. Therefore, in practice, it was found best to note the linear or angular displacement of the nut to predict the amount the ferrule was compressed. In some cases, the nut was removed to visually inspect the joint, which was the most full proof approach.

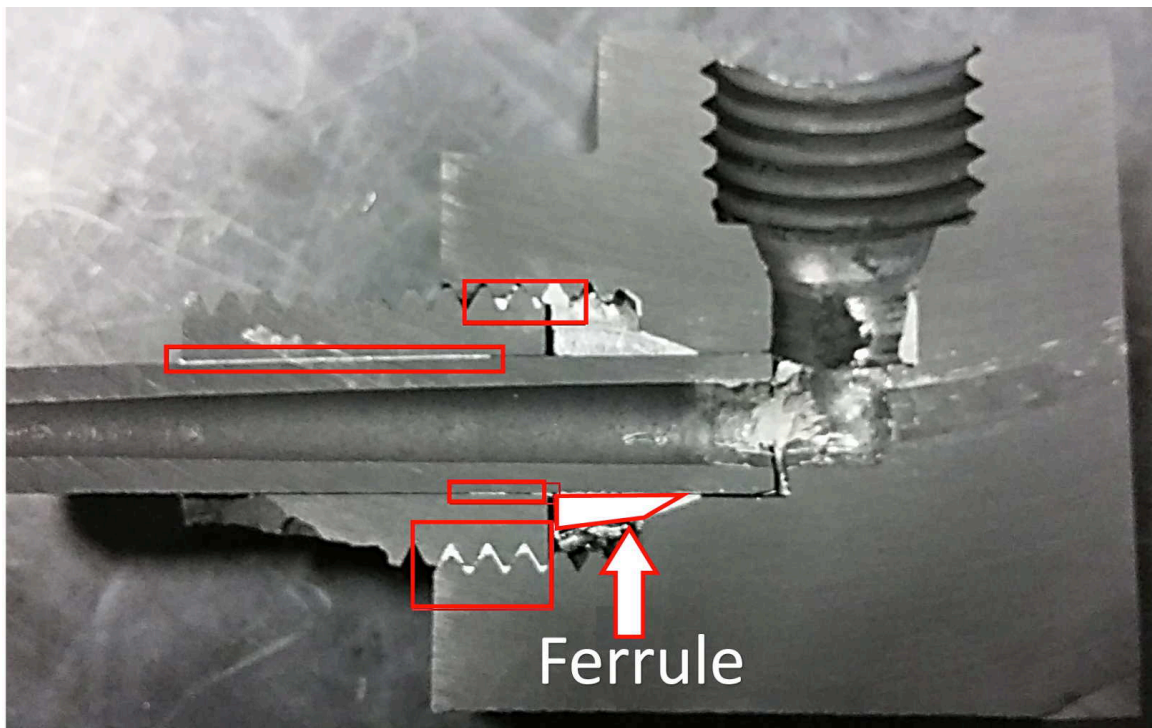


**Figure 49:** Sn leak at removable joint caused by inadequate ferrule compression

## 5.2 Shapal Hi-M Soft™

Once the Inconel pump was proven to perform well for the medium temperature case (below 600°C), focus shifted to enabling pumping at extreme temperatures, with the target of 1350°C. The Shapal pump was the primary material of interest because of its wide compatibility with molten metals as discussed previously. During initial experiments, the objective was to determine if, and for how long, the pump could operate without failure. Therefore, in these tests, a flow meter was not used, and the pump was run at very low rpm—only enough to maintain consistent flow (~150 rpm). Notably, a gear pump should, in theory, generate consistent flow at arbitrarily low rpm, but in reality, the fluid circulated inside the pump with no outlet flow for ~50 rpm. This is possible because there is clearance between to outer diameter of the gears and the pump cavity, in addition to the clearance between the flat gear face and the pump cavity. At low rpm, the pressure head after the pump outlet can overcome the reduced viscous forces which resist this internal circulation. Thus, at 150 rpm, instead of the predicted 0.6 gpm (see Chapter 3), only ~0.06 gpm flow was observed, which is only 10% of the theoretical flow rate. However, at 300 rpm, 0.25 gpm flow was observed, representing 20% of the theoretical flow rate. As rpm is increased the flow is expected to approach the theoretical maximum. Gear pumps are generally only rated for flow rates above ~500 rpm and up to ~3600 rpm, as noted in Appendix C.

### 5.2.1 *Initial Unsuccessful Tests*

Before the successful tests reported later in this chapter, issues including major Sn leaks, loss of temperature signals from electromagnetic interference, severe oxidation Sn

and C, external shaft support bearing failure, excessive shaft misalignment, and extreme wear occurred. Each of these issues is discussed in this section.

Although sealing issues were mostly solved during iterations with the medium temperature tests, the first high-temperature test resulted in a new type of leak: at the pump face seal. The issue here, as noted in the section on Pump Mounting in Chapter 3, was that TZM bolts were used to mount the pump, and these bolts had a slightly higher CTE than the Shapal which caused them to loosen as temperature increased. Because the bolts, and the ceramic materials clamped, were very stiff at room temperature, minimal deflection occurred during installation. Therefore, at peak temperature, the small (~0.2mm) growth mismatch was consumed at the face seal, and the seal leaked severely.

As this first experiment began at low temperature, the Sn circulated well initially, but after exceeding 1000°C the flow quickly stopped. An image from the aftermath of this experiment is given in Figure 50, which shows the entire volume of Sn leaked directly below this seal. This issue was readily solved once a supplier of tungsten bolts was identified, as W bolts have a CTE slightly less than Shapal. In this case, the bolts became even tighter as temperature increased, which kept the joint sealed. It is interesting to note that, although this Sn leaked fairly rapidly at ~1000°C, it did not deform or adhere to the stainless-steel table. Before this experiment, there was great concern about potential catastrophic effects of a high-temperature Sn leak. If the Sn did corrode through the table, it could eventually breach the oxygen barrier, which would expose the system to oxygen, whereas it would rapidly oxidize. As an added preventative measure, the bottom of the nitrogen chamber was covered with ceramic tiles and several layers of galvanized steel sheets to protect the outer oxygen barrier. However, even in the case of this rapid leak of

Sn above 1000°C, Sn did not breach the table because of two factors: the table was covered with graphite sheets which do not react with Sn and the large surface area dissipated the heat from the Sn quickly. Here, it is clear that the Sn froze quickly because it did not travel far from where it leaked. It froze especially quickly on the cold plate beneath the andalusite brick the pump was mounted to. Even here it did not appreciably react with the iron-based cold plate because it froze quickly and the plate had a thin carbon coating.



**Figure 50:** Leak caused by loosening of pump face seal bolts from thermal expansion

Another issue that occurred was control signal loss, which was primarily caused by interference from heater power inputs. Here, the heat was provided for experiments above 1000°C by an induction heater around the reservoir, as described in the Chapter 4. The working principle behind induction heating is that eddy currents are generated in a

workpiece by a strong, high-frequency electromagnetic field generated by the copper heater coil, which remains cool since it is actively water cooled. During several experiments, this field caused significant noise issues in thermocouple voltage. In addition to this influence, the coiled Kanthal resistance heaters caused similar issues, especially for thermocouples that were controlling the heaters, as they were nearly in contact with the element. In some cases, this interference was so strong that the NI 9213 thermocouple cards used in the NI cRIO 9074 controller, which were used to input the thermocouple reading into LabVIEW, completely stopped functioning. When this happened, all the thermocouple signals from a card (15 signals) output no data. This amounted to a loss of 1/3 of the input signals available from the control cart (Box B) shown in Figure 42—in these experiments, only ~20 thermocouples were used, and although they were spread across multiple cards, this signal loss essentially disabled safely heating the system.

As an immediate fix to continue experiments, handheld voltmeters were used to monitor temperature and control was done manually, as shown in Figure 51. After investigation, the issue was partially mitigated by separating the power and signal delivery wires as much as possible and having them cross perpendicular to each other where needed. Unfortunately, the signal and power wires entered the N<sub>2</sub> chamber through adjacent, parallel ports, so it was not possible to have optimal separation. With this improved setup, in most cases the induction heater only caused a small, repeatable (correctable) offset amounting to ~10 K in thermocouple voltage. It is expected that the main cause of this signal issue was a result of a ground loop between the thermocouple and the control system. Here, the thermocouples used were grounded; that is, the metal sheath was in electrical

contact with the thermocouple bead. Thus, the best solution would be to instead use ungrounded thermocouples.



**Figure 51:** Backup monitoring/control system to circumvent signal interference issues

Oxidation issues also occurred during some high-temperature tests. As indicated in the Medium Temperature Pumps section, this was evidenced by surfaces inside the N<sub>2</sub> chamber being covered in an oxide powder film and the oxygen sensor registering a higher oxygen content. Notably, the oxygen partial pressure was still relatively low ( $1 \times 10^{-13}$  atm) but this alone does not tell the complete story. Here, the leak rate was high, but the oxidation rate was sufficiently high to match the leak rate. The oxygen content was, however, useful to compare to previous experiments where the oxidation rate was low. Unlike the medium temperature tests, here, oxidation caused severe issues. Most notably, the graphite oxidized to a detectable level. Even bulk graphite components, such as the reservoir, had clearly larger pores near the external surfaces after several hours at

1350°C—pores initially less than 1 mm were as large as than 2-3 mm after oxidation, as shown in Figure 52.

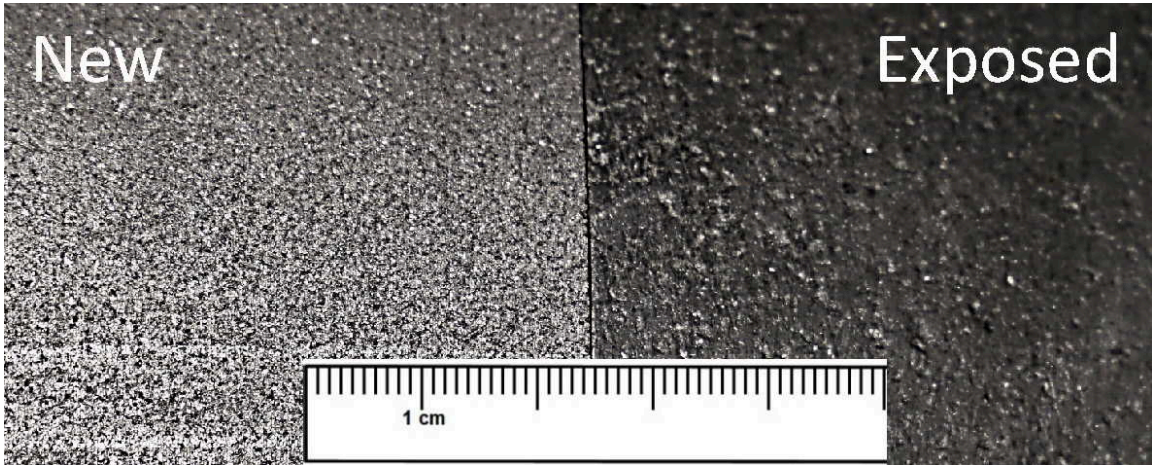


**Figure 52:** relative pore size of a new extruded graphite reservoir compared to one that was heated to 1350°C for ~10 hours in N<sub>2</sub> chamber when significant oxidation was observed.

Even more immediate issues were found with reaction bonded joints. Here, after being exposed to the same conditions, some pipes could easily be pulled out of the component they were initially bonded into because the bond was almost completely oxidized away. The reaction bonded joints were most susceptible to oxidation because of their relatively high porosity. Even after sealing, the external reaction bond surfaces were relatively porous because the sealer was applied internally—that is, from the inside out. Thus, pores from the outside could be unsealed if they did not fully penetrate the joint. Although in the cases where this happened there were no Sn leaks, it is likely that this oxidation would eventually cause leaks, possibly after a few days of exposure. As an example of a reaction bond that failed from oxidation, the tungsten mesh described in the Circulation Loop section of Experimental Setup completely separated from the graphite mount that constrained it, as shown in Figure 53. Here, the two graphite discs were reaction

bonded together, and this bond surface was the more prone to oxidation than the base material because of its high porosity and, thus, high surface area—especially because this bond was not sealed.

Notably, when C oxidizes in a low O<sub>2</sub> environment (below  $\sim 1 \times 10^{-4}$  atm), it predominately forms carbon monoxide (CO) [86]. In the low partial pressure O<sub>2</sub> environment inside the N<sub>2</sub> chamber, this CO, although unstable, may not react to form carbon dioxide (CO<sub>2</sub>) immediately. This effect was confirmed by placing a CO alarm inside the chamber, which consistently sounded once graphite components were heated above  $\sim 600^\circ\text{C}$ , indicating CO levels above  $70 \times 10^{-6}$  atm. Because the kinetics of the reaction  $2\text{CO} + \text{O}_2 \longrightarrow 2\text{CO}_2$  are accelerated with increasing temperature, the reaction is expected to occur where the temperature is high and O<sub>2</sub> is available to react. Near the heated graphite, the reaction was O<sub>2</sub> starved, so CO<sub>2</sub> was not favorable to be formed there. Instead, it is likely that CO formed CO<sub>2</sub> in the heated oxygen sensor, described in Chapter 4. This sensor is heated to  $750^\circ\text{C}$ , which is above the  $605^\circ\text{C}$  autoignition temperature of CO, so if oxygen is present, CO<sub>2</sub> may be formed. Thus, this reaction may suppress the reading of O<sub>2</sub> content inside the N<sub>2</sub> chamber. Here, the oxidation of C itself also reduces the reading on the sensor, but, in this case, it is possible that the actual O<sub>2</sub> content inside the N<sub>2</sub> chamber is not as low as measured.



**Figure 53:** Tungsten mesh un-bonded from graphite mount after the reaction bond suffered severe oxidation

Another critical issue related to the formation of SnO (which is the thermodynamically favorable oxide of Sn in this low oxygen environment) is that its melting point is 1080°C. This melting point is below the target temperature and thus it is possible that any oxide formed will actually melt during the experiment and could be entrained in the flow. This was particularly troublesome because the circulation loop was not quite isothermal. Therefore, during pre-heating, the SnO could melt in one part of the loop and freeze in another. This occurred during some experiments and resulted in a clog in the outlet piping. This issue was mitigated by reducing oxygen content and pre-heating the entire loop above the oxide melting temperature before pumping. The latter approach is limited to an experimental setup though, because in many applications it is necessary for the circulation loop to be far below the oxide melting temperature in some sections, and

above it in others. However, in a full-scale application, a system to filter the fluid or otherwise prevent clogs could more feasibly be implemented. It should be noted, however, that the primary safeguard against oxidation is the inert gas containment system, which should be properly sealed to drastically minimize leaks. Although a low leak rate was achieved with the experimental setup used in this study, it was not routinely operated with such effective sealing and major O<sub>2</sub> leaks likely existed during most tests. Nonetheless, this can be remedied with an improved setup, but was sufficient for the testing required herein.

Another major issue encountered in several experiments was the mechanical failure of the zirconia shaft bearing. Because of the system temperature, a very limited set of materials could be used for this bearing, and an even more limited set of commercially available bearings existed. As noted in the section on Pump Actuation in Chapter 3, after evaluating many options, the best commercially available ball bearing that was thermal expansion matched with the ZrO<sub>2</sub> pump shaft was made from partially stabilized ZrO<sub>2</sub>. Because of this, it underwent a phase transformation at 1173°C which, in addition to the stress from thermal misalignment, caused the inner race to fracture (see Figure 16) and subsequently caused the unsupported pump shaft to fail.

The ZrO<sub>2</sub> bearing setup was used during four tests (with a new bearing each time) and at best survived one test for 4 hours, where the pump was held at 1400°C—and the bearing was somewhat colder (~1100°C). During the other three tests, the bearing failed in less than 2 hours. Although several factors contributed, to unknown degrees, it is likely that because the bearing was colder than the pump (see Figure 10) its gradual temperature rise toward phase transformation temperature of 1173°C, in addition to the severe wear the bearing races experienced from misalignment, caused failure. An image of the pump

system after a test where the bearing failed is shown in Figure 54. Although the only failed component visible is the Shapal pump shaft, this shaft presumably failed after, and because, the support bearing failed. That is, zirconia bearing which was held in the yellow bearing mount on the right of the image failed, which allowed the zirconia shaft to move freely in the radial direction. This lack of constraint combined with the unbalance caused by misalignment caused the weakest point—the small, brittle Shapal shaft—to fracture. The fractured bearing is shown after disassembly in Figure 16.



**Figure 54:** Pump failure caused by phase transformation and misalignment induced stress in the  $ZrO_2$  bearing. The Shapal pump shaft has visibly failed, but this was preceded by failure of the bearing.

After repeated  $ZrO_2$  bearing failures, the decision was made to target a more robust bearing design. Therefore, although increased wear and friction was expected, a tungsten sleeve bearing, specifically designed to only constrain the shaft axially, and not angularly, was chosen. Surprisingly, instead of wear on the relatively soft W bearing, wear occurred

predominantly on the ZrO<sub>2</sub> shaft, because the shaft was not fully stabilized and thus was subject to phase transformation at the application temperature. The inner surface of the bearing was fully filleted so that, at small angles, the shaft was free to angularly deflect, as shown in Figure 17. This constraint is key because as the pump grows vertically, the ZrO<sub>2</sub> shaft deflects angularly, and the attempt to constrain this angle is largely why the stress on the original bearing was so great. This thin tungsten bearing is shown in the 3D models included in Chapter 3 and is also shown with the Shapal pump in its final configuration in Figure 59.

One more key challenge was the excessive wear rates experienced at Shapal-Shapal dynamic interfaces. Specifically, severe wear occurred at the Shapal sleeve bearing-shaft interfaces, the gear tooth meshing interface, and between the gears and the pump cavity, as shown in Figure 55. A major source of this wear was the third particle abrasion caused by abraded aluminum nitride particles grinding boron nitride, which exposed more aluminum nitride to be abraded. Although this cause can be resolved by using a harder, homogeneous ceramic, proper tribological design—which could enable very long life—necessitates improving other design factors as well [87].

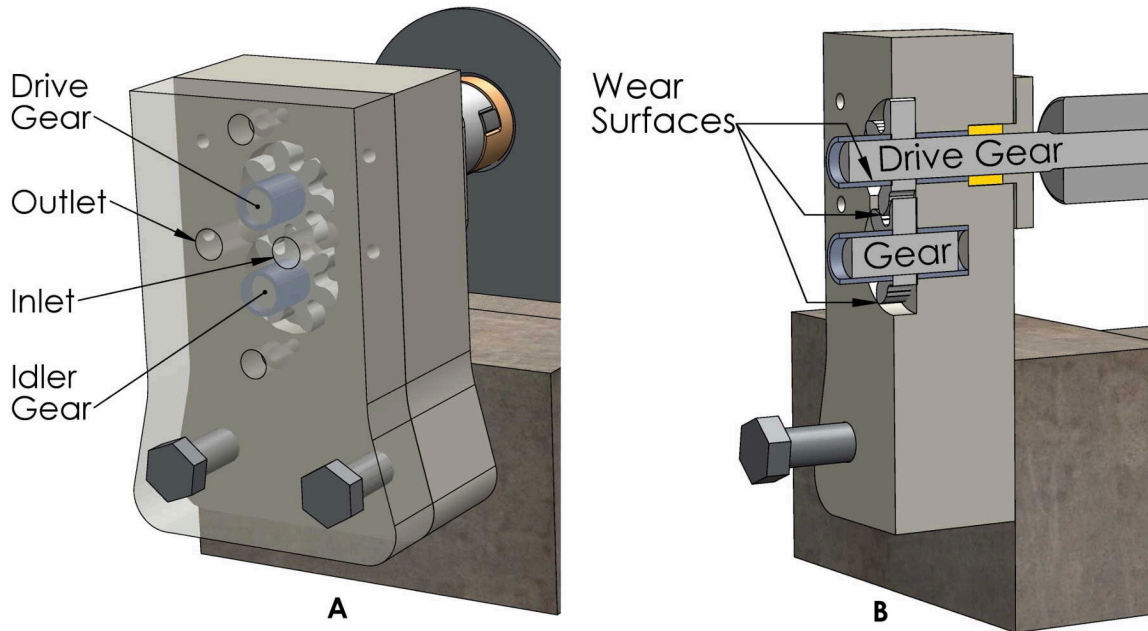


**Figure 55A:** Shapal pump internal geometry and **B:** Shapal wear surfaces

As sleeve bearings are employed to support the pump gears, they experience sliding wear. This wear rate is exacerbated if the bearing is not properly lubricated. During initial tests, the wear rate of the bearing/shaft interface was found to be in the range of severe wear (by definition in [87]), but after polishing these surfaces to a mirror finish, this wear rate was reduced by a factor of 30, and an acceptable amount of wear occurred during the 72-hour test reported in the next section. Before polishing, the wear rate was measured to be  $50 \mu\text{m}/\text{hour}$ , whereas after polishing the rate was reduced to  $1.8 \mu\text{m}/\text{hour}$ —where the distance measured was the diametric clearance between the shaft and bearing. As the machined surface roughness was reported to be  $0.4 \mu\text{m RMS}$ , the shafts were sanded starting from 400 grit to 2000 grit—which can reduce roughness to  $\sim 0.02 \mu\text{m RMS}$ .

In order to expedite this process, and achieve a uniform finish, the shafts were mounted in a small lathe and turned while sanding, as shown in Figure 56. In order to

protect the brittle ceramic shafts from the lathe jaws, a rubber set of rubber O-rings was used to minimize stress concentrations at the interface. Next, the shafts were polished in two steps, first with consumer grade Dremel polishing compound, and then with nanophase silica polishing compound. Here, the shafts were stationary and a Dremel polishing wheel was used to polish the shafts.

The target of these highly-polished surfaces was to enable full hydrodynamic film lubrication, where there is no direct contact between the bearing and shaft. This target was likely not achieved, because of the small size and limited precision of the pump components, although the wear rate was greatly reduced. Another factor which limits the ability to achieve full-film lubrication is the linear speed of the shaft surface, which in this experiment is very low. Here, the shaft speed was maintained below 400 rpm mainly out of concern of brittle failure of this prototype pump, but in a full-scale application, both the shaft diameter and rpm would increase.

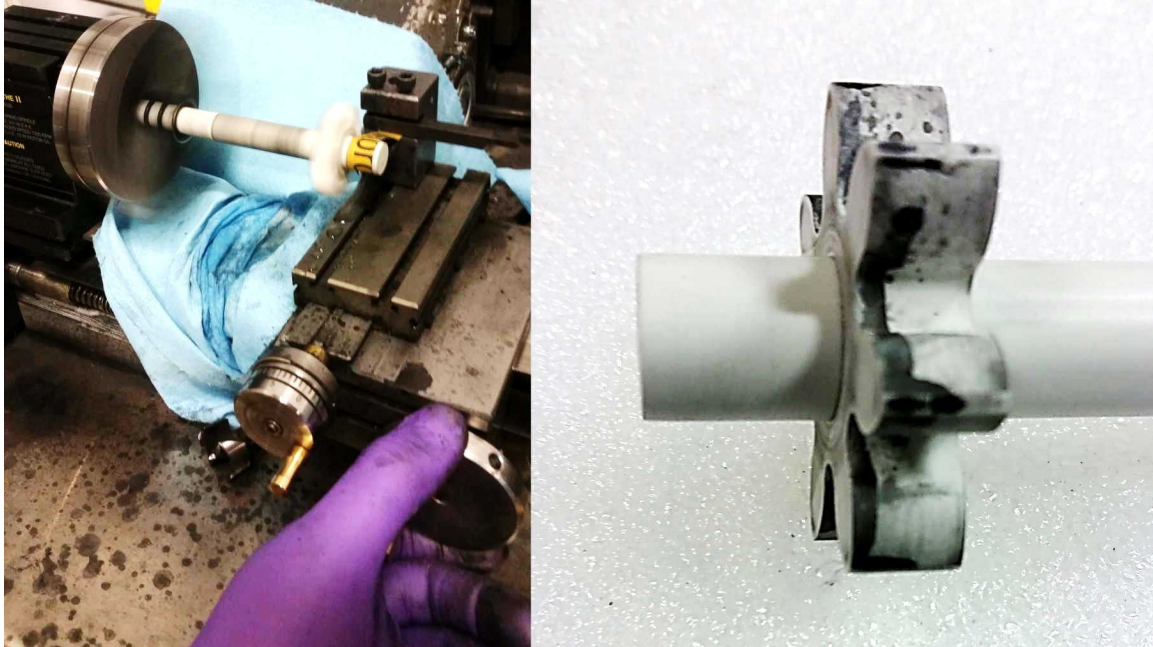


**Figure 56:** Sanding pump shafts to reduce wear rate by minimizing surface roughness

In addition to bearing wear, the gear teeth also experienced severe wear during all tests, even after polishing. The causes here are similar, however to achieve a very low wear rate, elastohydrodynamic lubrication was needed [87]. If this regime is met, which requires precise, polished gears and sufficient rpm, the gear teeth do not contact directly. Instead, they remain separated by a *very* thin layer of liquid, which requires a finite time to deform when driven by a finite force (see the section on Wear Resistance in Discussion and Future Work). Polishing did not solve this problem, and the pump was not tested above 500 rpm, which might have enabled a film to develop. This tooth wear issue is fundamental to the Shapal pump material, and for that reason, an alternate material should be used to achieve much longer life—on the order of tens of thousands of hours. Alternative design options are included in the section on Discussion and Future Work, later in this chapter.

### 5.2.2 *Primary Successful Tests*

Among the many tests conducted with the Shapal pump, the most notable are the highest temperature test and the longest test. The test that achieved the highest pump temperature, nearly 1500°C, unfortunately did not have the temperature data recorded because of an error with the LabVIEW VI, but was nonetheless noted by those conducting the experiment; Therefore, data from the test which achieved the second highest temperature, 1415°C, is reported. Video and pictures were recorded, however, and an image is included in Figure 57. Because Sn is highly reflective, the fluid stream enable a view of the surface of the reservoir it was flowing into. Here, the small (~1mm), horizontal ripples visible on the stream are actually reflections of the ripples on the surface of the reservoir—like those that from when a rock is thrown in a lake.

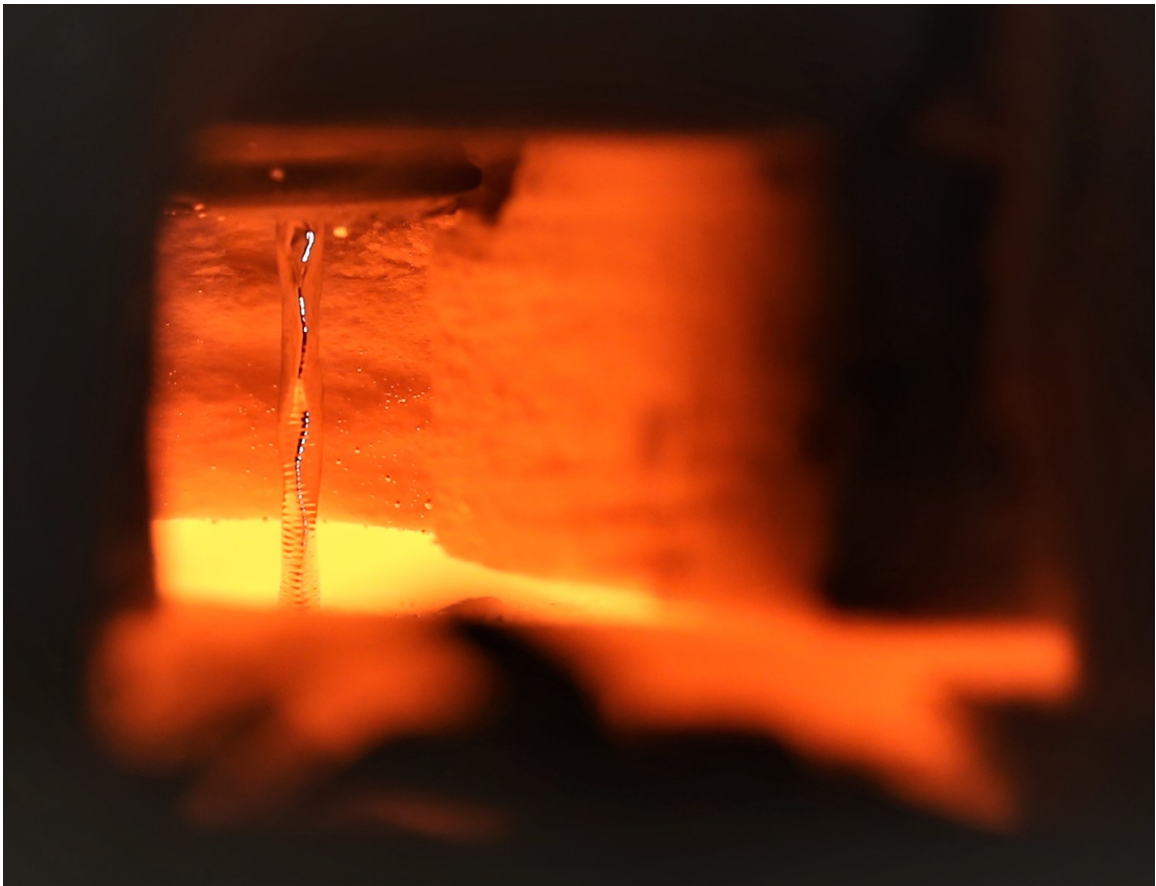


**Figure 57:** Image from pump test which reached 1490°C

In the second hottest test, which occurred when the ZrO<sub>2</sub> bearing was still used, the pump operated continuously for 2 hours above 1100°C, spending nearly 45 minutes above 1350°C, as shown in Figure 58. The saw tooth shape visible during the first hour reported is a result of the varied pump throttle, shown in gray. The pump was cycled on and off here because no outlet flow was observed, which turned out to be the result of a partial Sn freeze near the exit of the circulation loop. After the loop was sufficiently preheated, flow was visible as shown on an overlay in Figure 58—here, the pump was run at constant speed and a smooth temperature rise was observed after the first hour.

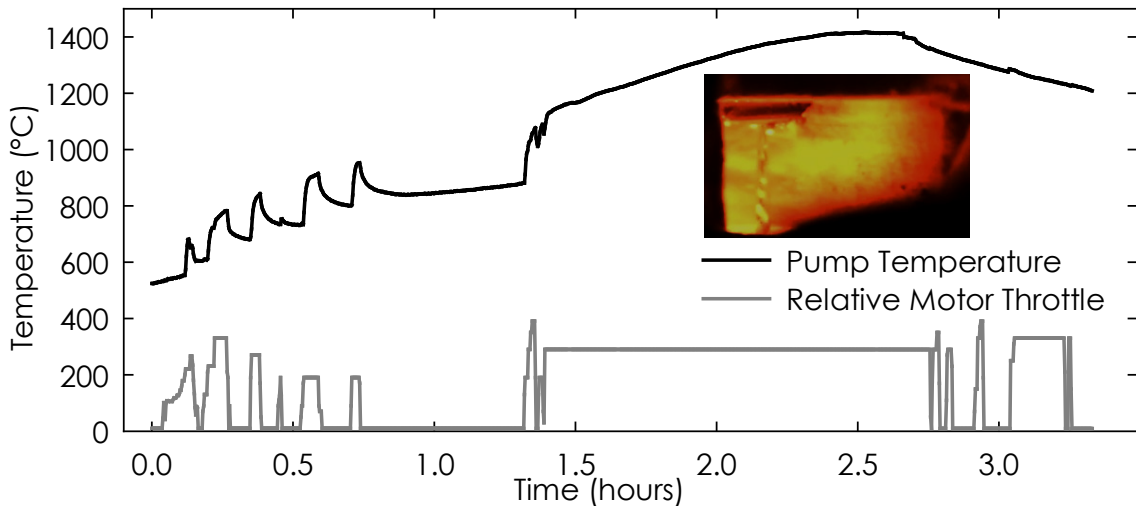


**Figure 58:** Pump temperature and throttle, during test which reached 1415°C

As noted in the previous section on Initial Unsuccessful Tests, this test ended after only two hours of continuous pumping when the ZrO<sub>2</sub> ball bearing failed, leading the unsupported Shapal pump shaft to fail, and thus the pump stopped rotating. An image of the pump shaft after this test is shown in Figure 54. Because of the sensitivity of this bearing, a more robust tungsten sleeve bearing was employed in the longest test, as noted in the previous section. Further, even in this short test, noticeable wear was seen on the all

the Shapal-Shapal dynamic surfaces. This wear rate was mitigated on the cylindrical surfaces in future tests where they were highly polished (see Initial Unsuccessful Tests), but the gear teeth wear rate remained severe.



**Figure 59:** Pump system in configuration used for 72 hour test

After the previous tests, it was clear that a different pump material was needed to achieve long (~10,000 hours) life, but in order to confirm if short term failure modes were resolved, and to quantify flow rate, a final test was conducted. In this, the longest test, the system was in its final configuration, which included the visual flow meter, polished gears, and the tungsten sleeve bearing, as shown in Figure 59. Here, the pump operated for 72 hours without failure, although noticeable degradation in performance was observed after 55 hours. During this test, the pump temperature was maintained between 1120-1240°C.

This temperature limit was a result of limited heater power and is not a fundamental bound on the pump or other system components. For example, earlier tests without the flow meter were conducted at temperatures as high as 1500 °C without failure. One of the major sources of heat loss was the flowmeter viewport which limited the steady state temperature of the system. A view from this port, which was necessary to determine flow rate, is shown as an overlay on Figure 60 and with a view of the experiment chamber in Figure 45. Also, methods to increase the heat input from the induction heater are discussed in the section on Heating Equipment in Experimental Setup.

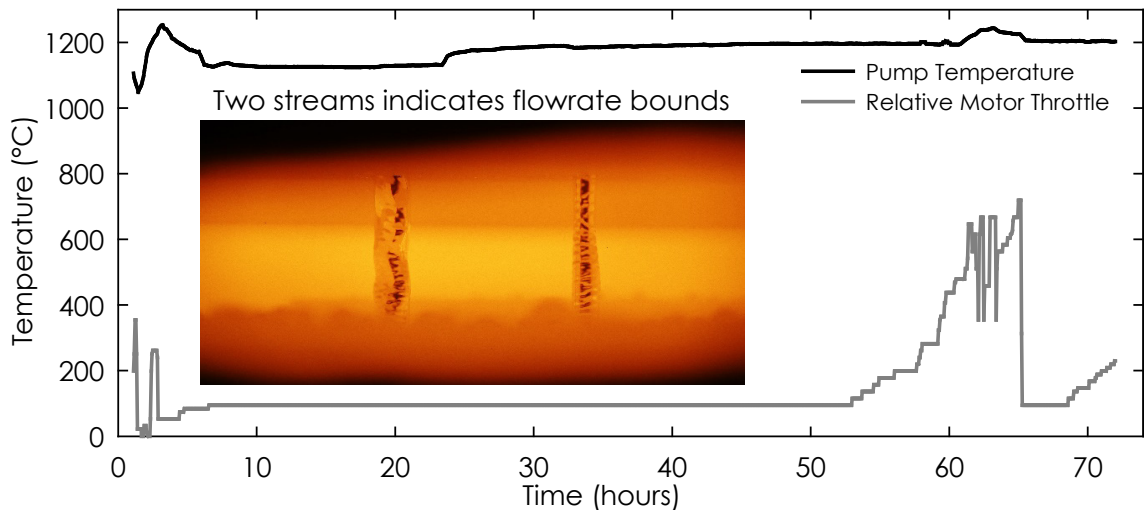


**Figure 60:** Pump temperature and throttle, during 72 hours of pumping near 1200°C

As indicated by the two-outlet flow shown overlaid on Figure 60, a flow rate between 24-108 g/s was maintained for the first 60 hours of the test. This quantitative measurement is based on the calibration process explained in the section on the Flow Meter in Experimental Setup. The initial spike in temperature was driven by auxiliary pre-heaters which have a very short life above 1000°C. As a result, they failed and the remaining heat was supplied by the induction furnace loop around the reservoir (see Figure 36) and

subsequently spread throughout the system via the Sn flow. Also, convective cooling of the ambient gas inside the inert containment system was reduced after 25 hours (by turning off one of the two fan coolers), which enabled a slight temperature increase, visible in Figure 60, to above 1200°C.

After 55 hours, a decrease in flow rate occurred and the rotational speed of the pump was temporarily increased to maintain the target flow rate, shown in gray in Figure 60. An image of the second outlet dripping, which indicated decreased flow rate, is included in Figure 61. However, over the next 10 hours, maintaining the target flow rate required a steady increase of the motor rpm. After 65 hours, in order to avoid the risk of breaking the pump at higher rpm (which was, at the time, 300 rpm), the decision was made to complete the remainder of the test below the measurable threshold. This self-imposed low rpm was not based on experimental issues and was mainly followed because the cause of the flow rate decrease was unknown at the time. Even with this flow rate limitation removed, the throttle had to be steadily increased just to maintain steady flow out of the first outlet. The pump continued to operate, and the test was stopped after 72 hours for inspection.

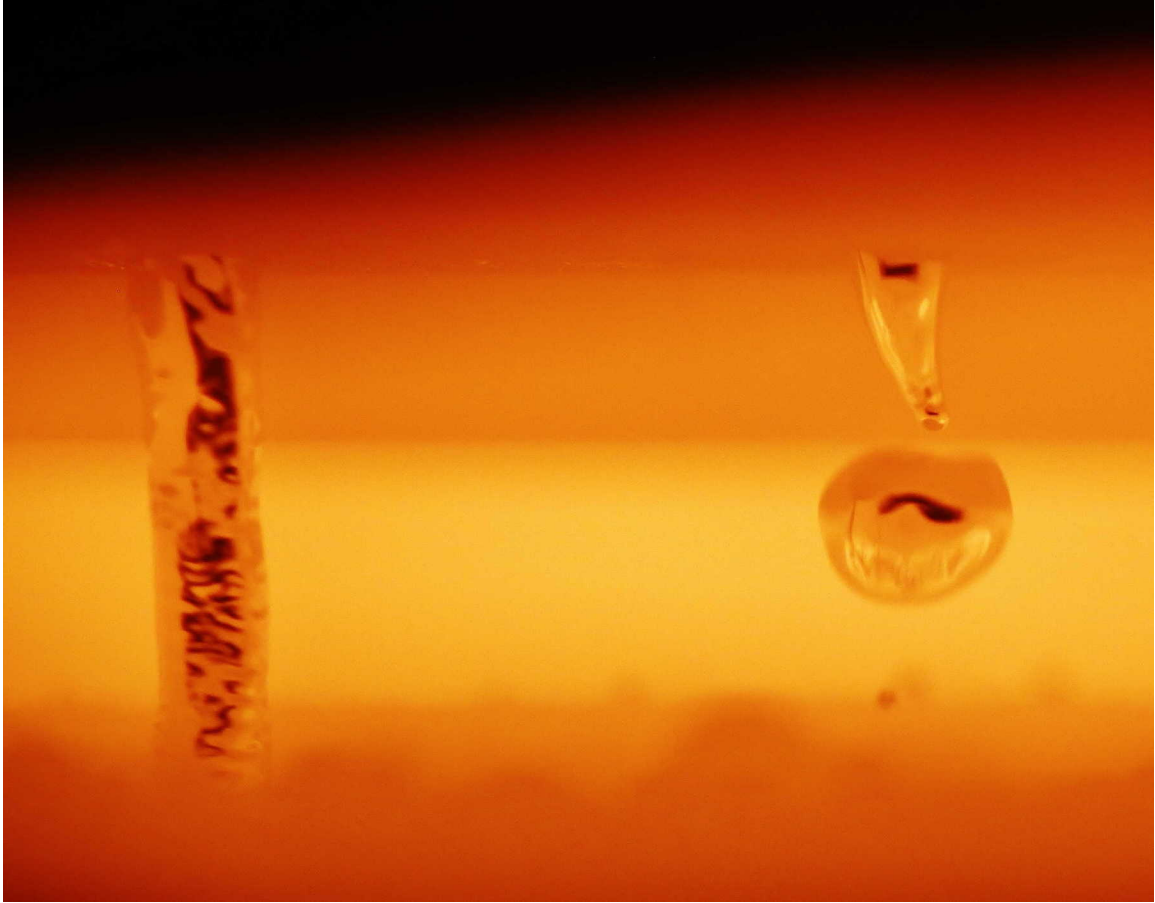


**Figure 61:** Image depicting flow decrease (dripping) out of second outlet after 55 hours

There was no mechanical failure of any components during the test, nor was there failure from/during cooling. The pump gear teeth, however, experienced significant wear, although the sleeve bearings did not wear excessively—the bearings wore at a rate of 1.8  $\mu\text{m}/\text{hour}$ , which is expected to enable for pump life of  $\sim 500$  hours based on the accumulated wear during previous pump failure. It was believed that this wear was responsible for the reduced flow rate after 55 hours; it was quite severe, as shown in Figure 62. The majority of the apparent wear was on the drive gear and, as shown in the zoomed view, was a result of the drive gear continually colliding with the idler gear—approximately one million times during the test. Although this type of wear does not always

reduce the performance of a pump—in fact, metal gear pumps often use polymer idler gears to enable this wear which can result in lower peak stress—in this case, the brittle ceramic gear teeth also increased clearance on the radial tips, as well as their flat faces. Compared to a new gear, the outer diameter of these gears was reduced by nearly 500  $\mu\text{m}$ , as noted in Table 4.

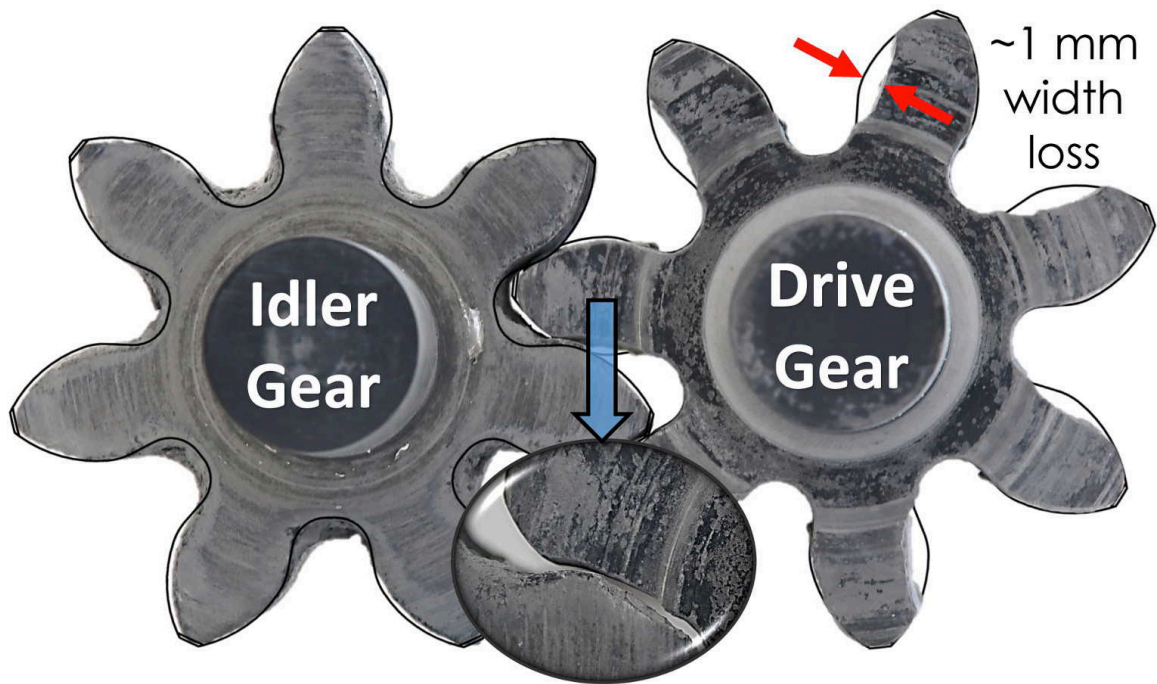


**Figure 62:** Wear on Shapal gear teeth after 72 hours of continuous pumping

Based on this severe wear, an alternative material is recommended for future extreme temperature liquid metal mechanical pumps, or at least a different material for dynamic components. Nevertheless, an all ceramic pump has been designed, fabricated, and successfully tested which has demonstrated the highest temperature continuous pumping of any fluid ever achieved. Notably, although some gasses have been transported at higher temperatures (*e.g.*, gas turbines), they are pumped/compressed at much lower temperature. Here, Sn has been pumped directly at temperatures in excess of 1400°C

without failure and a pathway to realizing the long life required in industrial settings is included in the section on Discussion and Future Work later in this chapter.

**Table 4:** Wear amount and rates for gears after 72 hours (~1,000,000 rev.). While most wear occurred at the gear teeth, the wear most detrimental to performance occurred at the radial gear tips—because this allowed fluid to leak around the teeth. This surface only contacts the pump body as the shaft wears; thus, minimizing the shaft/bearing wear rate is key.

<b>Dimension</b>	<b>Baseline</b>	<b>Drive</b>	<b>Drive loss</b>	<b>Idler</b>	<b>Idler loss</b>	<b>Unit</b>
Tooth width	6.78	5.82	0.97	6.68	0.10	mm
Gear Thickness	8.89	8.66	0.23	8.84	0.05	mm
Gear Diameter (3 pt)	36.42	36.20	0.23	36.07	0.36	mm
Shaft Diameter	12.70	12.59	0.11	12.54	0.16	mm
Gear Wear Coefficient			2.85E-02		5.41E-03	unitless
Shaft Wear Coefficient			3.68E-02		4.41E-02	unitless

### 5.3 Tungsten

Thus far, the tungsten pump has not been tested extensively. It has, however, performed well at 650°C without leaks, mechanical failure, or even noticeable wear. It has run for eight hours at a speed above 400 rpm and flow rate near 100 g/s. There was no evidence of issues with this pump and it is expected to perform well at 1350°C, and even much higher temperatures. It is important to note, though, that this pump is chemically limited to use with molten Sn (or the cost prohibitive Ga and In), unlike the Shapal pump.

One interesting aspect of the tungsten pump is its extreme density—it is six times denser than the Shapal pump. Although in this small-scale application this was not a major issue, if a pump was designed for several hundred gpm flow rate, its fabrication should include lightweighting. Here, for example, the pump body should be a shell (which would likely be hot pressed into nearly to final shape from W particles) rather than the bulk tungsten block with minimal machining used in these experiments. Even at this small scale,

effects of heavy weight were apparent. The tungsten jaw coupler had a mass of 750 g, and was thus too heavy to safely use with the Shapal pump shaft; however, a shelled design can be a fifth the mass, at 150 g, while retaining high strength. For reference, the Shapal coupler which has the same geometry as the heavy tungsten coupler, had a mass of only 125 g. An example of this lightweighting process is shown in Figure 63.

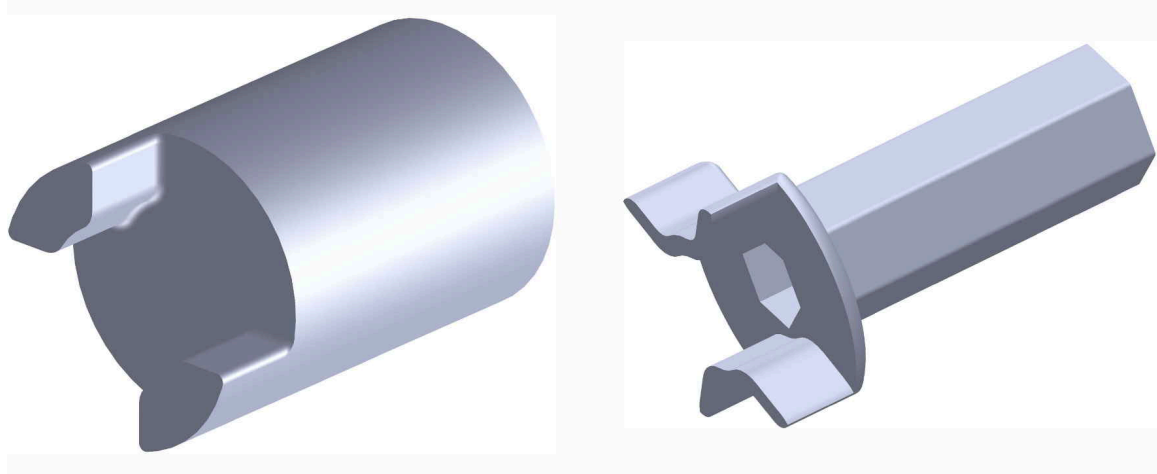


**Figure 63:** Example of lightweighting of tungsten components to reduce cost and weight induced stress

## 5.4 Discussion and Future Work

The clearest takeaway from these results is that *it is possible* to continuously circulate liquid metals at temperatures well above 1000°C, even in an isothermal loop. The primary limitations reached in these experiments are not fundamental limits and can be greatly exceeded with an improved design. Three main design areas remain to be improved to enable operation of a HTF flexible, extreme temperature mechanical pump with high life and reliability: wear resistance, shaft actuation, and fluid compatibility.

### 5.4.1 Wear Resistance

The first step to reducing wear rate, as mentioned previously, is exchanging Shapal for a more wear resistant material. For example,  $\text{Al}_2\text{O}_3$ ,  $\text{ZrO}_2$ ,  $\text{Si}_3\text{N}_4$ , and  $\text{SiC}$  are homogeneous, highly chemically compatible materials with high hardness. Among these, an alloy of alumina ( $\text{Al}_2\text{O}_3$ ) known as zirconia toughened alumina (ZTA), is an attractive candidate. Here, the high hardness (1650 HV  $\text{kg mm}^{-2}$ ), high fracture toughness (7.3 MPa  $\text{m}^{0.5}$ ), and high-temperature limit of mechanical stability (1500°C) of ZTA can prevent failure and minimize wear rate.

Although material hardness is key to wear rate in this low-speed sliding wear regime, Shapal's weakness is not only due to its relatively low Vickers hardness of 390  $\text{kg mm}^{-2}$  (compared to other technical ceramics above 1500  $\text{kg mm}^{-2}$ ). Shapal's key flaw lies in what makes it machinable: its nonhomogeneous lamellar  $\text{AlN}/\text{BN}$  crystal structure. This structure causes it to erode in small ( $\sim 5 \mu\text{m}$ ) particles of  $\text{AlN}$  and  $\text{BN}$ . These particles remain entrained in the Sn flow, at particularly high concentrations in the sleeve bearing cavities. This results in third particle abrasion caused by abraded aluminum nitride particles grinding boron nitride, which exposes more aluminum nitride to be abraded. The relatively large particle size also causes the surface roughness to increase greatly at the onset of wear. Similarly, in the case of the gear teeth, where the harder  $\text{AlN}$  particles are exposed, they abrade the  $\text{BN}$  particles on the opposite surface, and vice versa. While this cause can be resolved by using a harder, homogeneous ceramic, several other factors need to be considered for proper tribological design—which can enable very long pump life on the order of years.

Therefore, although the life of the pump can be extended to perhaps the order of thousands of hours by employing hard, homogeneous ceramics, in order to enable pump

life on the order of several years, it will likely be necessary to achieve a different regime of lubrication. The ideal regime is that of full hydrodynamic film for the sleeve bearings and elastohydrodynamic lubrication (EHL) for the gear teeth—these regimes are discussed in detail below. It should be noted that although hydrodynamic lubrication would be beneficial for the gear teeth as well, it is infeasible to achieve because the gear teeth are counterformal—that is, they are not closely matched in shape where they contact. In the case of EHL and hydrodynamic lubrication, no dynamic components directly contact a solid at a moving surface [87]. Thus, in this case, wear is minimal. The conditions required to achieve these flow regimes are related, but not identical.

In order to design a sleeve bearing to operate under the conditions of full hydrodynamic film lubrication, viscous forces must overcome the bulk mechanical forces on a shaft. That is, the minimum fluid film thickness must be greater than the height of asperities on either surface. Asperities are the areas of a surface that are above the mean surface height—analogueous to mountain peaks. Often, the force that must be overcome is predominately from gravity, although in the case of this ceramic pump the dominant force was a reaction to the off-axis force at the interface of the two gears, which was caused by the applied torque. This is because the gears in this system are small and have low density. It is desirable to minimize this reaction force, which was a direct consequence of the pressure drop throughout the circulation loop and the pump efficiency. It is important to note, however, that other pump designs utilize symmetry to avoid this issue altogether—*e.g.*, centrifugal pumps exert (nearly) axially symmetric force on the fluid, so the shaft is balanced.

Another controllable design parameter is surface roughness. The smoother the two conformal surfaces are (in this case the bearing and shaft), the lower the required film thickness to prevent contact. Although most surfaces can be sanded and polished to a smooth finish, the grain size can put a lower limit on surface roughness after initial wear. Thus, lower grain size can result in lower wear rates [88]. Sliding velocity is an additional factor that determines the lubrication regime. Here, increased velocity increases the viscous forces present and results in a larger minimum film thickness. Lastly, decreasing the radial bearing clearance can also shift the system toward full film lubrication, although this reduction is limited to about 10x the surface roughness of the shaft/bearing.

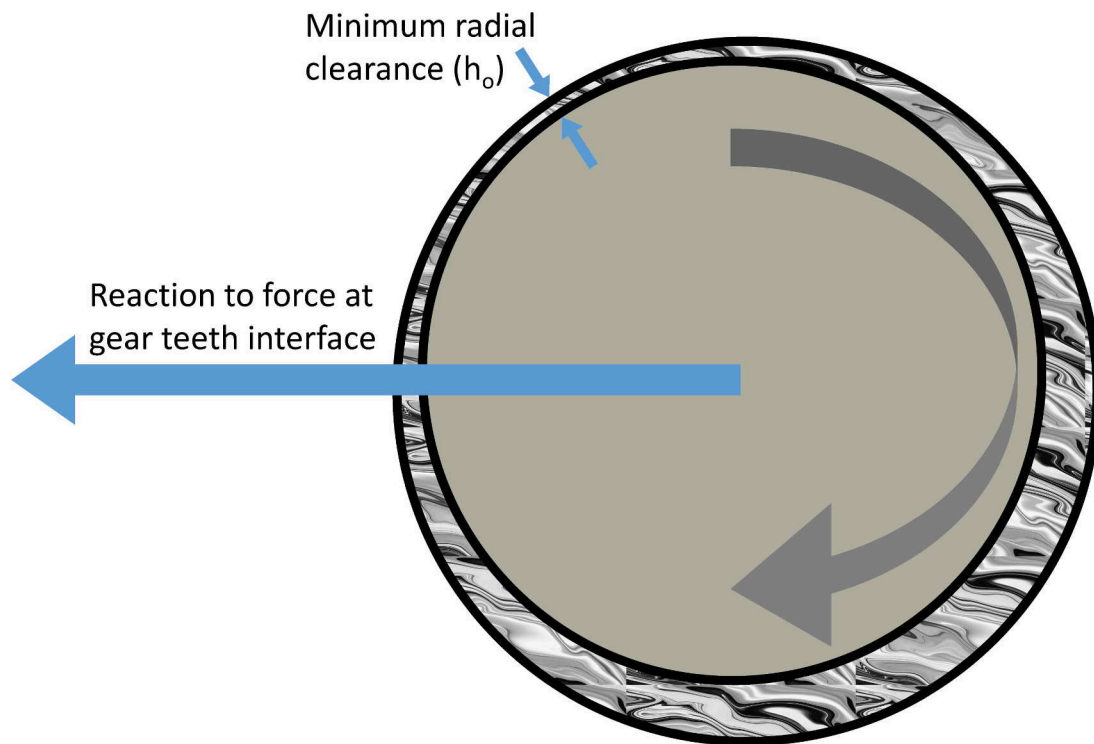


**Figure 64:** Diagram of sleeve bearing lubrication

These competing factors are all variables in a simplified version of Reynolds equation (see Equation 10), which is used to describe the pressure distribution within a

hydrodynamic lubricant film. It is simplified, in this case, by assuming incompressible, constant viscosity flow. Reynolds equation is derived from the general Navier-Stokes equations, which describe the motion of viscous fluids, based on the assumptions of laminar, viscosity driven flow flow—where the fluid film is thin relative to other dimensions. Although derived for a flat plate, if the radial clearance of a sleeve bearing is small relative to the diameter, the gap is relatively planar. Here, the pressure drop is a function of dynamic viscosity ( $\mu$ ), sliding velocity ( $U$ ), and the difference between average radial clearance ( $h$ ) and minimum radial clearance ( $h_o$ ). A diagram indicating the shaft eccentricity and attitude angle is given in Figure 64. Attitude angle is the angle between the net applied force and the minimum radial clearance ( $h_o$ ), which is a function of the fluid properties and shaft speed because it is caused by the lubricant pressure pushing the shaft to the lower pressure region (here, the top of the cavity).

$$\frac{\partial p}{\partial x} = \frac{-6\mu U(h - h_o)}{h^3} \quad (10)$$

After integrating Equation 10 and applying the periodic boundary condition, the effect of the parameters discussed above can be summed up as shown in Equation 11: the load carrying capacity ( $W$ ) of a shaft in full hydrodynamic lubrication is a function of dynamic viscosity ( $\mu$ ), sliding velocity ( $U$ ), shaft radius ( $R$ ), average radial clearance ( $h$ ), and the fitting constant  $S$ . Here,  $S$  is the Sommerfeld number, and is related to the length of a shaft and its eccentricity—it can be determined numerically or experimentally. Although this equation is useful, the parameter  $W$  can be difficult to determine and is a function of the circulation loop's resistance to flow, pump efficiency, and flow rate.

Therefore, although an allowable load can be predicted, it cannot be easily compared with an expected load. In this case, it is necessary to design for an allowable load in excess of the maximum predicted load, including a factor for uncertainty.

$$W = S\mu U \left( \frac{R^2}{h^2} \right) \quad (11)$$

It is important to note that there are other approaches to force full film lubrication, which involve varying methods of forcing fluid into the highest pressure angular location on the shaft. For example, large rotating machinery, such as power generation gas turbines, are often lifted by pumping oil to this location (in this case nearly at the 6 o'clock position because of the immense weight of the rotor). However, this approach is not practical for a pump, because it alone requires a separate pump.

On the other hand, there are alternate methods to lift a pump shaft that take advantage of the pressure difference created by the pump itself. Here, a small fluid port can be made connecting the high-pressure side of the pump to the high-pressure angular location on the shaft, as shown in . In this way, a portion of the fluid that would exit the pump outlet is instead rerouted to lubricate the bearing. This approach is technically possible to apply to a ceramic gear pump, although the channel paths required are complex, and not straight. Therefore, this approach would require machining several paths, and then partially filling them via reaction bond.

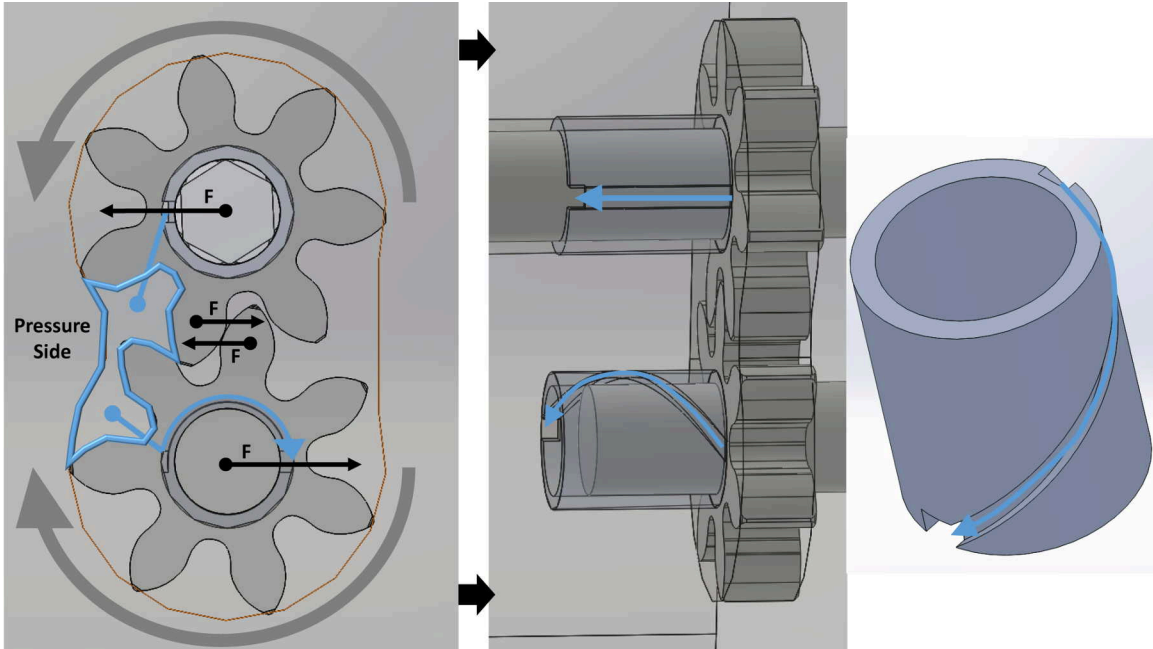


**Figure 65:** Actively self-lubricated sleeve bearing. Here, the concept is to connect the pressure side of the pump to the angular position on the bearing/shaft interface with the highest pressure. This pressure is caused by a reaction force from the gear meshing, as shown. The lubricant is routed to the back of the bearing to maximize the leak path back out of the bearing. Thus, the (top) drive gear is pushed to the left, so it needs lubricant ( $S_n$ ) on this side. Because this is the pressure side of the pump, a straight path connects the pressure cavity to the bearing. On the other hand, the (bottom) idler gear is pushed to the right, so a helical path is required to lubricate it—this bearing is detailed on the far right of this figure.

Elastohydrodynamic lubrication (EHL) has similar, but relaxed, requirements when compared to full hydrodynamic film. Because of the high pressure at the line of contact between two gears, the viscosity of the lubricant (in this case  $S_n$ ) can increase greatly at this location in space and time. Although pressure dependent viscosity of  $S_n$  is not well known, it has been proven in general that viscosity can be scaled with melting temperature; therefore, because the melting temperature of most materials (including liquid metals) increases with pressure, so too does the viscosity [89]. In the case of mineral oil based lubricants, viscosity can increase by a factor of 20,000 or more at the contact between two counterformal metals [87]. This is possible because the pressure over the minuscule contact

area is only limited by the elastic modulus of the material. In the case of ceramics, the elastic modulus is even higher than metals, so EHL lubrication is feasible to achieve, but only with sufficiently short contact time (high rpm) and sufficiently smooth surfaces.

Quantitative prediction of the precise values required to achieve EHL can only be solved via numerical methods, or using experimentally based empirical models, and then only if sufficient fluid properties are available. Therefore, in this case, the design considerations are very similar to those for full hydrodynamic film lubrication, focusing on low roughness, high hardness, and high speed. If, in future work, more parameters are open to modification, including shaft diameter, rpm, and even pump type—in addition to alternate materials—ideal wear regimes may be achieved and could have a dramatic effect on the pump lifetime. For example, centrifugal pumps have minimal shaft load, so a thicker fluid film would develop than in a gear pump with the same linear shaft speed and roughness. Similarly, this type of pump removes the continuously contacting of gear teeth, thereby side-stepping the issue of EHL at this interface altogether. Centrifugal pumps, on the other hand, generate an axial force, so a thrust bearing would be required, or at least the design should accommodate this thrust. Although some applications may be better suited for a gear pump to achieve reliable flow rates or high pressure, many industrial applications of this technology will likely favor a centrifugal pump or another velocity type pump.

An alternative gear geometry can also reduce the wear rate of a gear pump. Specifically, helical gears enable continuous meshing of gear teeth and thus a smooth transition between teeth. In order to counteract the axial force developed from helical gears, a double helix, or herringbone, gear is often used. Here, the helix is reflected so that each

part cancels the other's axial force. In this way, the need for a thrust bearing is avoided. An example of the pump geometry used in this work converted to a herringbone design is included in Figure 66. While helical gears may reduce wear rate, their fabrication is significantly more complex, and may be cost prohibitive if made from hard ceramics, which require diamond grinding of all critical dimensioned surfaces as noted in Chapter 3.

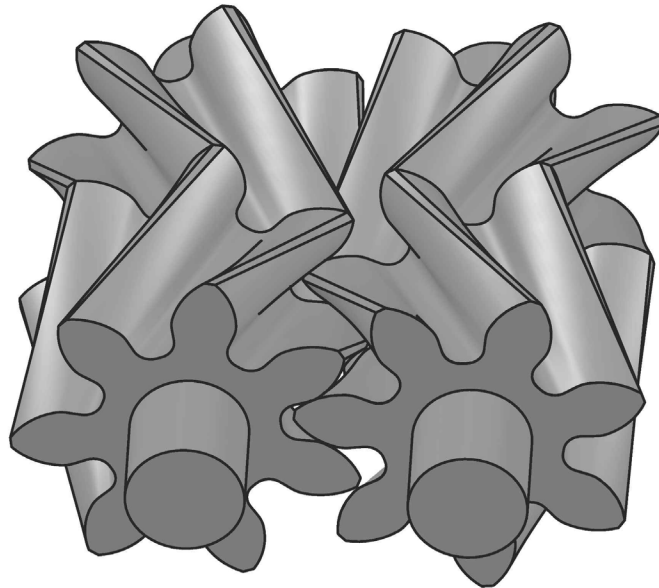


**Figure 66:** Continuous meshing of two herringbone gears

Achieving full film lubrication, or at the very least very fine polished surfaces, is especially critical for ceramics, because of their intolerance for plastic flow. Unlike metals, which may experience plastic deformation when asperities (high spots) contact, ceramics typically experience brittle fracture [87]. This fracture is usually intergranular, except in the case of extreme wear, and therefore the surface roughness of a ceramic will increase up to the mean grain size of the bulk material, given enough time. So, it is ideal to prevent asperity contact altogether, or at least reduce it enough so that once the highest asperities

have fractured away, the bulk of the original conformal surfaces are still smooth. In addition to solving the severe wear challenges encountered, the shaft setup should also be improved in a future design, and approaches to this design are included in the next section.

#### *5.4.2 Shaft Actuation*

The second main design feature to improve is the shaft setup. There are two main features to improve: the misalignment of the pump should be reduced and the tolerance to misalignment should be increased. Here, instead of offsetting the alignment to match only at a specific temperature, the pump could be mounted in such a way that the total displacement decreases. One approach could be to install the pump upside down from its previous orientation so that the expansion of the pump and its base partially cancel each other. Here, the pump would expand downward, while the base would expand upward. In practice, a less extreme change will be needed in order to maintain adequate thermal isolation and mechanical linkages. For example, the pump body could be mounted at the same vertical position that the driven shaft exits so that the pump growth has no effect on alignment—that is, the shaft position would not be effected by expansion of the pump. A possible arrangement of this mounting system is shown in Figure 67.

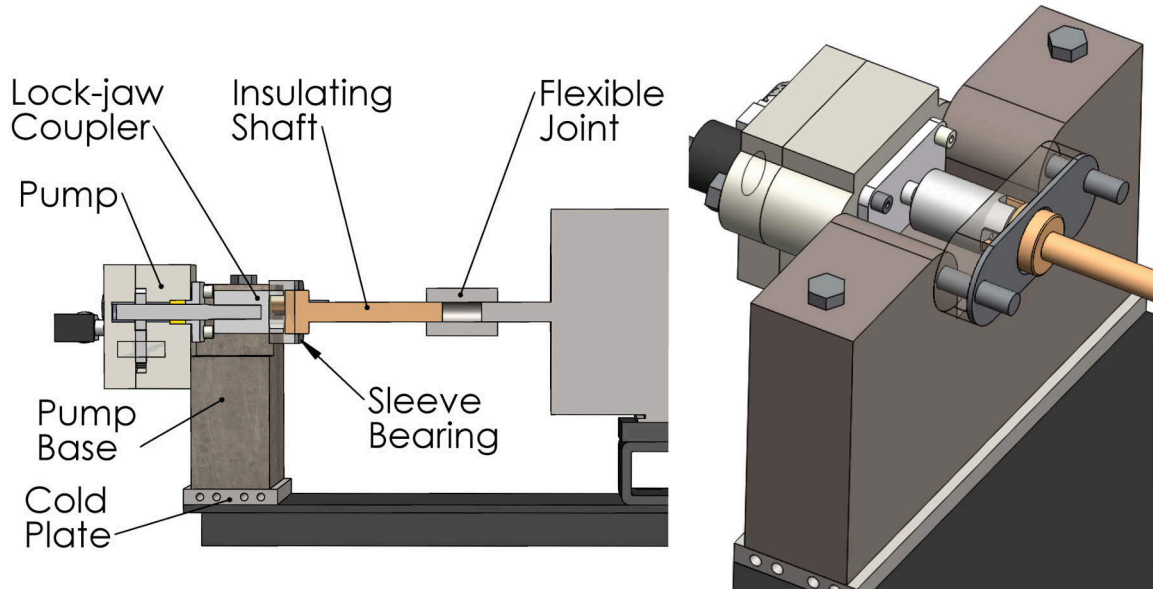


**Figure 67:** Alternate pump mount design where the pump is bolted at the same vertical height as the drive gear, so that it expands about this plane, and thus remains in perfect alignment with the external bearing—independent of temperature.

There are two sets of alignment challenges. The first is between the pump/mount/bearing and the motor, and this misalignment can be tolerated by various flexible couplers. The metal helical coupler used on the cold side in these experiments worked well, and that side of the shaft setup does not need revision. On the hot side, however, replacement of the jaw coupler interface is recommended. These jaws rely on a soft intermediate “spider” in order to accommodate misalignment. Unfortunately, at these temperatures, a material hasn’t been identified that has elastic shock absorbing properties like rubber does at room temperature. So, for these tests, a TZM spider has been used, which is only slightly better (softer) than a ceramic. Instead of this coupler type, a universal type joint or helical coupler is recommended. Here, a tungsten helical coupler with similar geometry to the cold side metal coupler could be used. If this design were employed, the hot (pump) side of this coupler would need to be constrained by a relatively wide (~4 cm)

sleeve bearing. A possible arrangement of this helical-helical shaft actuation system is shown in Figure 68.

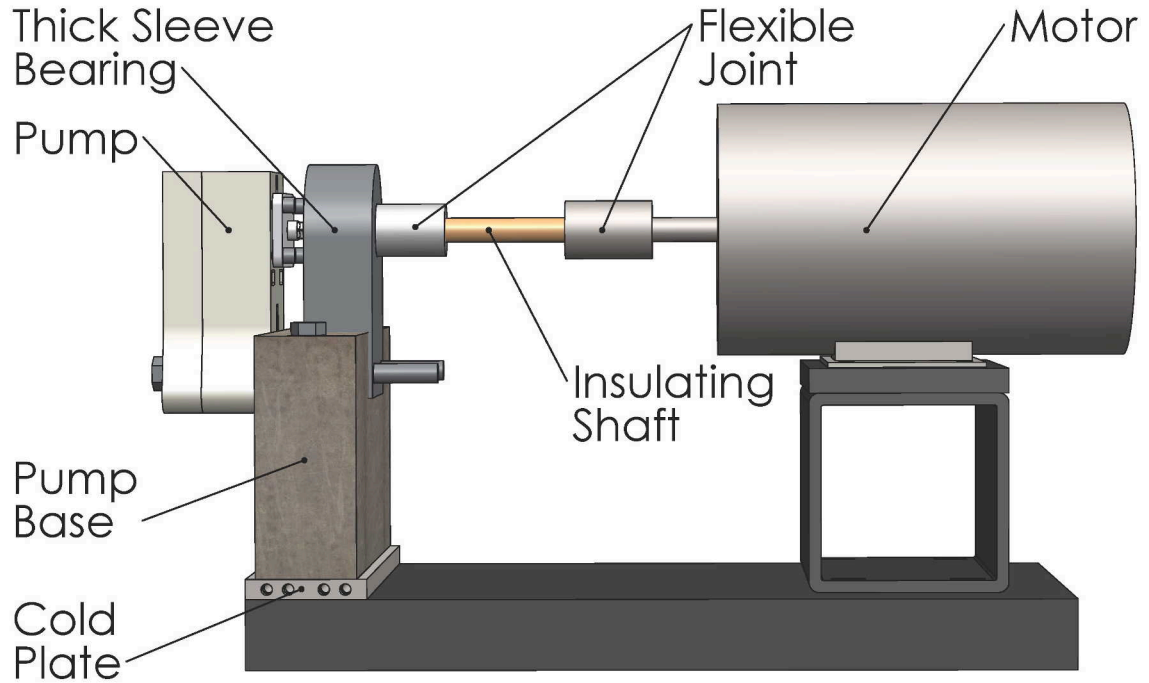


**Figure 68:** Alternate shaft actuation system. Here, both the hot (left) and cold (right) sides of the system accommodate misalignment through the use of flexible helical couplers. In this case, the hot coupler would be W or Mo based.

The second alignment challenge is between the pump and the external bearing. It is critical that these two remain very well aligned, as there is no active accommodation for misalignment here. Therefore, the materials and temperatures need to be well matched, or the pump and bearing must be mounted in such a way that they are stationary relative to each other—having temperature invariant alignment from geometry alone. This is possible via clever geometrical design, such as the one shown in Figure 69, but may be at the expense of other requirements (e.g., strength, thermal isolation). Furthermore, in the future, a metal (tungsten) coupler should be used to interface with the ceramic pump

shaft—although this coupler should be weight/strength optimized as shown in Figure 63. This would leverage the key design principle of using ceramics only where required for maximum chemical compatibility with molten metal. The insulating shaft, however, should still remain  $ZrO_2$  in order to allow the temperature drop needed. Additionally, the diameter of ceramic shafts should be maximized (extended to the base of gear teeth) and be about twice the (12 mm) diameter used in these tests.

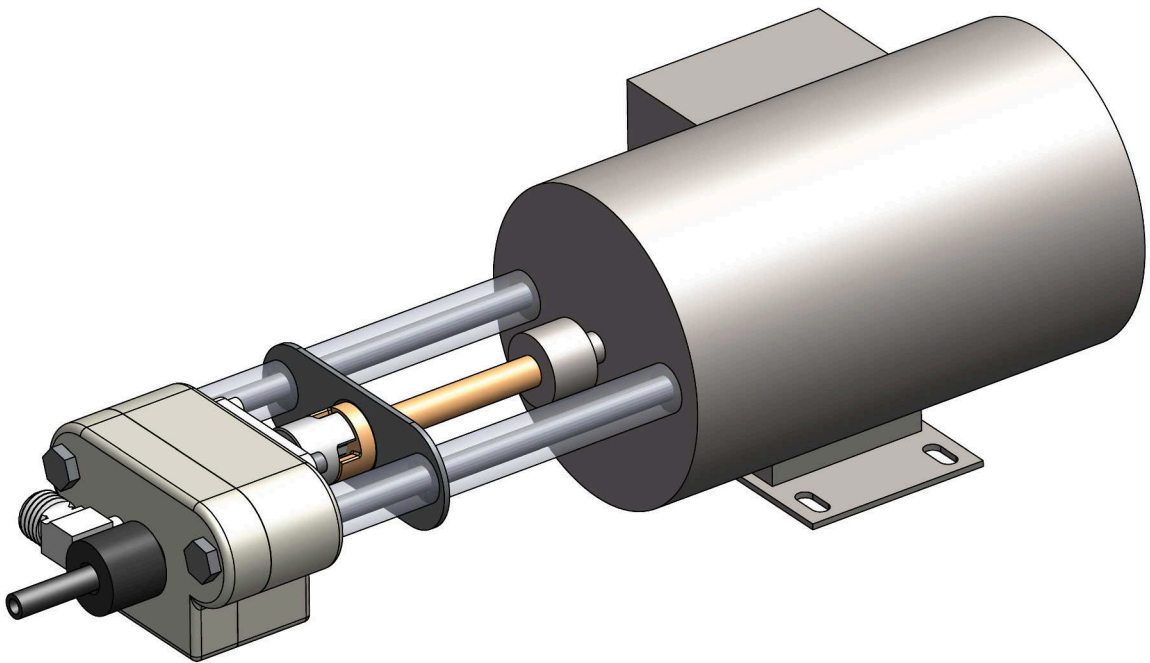


**Figure 69:** Alternate shaft actuation and mounting system. Here, thermally independent alignment can be achieved by mounting the pump directly to the motor at the plane of the pump drive shaft. This configuration would ideally have a vertical shaft axis to keep the forces symmetric.

#### 5.4.3 *Compatible fluids*

Although Sn is a very attractive heat transfer fluid for extreme temperature heat transfer, there are several applications where other fluids have advantages. For example,

for thermal energy storage (TES) which can be used with CSP or directly with the grid, Sn is too expensive to be used as a bulk storage fluid, at \$25 kg<sup>-1</sup> or \$104 K kJ<sup>-1</sup>. Here, aluminum (Al) or an Al-Si alloy is desirable [5]. Additionally, in the manufacturing of iron and nickel based components, the ability to pump these metals enable improved material properties and/or reduced cost [2, 31, 43]. Although several ceramics are compatible with these fluids, the seal is the critical limitation to enable their use—most challenging is the dynamic seal. This is because all the metals of interest, other than Sn, react with C. If a packing seal is still to be used, one candidate is BN, as it has a similar crystal structure to graphite, as described in the section on Pump Sealing in Design and Modeling of The Pump System.

In addition to replacing the seals, the graphite-based circulation loop would also have to be exchanged for an alternate material. This, however, is achievable with known materials—graphite was used because of convenience/cost in these experiments, but other options are available. For example, alumina based materials can be used, including castable cements like Westmoreland Advanced Materials' ALII-HD [5]. Other candidates, as mentioned in Chapter 2, include SiC and ZrO<sub>2</sub>.

Although many of the components employed in this work (C, W, AlN, etc) would suffer oxidation at the operation temperatures required, it is interesting to consider modifications that could be made to enable some, or all, of this system to operate outside of an inert environment. There are several options available for material coatings that could prevent oxidation. For example, a protective layer of silica (SiO<sub>2</sub>) can be formed on the surface of AlN to enable operation up to 1400°C with oxidation kinetics greatly reduced compared to exposed AlN, which is generally limited to 1000°C in an oxidizing

atmosphere [90]. Similarly, graphite can be converted to SiC via exposure to silicon particles at high temperature [91]. This process can be controlled so as to only convert a thin outer layer of the graphite (and the penetration depth is limited to 6 mm, as noted in Appendix D, which enables oxidation protection up to ~1300°C, while retaining many of the preferred qualities of graphite—low cost, machinability, and (relatively) high thermal conductivity at elevated temperature.

The most challenging issue, however, is to enable a high-temperature *hermetic* seal. This will be a key feature because even if the containment materials are protected from oxidation, the molten metal will not be. Among the seals required, the dynamic pump seal would be the most challenging to make hermetic. Here, fortunately, if the pump system is enclosed in its own an inert environment, then the hermetic seal can at least be static, and potentially even cold with clever flange design.

## CHAPTER 6. CONCLUSION

Liquid metals are extremely efficient heat transfer fluids, which can allow high-temperature thermal energy transfer and storage. However, it has previously been infeasible to pump liquid metals, or any liquid, above 1000°C. In this work a system has been developed that successfully pumped molten Sn at temperatures as high as 1490°C without failure. In an additional test that was temperature limited by the heater, Sn was pumped continuously for 72 hours, at 1200°C without failure. Therefore, the concept of using ceramic and refractory metal components in an inert atmosphere to pump liquid metal at extreme temperatures, should now be considered a viable approach. Tests at even higher temperatures, perhaps above 1600°C are expected to be successful and were only prevented by the combination of heat loss (largely from the flow viewport) and heater power input limitation.

This new ability has broad applications and it is therefore warranted to begin reevaluating how various industries operate in order to identify opportunities where major energy savings can be achieved, or energy efficiency can be increased. Thus, many technologies that have previously been non-competitive economically may become viable if this new regime of heat transfer and storage is employed. For example, though counterintuitive, it may be profitable, in today's market, to employ thermal energy grid storage (TEGS). This is only the case because, at such extreme temperature as displayed in this work, roundtrip efficiency can exceed 60%. Similarly, CSP at twice the current peak temperature is enabled by this approach—which is expected to result in a relative efficiency increase of 50% [11, 34]. Likewise, this new ability to move heat at extreme temperatures can enable TPV to function as a competitive heat engine for CSP [11]. Further, this technology can be applied to nuclear power generation [16, 27], enable new solar fuel concepts [39], and even improve the

efficiency of gas turbines, where up to 5% of system efficiency is lost to blade cooling [42]. Further detail of power generation enhancements is included in the Introduction.

Additionally, high-efficiency gas-gas heat exchange is enabled by this new technology. Here, Sn can be used as an intermediate heat transfer fluid in a direct contact heat exchanger to drastically reduce the amount of required solid surface area—and thus the cost and compressor power required for heat exchange [5, 28, 29]. Many industrial processes can also be made more efficient or effective by employing energy advection at extreme temperature [2, 31-33, 43]. These technologies include injection molding, casting, controlling the cooling rate of single crystal superalloys, and waste heat recovery. The Introduction includes detail about the contribution of pumping to this technology.

The remaining challenges, included in Discussion and Future Work, to enable long life and increased fluid compatibility include the selection of an alternative pump material that is thermodynamically stable, mechanically strong, and highly wear resistant. Further, shaft design can be improved to minimize misalignment, which will reduce stress—slowing wear and reducing the risk of pump failure from brittle fracture. Lastly, graphite components can be replaced with other ceramics compatible with Al, Fe, and Ni in order to enable additional applications.

# APPENDIX A: COMMERCIAL THERMAL ENERGY GRID

## STORAGE (TEGS) ATTEMPTS

### SIEMENS

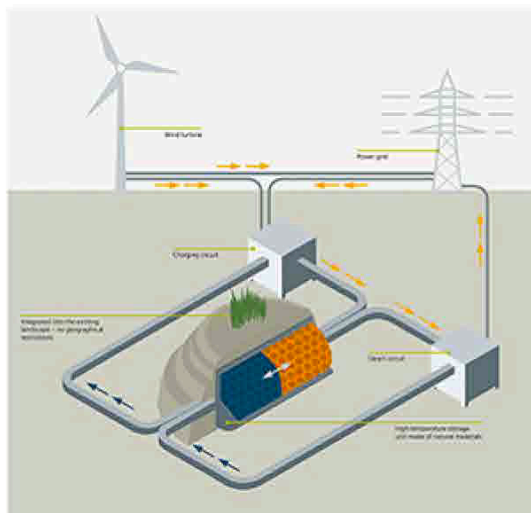
> Home > Press Wind Power and Renewables

#### Siemens presents thermal storage solution for wind energy

Hamburg, 2016-Sep-27

- Highly economic concept based on tried and trusted main components
- FES research project with Hamburg Energie and TU Hamburg-Harburg
- Funded by the German Federal Ministry for Economic Affairs and Energy

Siemens is developing economic storage technology: alongside Technical University Hamburg Harburg (TUHH) and urban utility company Hamburg Energie, Siemens is researching a storage solution in the Northern German city that will set a future standard in efficiency. After having been converted to heat in rock fill, excess wind energy is stored and protected with an insulated cover. When there is a need for additional electricity, a steam turbine converts the heat energy back to electricity. The simple principle of this store promises an extremely low-cost set-up. The project has therefore received research funding from the German Federal Ministry for Economic Affairs and Energy.



The thermal store for wind energy, which is being developed in Hamburg, is a joint project between Siemens, Hamburg Energie and TUHH. The German Federal Ministry for Economic Affairs and Energy is funding the project.

[https://www.siemens.com/press/en/pressrelease?press=en/pressrelease/2016/windpower-renewables/pr2016090419wpen.htm&content\[\]=WP](https://www.siemens.com/press/en/pressrelease?press=en/pressrelease/2016/windpower-renewables/pr2016090419wpen.htm&content[]=WP)

1/4

Siemens is currently operating a test set-up for the storage solution, named Future Energy Solution (FES), at Hamburg-Bergedorf. Alongside scientists from the TUHH Institute for Thermofluid Dynamics, the company is researching how to make charging and discharging the store particularly efficient. The arrangement of the rock fill and the form of the surrounding insulating container are crucial. The store is being tested at temperatures over 600 degrees Celsius. Just like a hot air gun, a fan uses an electrically-heated air flow to heat the stones to the desired temperature. When discharging, the hot stones in turn heat the air current, which then heats a steam boiler; its pressure drives a generator via a steam turbine.

As the current test set-up only tests the thermal requirements for the storage process, no reverse current is generated. However, researchers wish to test the complete energy conversion in spring 2017: from electricity to heat storage in the rock fill and back to electricity. They are establishing a complete thermal store on the Trimet aluminum smelter site in Hamburg-Altenwerder to the south of the River Elbe on the German A7 highway. The full-size FES will be able to store around 36 megawatt hours (MWh) of energy in a container with around 2,000 cubic meters of rock. Via a boiler, the heat it contains will generate so much steam that a Siemens compact steam turbine can generate output of up to 1.5 megawatts of electricity for up to 24 hours a day. The researchers expect to generate effectiveness of around 25% even in this early development phase. In the future the concept has the potential for an effectiveness of around 50%. Partner Hamburg Energie will investigate appropriate marketing options for the stored energy.

"The technology of our FES store deliberately uses mainly tried and trusted technology," says Till Bartheimer, Siemens' project manager. "Because we are working here with tested thermal components and a series-ready steam turbine, we will be able to offer a practical solution within a few years. Our complete experimental system will be operational in just around 15 months."

Whereas many other stores generate high costs or only permit limited storage capacities, the FES technology can be used in the most varied of sizes and output classes, and therefore always remains extremely economical. The only limit to the concept is the space required for the rock-filled insulated container.

For further information on Siemens' presented innovations at WindEnergy Hamburg, please see: <http://www.siemens.com/press/WindEnergy2016>

For further information on Siemens Wind Power and Renewables, please see: [www.siemens.com/wind](http://www.siemens.com/wind)

[https://www.siemens.com/press/en/pressrelease/?press=en/pressrelease/2016/windpower-renewables/pr2016090419wpen.htm&content\[\]=WP](https://www.siemens.com/press/en/pressrelease/?press=en/pressrelease/2016/windpower-renewables/pr2016090419wpen.htm&content[]=WP)



Sir Joseph  
Swan Centre  
for energy research



**Newcastle**  
University

### *Stand-alone, flexible storage*

We are developing a stand-alone energy storage system called Pumped Heat Energy Storage (PHES). The cycle uses a proprietary reciprocating heat pump/engine (developed in-house). It will take electricity from the grid to charge the system.

The reciprocating heat pump/engine is a positive displacement machine based on an entirely new concept. It has been designed from first principles to achieve high efficiency at low cost. The result is flexible power machinery that is optimised for use in electricity storage, that can be sited anywhere. It is designed to operate between 500°C and -160°C without lubrication. There are a number of potential applications for this machine.

w

e



## Thermal Stores

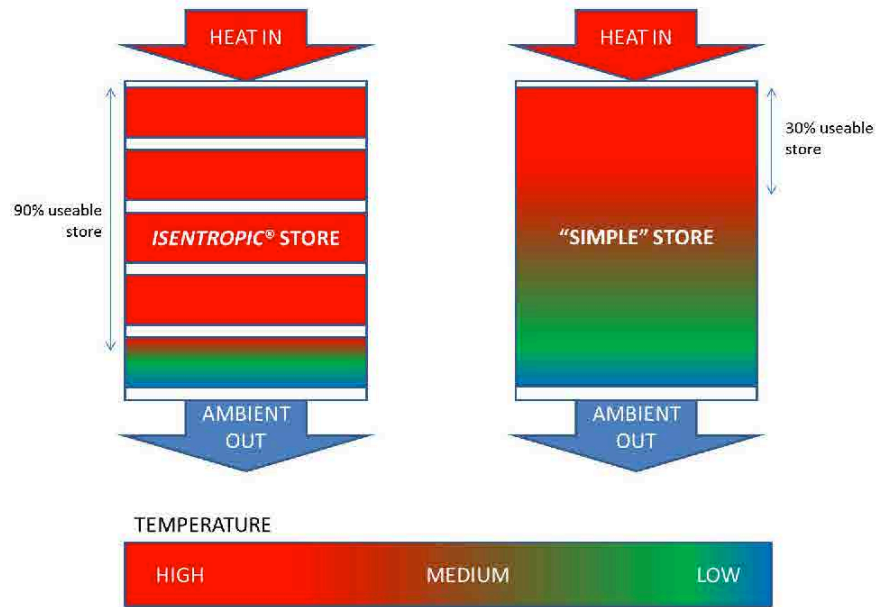
*PHES Thermal Stores are split into layers to achieve high efficiency of thermal transfer; low pressure drop and higher energy density than other 'packed bed' stores.*

The *PHES* Thermal Stores work by direct heat exchange between high pressure gas and particles of crushed rock or gravel. The design of a 'packed bed' store is normally a compromise between pressure drop and heat transfer. Reducing the particle size improves heat transfer efficiency but smaller particles offer more resistance to gas flow through the store. (The reverse is true for larger particles). The particle size of the storage media must therefore be carefully selected to mediate between these loss mechanisms.

### Layered Store

The most important contribution to 'packed bed' storage is the **layered store**. Gas flow can be confined to the region where heat exchange is active, termed the 'thermal front', while inactive areas, above and below, are bypassed. This allows the use of small particles for efficient heat.

exchange whilst maintaining a low pressure drop through the store. Active control of the thermal front allows for much higher energy density by ensuring that the front is kept short.



### Simple to Produce

The packed bed is contained within an insulated pressure vessel, such as the ones shown in the image below. The patented thermal store design is unique. Current designs envisage peak pressures of 25 bar and peak temperatures of 550°C. The external pressure vessel can be manufactured by a wide range of suppliers.



## Commercializing Standalone Thermal Energy Storage

*If thermal energy storage is less expensive than batteries, why aren't we hearing more about it?*

January 8, 2016

By Susan Kraemer, Correspondent



*Molten salt storage tanks at the Solana Generating Station in Arizona. Credit: Abengoa.*

Two innovators in highly efficient thermal energy storage materials believe that thermal storage could work as a standalone storage play, not just as part of a more familiar Concentrated Solar Power (CSP) project designed for electricity generation.

Anoop Mathur, founder and CEO of Terrafore Technologies, is a DOE awardee for his work on super-efficient advanced storage materials. He first suggested this possible new market for thermal storage as a pure storage play. He thinks that this kind of solar thermal energy plant would be designed to store all of its energy and be called upon on-demand like a battery.

"I believe, in the immediate future, we should be looking at this market," said Mathur. "Analysis has shown that using a large turbine with a small solar field and up to three hours of storage is significantly more profitable, if allowed to participate in ancillary services such as spinning reserve and regulation rather than just the day-ahead energy market. The benefit-to-cost ratio was calculated to be more than 25 percent for the California market."

<http://www.renewableenergyworld.com/articles/print/volume-18/issue-110/features/thermal-renewable-energy/commercializing-standalone-thermal-energy-sto...> 1/4

The way to make this form of solar act purely as storage would be to oversize the turbine in a full CSP project, and then run the plant just to fill the storage tanks, Mathur suggested.

"For example, a solar field designed for 100 MWe with a 200 MWe turbine and up to three hours of storage, supplying 300 MWhs a day, can have higher revenues to justify the capital costs than a plant designed for day-ahead energy markets."

Generating entirely from the storage on demand, this kind of grid storage would look like a solar thermal power plant but act like a battery.

"The utility industry pays high dollars for guaranteed power when they need it. For these markets the thermal storage route is definitely profitable today," Mathur said.

## Solving Power Block Cost

Halotechnics founder and CEO Justin Raade has also explored deploying stand-alone thermal storage in a similar pure storage play, because of its economy: storage with molten salts in a tower CSP plant costs about a tenth of the cost of battery storage, at around \$30 per kWh, compared to \$250 per kWh for batteries.

Initially, he envisioned a standalone storage tank of molten salt with PV or wind supplying electricity to heat the molten salts, and a steam turbine at the other end to turn the heat back to electricity for the grid. But after estimating the cost of standalone storage fed by electricity from PV (or wind) Raade found that most of what stood in the way of cost-effectiveness was the inclusion of the turbine used to transform the heat energy back into electricity.

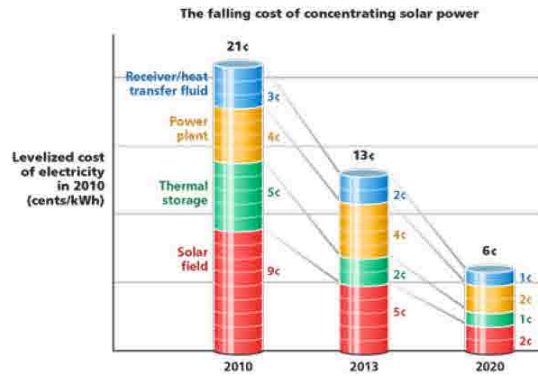
Power block costs canceled out the savings of standalone thermal energy storage. When thermal energy storage is included as part of a CSP project, the cost is minimized because the power block is already needed for electricity generation, so it is part of the plant cost, not of just storage, which is just tanks, piping, heat exchangers and cheap molten salts. But if not amortized by a full power plant, the power block is costly.

Armed with this realization, Raade took another approach. Instead of building a standalone thermal storage unit, fed by electricity from PV or wind, he now envisions offering this storage as a unit that can be piggybacked on an already existing turbine, cutting power block cost. The thermal storage unit would be attached to the steam turbine power block in a combined-cycle natural gas plant, and be commercialized as an efficiency improvement. By turning stored energy back into electricity using an existing steam turbine, costs are minimized. And as Glasspoint has done, with 1 GW of solar thermal for industrial steam production, Raade believes that the deeper pockets of the fossil fuel industry could help him get from innovation to commercialization.



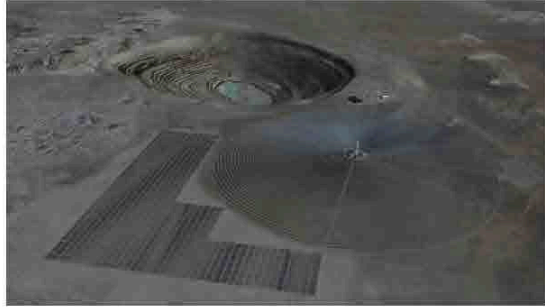
Chile's Atacama Desert will soon be home to the first hybrid CSP with Molten Salt Storage plus PV projects to help power mining operations, like this copper mine. Credit: Shutterstock.

Raade's long-term plan is to use earnings from this thermal energy storage using bankable molten salts to fund deployment of his signature molten glass storage. Halotechnics is an ARPA-E award winner for high-temperature molten glass phase-changing material, a storage medium for the advanced CSP storage of the future.



The costs of concentrating solar power (CSP) with storage is expected to fall to less than 6 cents per kWh by 2020. Credit U.S. Department of Energy Sunshot Initiative.

“Our next generation product would utilize our molten glass energy storage at 1,500°C and would integrate into a combined cycle power plant in much the same way,” said Raade.



*Artist rendering of the SolarReserve Copiapó plant. After construction began, a second tower was added to the design. Credit: SolarReserve.*

These temperatures are significantly ahead of their time for the concentrating solar power industry, which now operates at a high of 1,050° F and “freezes” at 550° F. The DOE SunShot Initiative is funding research into developing the receivers and tank materials needed to contain higher temperature storage materials for commercial deployment by 2020.

## Thermal Renewables To Replace Peaker Plants?

The grid needs an alternative to the polluting single-cycle peaker plants, both for instant response and for several hours of dispatchable generation on demand. Could solar thermal storage units displace these dirty peaker plants? Well, maybe not.

Single cycle plants can respond within a minute, which is why they are deployed as peakers. But there is a penalty for the fast action. They emit 1,365 pounds of CO<sub>2</sub> per MWh. At 825 pounds of CO<sub>2</sub> per MWh, combined-cycle natural gas plants are somewhat cleaner, but too slow to be peakers. Their response is limited by steam turbine ramp rates, which is typically about 10 percent a minute. CSP plants use the same kind of back-end power block, so they also cannot be instant-on like the higher-emitting peaker. However, if a CSP plant is running off its stored heat, it could start to respond in just ten minutes, Mathur said.

## As a Solar Battery for PV

In general, the thermal storage included with CSP decouples solar generation from energy that must be taken whenever it is generated — into a form of solar that could be available whenever it is needed. Molten salt thermal energy storage used in conjunction with CSP supplies a dispatchable form of solar energy. Some of the solar can be stored to be available when the grid requires it.

But CSP could also be built in a hybrid with a PV plant, where virtually all of the CSP is stored for use on demand, creating what amounts to a solar-powered “battery” for PV.

For the first time, such a combination is under construction now in two PV/CSP plants in Chile’s Atacama Desert, with the CSP being stored for use as a battery. This region primarily powers mining operations, which need power 24/7, and solar is able to supply this round-the-clock need by combining two forms of solar generation.

At Atacama-2 Abengoa is building a hybrid combining 100 MW of PV with 110 MW of CSP with a record 17.5 hours of thermal storage. To make up the initial ten-minute gap, Abengoa will also include a small (12 MW, 4 MWh) actual battery

<http://www.renewableenergyworld.com/articles/print/volume-18/issue-110/features/thermal-renewable-energy/commercializing-standalone-thermal-energy-sto...> 4/4

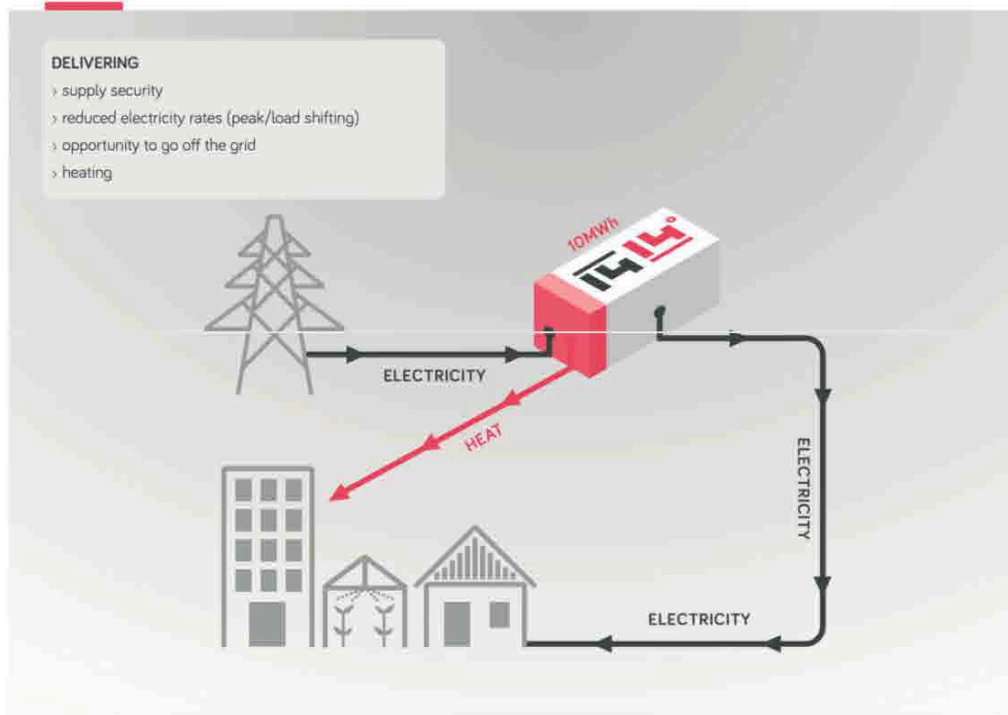


Renewable generators produce electricity intermittently. This requires backup generation in electricity networks during periods where renewable energy sources are low or not available.

Our patented thermal energy storage system (TESS) stores latent heat in molten silicon at 1414 degrees celsius providing maximum efficiency of energy output and transforming intermittent renewable electricity into reliable thermally generated power.

There are numerous way TESS can be implemented into an energy grid delivering energy efficiency, energy security and support during a blackout.

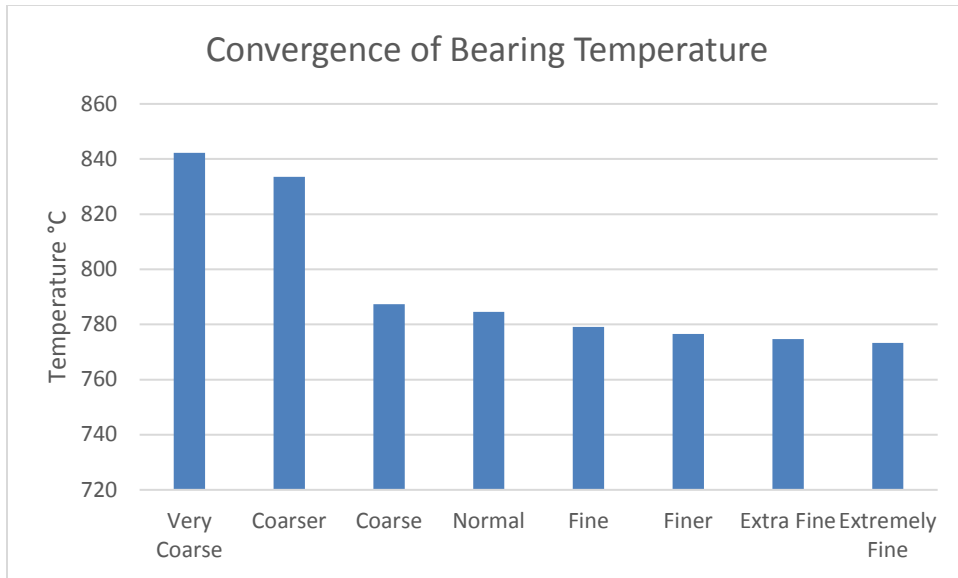
## 1414 DEGREES AFTER THE METER > E.G. COMMERCIAL / INDUSTRY / FARM INSTALLATION



## APPENDIX B: PROPERTIES AND MESH CONVERGENCE OF THERMAL MODELS

In order to check mesh convergence, several mesh settings were examined until it was clear that the solution had converged on a value. Two representative measurements were considered as representative of convergence: the temperature of the external tungsten bearing, and the heat loss through the pump mount. These were chosen because they are sensitive to mesh convergence and are relevant outputs of the model. It was found that for mesh quality “Normal” or better, adequate convergence (~5% uncertainty) was achieved. The table below shows the results, where similar results were found for meshes containing 180,000-7,000,000 elements.

Mesh Quality	Maximum element size (inch)	Minimum element size (inch)	Number of elements	Bearing Temperature (°C)	Cold plate heat loss (W)	Error
<b>Very Coarse</b>	7	0.75	78066	842.23	210.26	34%
<b>Coarser</b>	4.75	0.5	91498	833.49	205.18	33%
<b>Coarse</b>	3.75	0.701	123,170	787.29	181.22	8%
<b>Normal</b>	2.5	0.45	178,205	784.56	181.07	6%
<b>Fine</b>	2	0.25	318,650	779.13	180.96	3%
<b>Finer</b>	1.38	0.1	641,762	776.57	178.09	2%
<b>Extra Fine</b>	0.876	0.0375	1,929,544	774.73	176.22	1%
<b>Extremely Fine</b>	0.5	0.005	6,678,435	773.27	175.12	



In the table below, relevant properties for the materials used in COMSOL modeling are included. Constant properties are based on an average temperature of 1000°C.

Manufacturer	Material	Thermal Conductivity (W/mK)	CTE (1/K)
Tokuyama	Shapal	35	4.90E-06
Zircar Ceramics	Alumina Blanket AB	$0.000000156 \cdot T^2 - 0.0000025 \cdot T + .055$	N/A
Ohio Carbon	Graphite	60	5.00E-06
SilRath	AK-60 Andalusite	2.2	4.50E-06
	Low Carbon Steel	44.5	1.23E-05
	Zirconia	2.2	1.00E-05
	Tungsten	110	4.50E-06

# APPENDIX C: PUMP SPEED AND PERFORMANCE

## RECOMMENDATIONS

	
<p><b><i>Application Note to the Field</i></b></p>	<p><b>Minimum Flow Rate for Gear Pumps</b></p>
<p><b>Application Note Number: 1602-5</b></p>	<p><b>Date: February 3, 2016</b></p>

### Turndown Ratio of a Gear Pump

A gear pump is an excellent choice for metering fluids. Often times the pump is called upon to meter a range of flow rates. The ratio of this range (maximum flow divided by minimum flow) is called the *turndown ratio* or simply, the *turndown*. For example, the range of 10 GPM to 1 GPM would be a turndown of 10:1.

First, it is important to distinguish between the motor and the pump. When adjustable flow of a gear pump is required, the best and most common way to do so is by adjusting the motor RPM, usually by means of a VFD (Variable Frequency Drive). When using this method, the turndown ratio of the motor must be considered and should fall into the required range of the pump. This ratio will vary depending on the manufacturer and type of motor, so it is best to check with the manufacturer for their specifications. A common turndown ratio for Baldor Premium Efficiency TEFC motors is 10:1 constant torque, which allows a 4-pole 60 Hz motor to safely operate from 1800 to 180 RPM (or under full-load from 1750 to 175 RPM), which is adequate for the majority of gear pump applications.

The turndown ratio of the pump is not as straightforward, because there is not one fixed answer. In theory, the pump can be run all the way down to zero RPM, if the conditions are right. Conditions which allow the pump to achieve a high turndown ratio (10:1 or more) are moderate to high viscosity (2 cP and above) and stable differential pressure. If the differential pressure varies, so can the flow rate, which can negatively impact metering accuracy. If this is a concern, a backpressure valve can be used to stabilize the pressure. A closed loop control system with a flowmeter feedback can also be used to increase the accuracy for a given system. At extremely low RPM, small pulsations may occur, caused by the slow rotation of the gear teeth. If a thin fluid is used, the pump is subject to excessive slip, which reduces the efficiency and accuracy, and narrows the RPM range the pump can successfully operate in, thus preventing a large turndown. The average turndown for a thin fluid (< 2 cP) is 2:1.

There is no fixed rule for the maximum turndown ratio of a gear pump; it varies by application. However, with the proper conditions, ratios in the range of 20:1 are achievable. For higher ratios or thin fluids, a recirculating loop may be a more accurate alternative.

### Metering Pump Selection

When metering, the pump size plays an important role. To achieve an accurate flow over a wide range, the smallest pump which fits inside the range is often the best selection. This allows a wider operating speed range and more discrete operating points, therefore allowing more controllability.

**Liquiflo Application Note to the Field: Minimum Flow Rate for Gear Pumps**

As an example, to achieve a flow rate of 1-2 GPM for a 20 cP fluid at 100 PSI differential pressure, there are three pump options, as shown in the table below:

Pump Size	Min RPM (1 GPM)	Max RPM (2 GPM)	Turndown Ratio	Motor		VFD	
				RPM Range	RPM Span	Hz Range	Hz Span
H5R	750	1470	1.96 : 1	750-1470	720	25-49	24
H5F	540	1040	1.93 : 1	540-1040	500	18-35	17
H7N	340	655	1.93 : 1	340-655	315	11-22	11

The smallest size pump offers the largest RPM range. Therefore, the most controllability for flow rates in between the Min and Max is achieved with the smaller pump.

**Note:** The Hz Range above is the VFD frequency range corresponding to the motor speed range (assuming zero slip between synchronous speed and actual motor speed). Since the motor used is a 4-pole motor, the VFD frequency is twice the motor speed in Hz. This relation is given by the following formula:

$$VFD\ Frequency\ [Hz] = 2 * Motor\ Speed\ [RPM] * \frac{1\ [Hz]}{60\ [RPM]}$$

For example, the VFD frequencies corresponding to motor speeds of 750 and 1470 RPM are given by:

$$VFD\ Frequency, Min = 2 * 750\ [RPM] * \frac{1\ [Hz]}{60\ [RPM]} = 25\ Hz$$

$$VFD\ Frequency, Max = 2 * 1470\ [RPM] * \frac{1\ [Hz]}{60\ [RPM]} = 49\ Hz$$

# APPENDIX D: SiC FORMATION ON C: THICKNESS LIMITATIONS

POCO SiC process - Complex Graphite Parts

---

Wayne Hambek to Caleb

Jan 13

Caleb,  
I apologize, I must have missed your first e-mail.

Either of the scenarios you outlined below is possible within POCO's process. We are bound by some design constraints, though. We have a maximum thickness for fully-converted SUPERSiC® of 0.25". For the 'Skin' process, (not fully converted, but just an outer SiC shell), this limitation does not apply. The other limit is on the size of individual components. Our conversion furnace can accommodate a component of diameter of 750mm. This may be stretched for non-round parts, maybe up to 800-850mm, as we can possibly tilt the part in the chamber to gain more length. Beyond that dimension, we are able to attach parts with our 'RBSC' process after conversion. This process has shown to be stronger than the base material, and so we have confidence that there is no performance degradation that results.

Please let me know if you have any further questions.

Best Regards,

Wayne Hambek

Director, Industrial & Glass Handling Products  
POCO - Industrial Sales

300 Old Greenwood Rd  
Decatur, Texas 76234 US

T [+1 940 393 4223](tel:+19403934223) M [+1 469 235 8322](tel:+14692358322)



entegris.com  
50 YEARS OF PURE ADVANTAGE



**From:** Caleb Amy [mailto:[calebaamy@gatech.edu](mailto:calebaamy@gatech.edu)]  
**Sent:** Thursday, January 12, 2017 7:43 PM  
**To:** Wayne Hambek <[Wayne.Hambek@entegris.com](mailto:Wayne.Hambek@entegris.com)>  
**Subject:** Re: POCO SiC process - Complex Graphite Parts

## REFERENCES

1. "Annual Energy Outlook," (US Energy Information Agency, 2017).
2. A. J. Elliott, T. M. Pollock, Thermal Analysis of the Bridgman and Liquid-Metal-Cooled Directional Solidification Investment Casting Processes. *Metallurgical and Materials Transactions A* **38**, 871-882 (2007).
3. V. M. B. Nunes, C. S. Queirós, M. J. V. Lourenço, F. J. V. Santos, C. A. Nieto de Castro, Molten salts as engineering fluids. *Applied Energy* **183**, 603-611 (2016).
4. K. Vignarooban, X. Xu, A. Arvay, K. Hsu, A. M. Kannan, Heat transfer fluids for concentrating solar power systems – A review. *Applied Energy* **146**, 383-396 (2015).
5. G. Wilk, Liquid metal based high temperature concentrated solar power: Cost considerations, Georgia Institute of Technology, (2016).
6. A. Fritsch *et al.*, Conceptual Study of Central Receiver Systems with Liquid Metals as Efficient Heat Transfer Fluids. *Energy Procedia* **69**, 644-653 (2015).
7. B. Elkin, L. Finkelstein, T. Dyer, J. Raade, Molten Oxide Glass Materials for Thermal Energy Storage. *Energy Procedia* **49**, 772-779 (2014).
8. E. B. Shand, *Glass Engineering Handbook*. (McGraw Hill, 1958).
9. N. Lorenzin, A. Abánades, A review on the application of liquid metals as heat transfer fluid in Concentrated Solar Power technologies. *International Journal of Hydrogen Energy* **41**, 6990-6995 (2016).
10. J. Pacio, T. Wetzel, Assessment of liquid metal technology status and research paths for their use as efficient heat transfer fluids in solar central receiver systems. *Solar Energy* **93**, 11-22 (2013).
11. H. R. Seyf, A. Henry, Thermophotovoltaics: a potential pathway to high efficiency concentrated solar power. *Energy & Environmental Science* **9**, 2654-2665 (2016).
12. H. R. Kim, Y. B. Lee, A design and characteristic experiment of the small annular linear induction electromagnetic pump. *Annals of Nuclear Energy* **38**, 1046-1052 (2011).

13. X. Dong, X. Huang, L. Liu, L. He, P. Li, A liquid aluminum alloy electromagnetic transport process for high pressure die casting. *Journal of Materials Processing Technology* **234**, 217-227 (2016).
14. M. Plevan *et al.*, Thermal cracking of methane in a liquid metal bubble column reactor: Experiments and kinetic analysis. *International Journal of Hydrogen Energy* **40**, 8020-8033 (2015).
15. C. Fazio, F. Balbaud, Corrosion phenomena induced by liquid metals in Generation IV reactors A2 - Yvon, Pascal. *Structural Materials for Generation IV Nuclear Reactors*, 23-74 (2017).
16. A. Y. Legkikh, R. S. Askhadullin, R. P. Sadovnichiy, Ensuring the corrosion resistance of steels in heavy liquid metal coolants. *Nuclear Energy and Technology* **2**, 136-141 (2016).
17. T. Emmerich, C. Schroer, Corrosion in austenitic steels and nickel-based alloys caused by liquid tin at high temperature. *Corrosion Science*, (2017).
18. R. Danzer, On the relationship between ceramic strength and the requirements for mechanical design. *Journal of the European Ceramic Society* **34**, 3435-3460 (2014).
19. A. Henry, R. Prasher, The prospect of high temperature solid state energy conversion to reduce the cost of concentrated solar power. *Energy & Environmental Science* **7**, 1819-1828 (2014).
20. M. M. Opeka, I. G. Talmy, E. J. Wuchina, J. A. Zaykoski, S. J. Causey, Mechanical, Thermal, and Oxidation Properties of Refractory Hafnium and zirconium Compounds. *Journal of the European Ceramic Society* **19**, 2405-2414 (1999).
21. M. M. Opeka, I. G. Talmy, J. A. Zaykoski, Oxidation-based materials selection for 2000°C + hypersonic aerosurfaces: Theoretical considerations and historical experience. *Journal of Materials Science* **39**, 5887-5904 (2004).
22. W. G. Fahrenholtz, G. E. Hilmas, Ultra-high temperature ceramics: Materials for extreme environments. *Scripta Materialia* **129**, 94-99 (2017).
23. D. Frazer, E. Stergar, C. Cionea, P. Hosemann, Liquid Metal as a Heat Transport Fluid for Thermal Solar Power Applications. *Energy Procedia* **49**, 627-636 (2014).
24. E. Slavcheva, B. Shone, A. Turnbull, Review of naphthenic acid corrosion in oilrefining. *British Corrosion Journal* **34**, 125-131 (1999).
25. S. Cissé, L. Laffont, B. Tanguy, M.-C. Lafont, E. Andrieu, Effect of surface preparation on the corrosion of austenitic stainless steel 304L in high temperature steam and simulated PWR primary water. *Corrosion Science* **56**, 209-216 (2012).

26. M. Sun, X. Wu, Z. Zhang, E.-H. Han, Oxidation of 316 stainless steel in supercritical water. *Corrosion Science* **51**, 1069-1072 (2009).
27. J. R. Weeks, Lead, bismuth, tin and their alloys as nuclear coolants. *Nuclear Engineering and Design* **15**, 363-372 (1971).
28. A. P. Bruckner, A. T. Mattick, High effectiveness liquid droplet/gas heat exchanger for space power applications. *Acta Astronautica* **11**, 519-526 (1984).
29. J. R. Welty, Direct-Contact Heat Transfer in Solid-Gas Systems. *Direct-Contact Heat Transfer*, 197-201 (1988).
30. I. Gur, K. Sawyer, R. Prasher, Searching for a Better Thermal Battery. *Science* **335**, 1454 (2012).
31. P. Kapranos, C. Carney, A. Pola, M. Jolly, Advanced Casting Methodologies: Investment Casting, Centrifugal Casting, Squeeze Casting, Metal Spinning, and Batch Casting. *Comprehensive Materials Processing*, 39-67 (2014).
32. A. Thekdi, S. U. Nimbalkar, "Industrial Waste Heat Recovery - Potential Applications, Available Technologies and Crosscutting R&D Opportunities," (Oak Ridge National Lab., TN 2015).
33. W. Yang *et al.*, Thermodynamics analysis of carbothermal-chlorination reduction in aluminum production. *Applied Thermal Engineering* **111**, 876-883 (2017).
34. A. DeAngelis, Analysis and design of a high temperature liquid metal solar thermal receiver, The Georgia Institute of Technology (2016).
35. A. W. Dowling, T. Zheng, V. M. Zavala, Economic assessment of concentrated solar power technologies: A review. *Renewable and Sustainable Energy Reviews* **72**, 1019-1032 (2017).
36. G. Wilk, A. DeAngelis, A. Henry, Estimating the Cost of High Temperature Liquid Metal Based Concentrated Solar Power. *Solar Energy*, (In Review).
37. "Sunshot Vision Study," (NREL, EERE, US DOE, 2012).
38. "On the path to SunShot," (SETO, EERE, US DOE, 2016).
39. C. Yuan, C. Jarrett, W. Chueh, Y. Kawajiri, A. Henry, A new solar fuels reactor concept based on a liquid metal heat transfer fluid: Reactor design and efficiency estimation. *Solar Energy* **122**, 547-561 (2015).
40. R. Sioshansi, P. Denholm, T. Jenkin, J. Weiss, Estimating the value of electricity storage in PJM: Arbitrage and some welfare effects. *Energy Economics* **31**, 269-277 (2009).

41. F. Cascella, A. Teyssedou, Modeling a Direct Contact Heat Exchanger used in a supercritical water loop. *Applied Thermal Engineering* **79**, 132-139 (2015).
42. R. C. Wilcock, J. B. Young, J. H. Horlock, The Effect of Turbine Blade Cooling on the Cycle Efficiency of Gas Turbine Power Cycles. *Journal of Engineering for Gas Turbines and Power* **127**, 109-120 (2005).
43. C. L. Brundidge, J. D. Miller, T. M. Pollock, Development of Dendritic Structure in the Liquid-Metal-Cooled, Directional-Solidification Process. *Metallurgical and Materials Transactions A* **42**, 2723-2732 (2011).
44. Y. Zhang *et al.*, Containment materials for liquid tin at 1350C as a heat transfer fluid for high temperature concentrated solar power. (In Review).
45. S. Bodbodak, M. Moshfeghifar, *Advances in controlled atmosphere storage of fruits and vegetables*. Eco-Friendly Technology for Postharvest Produce Quality (Academic Press, 2016), pp. 39-76.
46. A. K. Thompson, D. Bishop, *Controlled Atmosphere Technology*. Reference Module in Food Science (Elsevier, 2016).
47. H. Zhao, R. Woods, *Controlled atmosphere brazing of aluminum*. Advances in Brazing (Woodhead Publishing, 2013), pp. 280-323.
48. G. Fiegl, W. Torbet. (Google Patents, 1981).
49. P. F. Tortorelli, J. H. DeVan, *Thermal-gradient mass transfer in lithium-stainless steel systems*. Conference: 1. topical meeting on fusion reactor materials, Miami Beach, FL, USA, 29 Jan 1979 (; Oak Ridge National Lab., TN (USA), 1979), pp. Medium: ED; Size: Pages: 5.
50. R. N. Lyon, D. L. V. Katz, U. S. O. o. N. R. C. o. t. B. P. o. L. Metals, U. S. A. E. Commission, U. S. N. D. B. o. Ships, *Liquid-metals Handbook*. (U.S. Government Printing Office, 1954).
51. D. W. Jeppson, J. L. Ballif, W. W. Yuan, B. E. Chaou, "Lithium Literature Review: Lithium's Properties and Interactions," (Hanford Engineering Development Laboratory, 1978).
52. V. Sobolev, "Database of thermophysical properties of liquid metal coolants for GEN-IV," (SCK-CEN, 2010).
53. Y. Wang, Application of ceramic thermal spray coatings for molten metal handling tools and moulds. *Surface Engineering* **15**, 205-209 (1999).
54. N. P. Padture, M. Gell, E. H. Jordan, Thermal Barrier Coatings for Gas-Turbine Engine Applications. *Science* **296**, 280-284 (2002).

55. J. E. House, K. A. House, *Silicon, Germanium, Tin, and Lead*. Descriptive Inorganic Chemistry (Third Edition) (Academic Press, Boston, 2016), pp. 177-196.
56. R. S. Lima, P. H. Dionísio, J. T. Moro, W. H. Schreiner, C. Achete, Thermal evolution and stability of a tin nitride obtained by reactive sputtering. *Hyperfine Interactions* **83**, 315-319 (1994).
57. H. Yanagida, M. Miyayama, in *Concise Encyclopedia of Advanced Ceramic Materials*. (Pergamon, Oxford, 1991), pp. 340-346.
58. J. Wang, R. Stevens, Zirconia-toughened alumina (ZTA) ceramics. *Journal of Materials Science* **24**, 3421-3440 (1989).
59. E. Illeková, K. Csomorová, Kinetics of oxidation in various forms of carbon. *Journal of Thermal Analysis and Calorimetry* **80**, 103-108 (2005).
60. J. Habainy, C. Nilsson, Oxidation of Pure Tungsten in the Temperature Interval 400° to 900°C, Lund University, (2013).
61. B. Predel, *Sn-W (Tin-Tungsten)*. Pu-Re – Zn-Zr (Springer Berlin Heidelberg, Berlin, Heidelberg, 1998).
62. L. L. Oden, N. A. Gokcen, Sn-C and Al-Sn-C phase diagrams and thermodynamic properties of C in the alloys: 1550 °C to 2300 °C. *Metallurgical Transactions B* **24**, 53-58 (1993).
63. M. Venkatraman, J. P. Neumann, The Cr–Sn (Chromium-Tin) system. *Journal of Phase Equilibria* **9**, 159-162 (1988).
64. T. B. Massalski, H. Okamoto, P. R. Subramanian, L. Kacprzak, Binary Alloy Phase Diagrams. *ASM International 2nd Edition*, (1990).
65. S. P. Taguchi, S. Ribeiro, Silicon nitride oxidation behaviour at 1000 and 1200 °C. *Journal of Materials Processing Technology* **147**, 336-342 (2004).
66. J. Edgar *et al.*, Oxidation of Aluminum Nitride for Defect Characterization. *MRS Proceedings* **892**, (2011).
67. H.-T. Kim, J.-S. Han, J.-H. Yang, J.-B. Lee, S.-H. Kim, The effect of low temperature aging on the mechanical property & phase stability of Y-TZP ceramics. *The Journal of Advanced Prosthodontics* **1**, 113-117 (2009).
68. T. Sato, K. Haryu, T. Endo, M. Shimada, High temperature oxidation of hot-pressed aluminium nitride by water vapour. *Journal of Materials Science* **22**, 2277-2280 (1987).
69. in *When to use a Positive Displacement Pump* (Viking Pump, Inc., 2007).

70. in *Positive Displacement Pump Applications and Benefits*. (IPEG, 2017).
71. W. E. Forsthoffer, *Pump Best Practices*. Forsthoffer's Best Practice Handbook for Rotating Machinery (Butterworth-Heinemann, Boston, 2011), pp. 25-91.
72. . (Wikipedia, the free encyclopedia).
73. B. Améduri, B. Boutevin, G. Kostov, Fluoroelastomers: synthesis, properties and applications. *Progress in Polymer Science* **26**, 105-187 (2001).
74. I. Milošev, B. Navinšek, Corrosion properties of selected Cr-based hard and protective coatings. *Surface and Coatings Technology* **60**, 545-548 (1993).
75. F. F. Schmidt, H. R. Ogden, "The engineering properties of tungsten and tungsten alloys," (DTIC Document, 1963).
76. A. Wronski, A. Foukdeux, The ductile-brittle transition in polycrystalline tungsten. *Journal of the Less Common Metals* **8**, 149-158 (1965).
77. S. A. Humphry-Baker, W. E. Lee, Tungsten carbide is more oxidation resistant than tungsten when processed to full density. *Scripta Materialia* **116**, 67-70 (2016).
78. *Pump types*. Handbook of Pumps and Pumping (Elsevier Science Ltd, Oxford, 2006), pp. 1-54.
79. R. F. Hill. (Google Patents, 1997).
80. A. S. Wronski, A. C. Chilton, E. M. Capron, The ductile-brittle transition in polycrystalline molybdenum. *Acta Metallurgica* **17**, 751-755 (1969).
81. R. G. Budynas, J. K. Nisbett, J. E. Shigley, *Shigley's mechanical engineering design*. McGraw-Hill series in mechanical engineering. (McGraw-Hill, Singapore ;, ed. 8th ed. in SI units /, 2008).
82. P. K. Chougule, S. S. Kumbhar, Y. D. Kolekar, C. H. Bhosale, Enhancement in Curie temperature of nickel substituted Co–Mn ferrite. *Journal of Magnetism and Magnetic Materials* **372**, 181-186 (2014).
83. R. J. Thorn, O. C. Simpson, Spectral Emissivities of Graphite and Carbon. *Journal of Applied Physics* **24**, 633-639 (1953).
84. A. I. Golovashkin, G. P. Motulevich, Optical and Electrical Properties of Tin *Journal of Experimental and Theoretical Physics* **19**, 310 (1963).
85. F. P. Incropera, A. S. Lavine, T. L. Bergman, D. P. DeWitt, *Fundamentals of heat and mass transfer*. (Wiley, 2007).
86. G. Blyholder, H. Eyring, Kinetics of Graphite Oxidation II. *The Journal of Physical Chemistry* **63**, 1004-1008 (1959).

87. I. Hutchings, P. Shipway, *Friction and Wear of Engineering Materials*. Tribology (2nd) (Butterworth-Heinemann, 2017), pp. 1-5.
88. K. H. Zum Gahr, W. Bundschuh, B. Zimmerlin, Effect of grain size on friction and sliding wear of oxide ceramics. *Wear* **162**, 269-279 (1993).
89. D. McLachlan, E. Ehlers, Effect of Pressure on the Melting Temperature of Metals *Journal of Geophysical Research* **76**, 2780-2789 (1971).
90. Y.-H. Koh, J.-J. Choi, H.-E. Kim, Strengthening and Prevention of Oxidation of Aluminum Nitride by Formation of a Silica Layer on the Surface. *Journal of the American Ceramic Society* **83**, 306-310 (2000).
91. P. W. Trester, G. R. Hopkins, J. L. Kaae, J. Whitley, Performance results on a C-SiC alloy coating chemically vapor-deposited onto graphite substrates. *Thin Solid Films* **108**, 383-393 (1983).